

---

Electronic Thesis and Dissertation Repository

---

9-28-2017 11:30 AM

## Determining the Reactivity and Oxidation Intermediates of an Allylnickel (N-Heterocyclic Carbene) Chloride Complex

Scott W. E. Hendriks  
*The University of Western Ontario*

Supervisor  
Dr. Johanna Blacquiere  
*The University of Western Ontario*

Graduate Program in Chemistry  
A thesis submitted in partial fulfillment of the requirements for the degree in Master of Science  
© Scott W. E. Hendriks 2017

Follow this and additional works at: <https://ir.lib.uwo.ca/etd>

 Part of the [Inorganic Chemistry Commons](#)

---

### Recommended Citation

Hendriks, Scott W. E., "Determining the Reactivity and Oxidation Intermediates of an Allylnickel (N-Heterocyclic Carbene) Chloride Complex" (2017). *Electronic Thesis and Dissertation Repository*. 4926.  
<https://ir.lib.uwo.ca/etd/4926>

This Dissertation/Thesis is brought to you for free and open access by Scholarship@Western. It has been accepted for inclusion in Electronic Thesis and Dissertation Repository by an authorized administrator of Scholarship@Western. For more information, please contact [wlsadmin@uwo.ca](mailto:wlsadmin@uwo.ca).

## Abstract

The oxidation of C-H bonds to carbonyl functional groups using molecular oxygen (O<sub>2</sub>) is a desirable process as O<sub>2</sub> is environmentally benign and inexpensive. However, oxidations that employ O<sub>2</sub> have lower product selectivity, making it industrially unappealing. The metal complexes NiCl( $\pi$ -cinnamyl)(NHC) oxidize stoichiometrically with O<sub>2</sub> as the oxidant to selectively form the ketone and aldehyde products.

This thesis details the attempted catalysis with the NiCl( $\pi$ -allyl)(NHC) complex and the stoichiometric reactivity of NiCl( $\pi$ -allyl)(NHC) and NiCl( $\pi$ -cinnamyl)(NHC) complexes upon O<sub>2</sub> exposure. An investigation of the intermediate and decomposition species of the NiCl( $\pi$ -allyl)(NHC) complex was conducted. The complexes were found to be non-catalytic under various conditions, and the decomposition studies revealed rapid, complex reactivity. Low-temperature studies and DFT methods determined the formation of two intermediates and lead to a new proposed mechanism. The first intermediate is proposed to be an organoperoxo metallocycle, while the second is proposed to be a  $\mu$ -Cl dimer structure.

## Keywords

Nickel (II) complexes, *N*-heterocyclic carbene ligands, molecular oxygen, allylic C-H oxidation, variable temperature NMR spectroscopy, UV-visible spectroscopy, density functional theory

## Co-Authorship Statement

From the paper “Ligand Dynamics and Aerobic Allylic Oxidation with Bifunctional Ni (NHC) Complexes”, Scott Hendriks provided the data for entries 6-15 in Table 2. He also provided the  $^1\text{H}$  NMR evidence for the fate of nickel species, and determining the identities and yields of the decomposition products. The synthesis and characterization of the reported complexes were completed by Richard J. Hazlehurst, a former member of the Blacquiere group. The reported crystal structures were solved by Paul D. Boyle of Western University.

## Acknowledgments

First and foremost I would like to thank my supervisor, Dr. Johanna Blacquiere. When I started this project I had not been in a lab for over a year. Throughout the entire project, she was always willing to educate me in the finer points of the field, come to the lab to help through a particularly rough synthesis, and made sure that she always had time for one more quick question. She strived to not only help me with my synthetic techniques, but my presentation and writing skills also. Her support throughout the project, as well as her knowledge of the field, helped make this project possible. I am truly grateful for such an excellent supervisor.

I would also like to thank Dr. Viktor Staroverov for his assistance with the computational work that was performed. While this section of the project started a little bit later, his assistance was imperative in helping me work through some of the early stages of the analysis. Without his help, I would be short a chapter today.

Next, I would like to thank the support faculty and staff at Western University. I would like to thank in particular Dr. Mathew Willans, who helped with anything NMR related, including some interesting experiments. I would also like to thank Kristina Jurcic and Jasmine Wang for obtaining the MALDI-MS data that is presented in this work.

I would also like to thank all of the students of the Blacquiere group students, both current and past, that I have worked with over the last two years. I would especially like to thank the graduate students James Stubbs, Ava Behnia, David Bocking, and Helen Yoon for making the days in the lab better. I would especially like to thank Richard Hazlehurst, whose previous work on this project and guidance in the early days of my work were essential for the work presented.

Lastly, I would like to thank my friends, both inside and outside of graduate school, and my family for their encouragement and support for the last two years. Thank you for listening to my frustrations and celebrating my successes, or as much of them as you understood.

# Table of Contents

Abstract.....	i
Co-Authorship Statement.....	ii
Acknowledgments.....	iii
Table of Contents.....	iv
List of Tables.....	vii
List of Figures.....	viii
List of Schemes.....	xv
List of Abbreviations.....	xix
Chapter 1.....	1
1 Introduction.....	1
1.1 Oxidation Chemistry.....	1
1.2 Oxidation of C-H Bonds.....	1
1.3 One Step C-H Oxidation.....	2
1.3.1 Catalytic Allylic Oxidation to Carbonyl Products.....	2
1.4 Oxygen as the Oxidant.....	4
1.4.1 Catalytic Allylic Oxidation with O <sub>2</sub> .....	5
1.5 Metal-O <sub>2</sub> Reactivity.....	7
1.5.1 Nickel-O <sub>2</sub> Reactivity.....	8
1.5.2 Ni <sup>II</sup> -O <sub>2</sub> Reactivity.....	8
1.6 Oxygen Reactivity of NiCl( $\pi$ -allyl)NHC Complexes.....	11
1.7 Ni <sup>II</sup> -OH Reactivity.....	13
1.8 Oxidation of Asymmetric NiCl( $\pi$ -allyl)(NHC) Complexes.....	15
1.9 Project Goals.....	17
1.9.1 Determination of Optimal Oxidation and Catalysis Conditions.....	17

1.9.2	Study of Ni Decomposition Products and Reaction Intermediates Following Oxidation .....	17
Chapter 2	.....	19
2	Stoichiometric Oxidation of <b>5a</b> and <b>5b</b> and Catalysis of <b>4</b> .....	19
2.1	Stoichiometric Determination of Oxidation Products.....	19
2.2	Attempted Catalysis of Allylbenzene .....	22
2.3	Attempted Catalysis with Cinnamyl Pinacolborane as the Substrate .....	24
Chapter 3	.....	27
3	Analysis of Decomposition Products after Oxidation and Attempted Synthesis of Intermediate Structures .....	27
3.1	Determination of Intermediate Species by <sup>1</sup> H NMR Spectroscopy at Room Temperature .....	27
3.2	Determination of Inorganic Decomposition Products by X-ray Crystallography	30
3.3	Attempted Synthesis of Azide Substituted <b>5a</b> (11).....	33
Chapter 4	.....	38
4	Experimental Determination of Intermediate Species by UV-vis and <sup>1</sup> H NMR Spectroscopy .....	38
4.1	Determination of Intermediate Species by UV-vis Spectroscopy .....	38
4.2	Reversibility of Trapped Intermediates .....	43
4.3	Reactivity of Oxidation Intermediates .....	48
4.4	Investigation of Oxidation Intermediates by Variable Temperature of <sup>1</sup> H NMR Spectroscopy .....	53
Chapter 5	.....	62
5	Determination of Reaction Intermediates by Density Functional Theory and Time Dependent Density Functional Theory .....	62
5.1	Determination of Reaction Intermediates by Density Functional Theory .....	62
5.2	Time-Dependent DFT of Possible Oxidation Intermediates .....	75
6	Conclusions and Future Work.....	88
6.1	General Conclusions .....	88

6.2 Future Work .....	91
7 Experimental .....	94
References .....	107
Appendices .....	112
Curriculum Vitae .....	116

## List of Tables

Table 2.1 Product Yields for Stoichiometric Oxidation of 5a <sup>a</sup> .....	21
Table 2.2: Conditions Screened for the Attempted Catalytic Oxidation <sup>a</sup> .....	24



## List of Figures

Figure 1.1: Structure of (+)-quassin.....	3
Figure 1.2: Chemical structure of peribysin E.....	3
Figure 1.3: Proposed structure of the active site of the quercetinase enzyme in its resting state. ....	8
Figure 1.4: Representative structures of $\text{Ni}_2(\mu\text{-O})_2$ and $[\text{Ni-}\mu\text{OH}]_2$ dimers. ....	8
Figure 1.5: Structures of 2 and 3 as reported by Nam <i>et al.</i> ....	10
Figure 1.6: $\text{NiCl}(\eta^3\text{-allyl})(\text{ItBu})$ with the axial sites blocked by the sterically bulky tBu groups, leading to a loss of reactivity. ....	13
Figure 1.7: Proposed square pyramidal and trigonal bipyramidal $\text{Ni}^{\text{III}}$ -superoxo intermediates. ....	13
Figure 1.8: Reported reactivity of a $\text{Ni}^{\text{II}}$ -OH monomer by Holm <i>et al.</i> .....	14
Figure 1.9: $\text{Ni}^{\text{II}}$ -OH monomer reported by Borovik <i>et al.</i> stabilized by hydrogen bonding interactions from amine N-H moieties in the secondary coordination sphere.....	14
Figure 1.10: The structure of a $\text{Ni}^{\text{II}}$ -OH species stabilized by hydrogen bonding interactions, reported by Ghosh <i>et al.</i> .....	15
Figure 1.11: The three asymmetric $\text{NiCl}(\pi\text{-allyl})(\text{NHC})$ complexes used throughout this work. ....	16
Figure 2.1: Percent of cinnamyl pinacolborane remaining over 48 hours. Traces are: control (◆); $\text{O}_2$ (■); 1mol% 4 (▲); $\text{O}_2$ , 1 mol% 4 (●).....	26
Figure 3.1: $^1\text{H}$ NMR spectra in as-received $\text{MeCN-d}_3$ of a) 4 with dimethyl terephthalate, b) 4 with dimethyl terephthalate treated with $\text{O}_2$ , after 4 hours. Species are labelled as follows: $\text{H}[\text{NHC}]^+$ (●), an unknown species containing the NHC ligand (●), and dimethyl terephthalate (●).....	28

Figure 3.2: a) Product Formation over time in as-received MeCN- $d_3$ . b) Product Formation over Time in dry MeCN- $d_3$ . Product 8 (◆), H[NHC] <sup>+</sup> (■), Combined Yield (●). Conditions: 11.88 mM 4, 10.30 mM internal standard. ....	28
Figure 3.3: a) Oxidation Products over Time in as-received Pyridine- $d_5$ a. b) Oxidation Products over Time in Dry Pyridine- $d_5$ . Product X, (◆). H[NHC] <sup>+</sup> , (■). Product A + Product B, (●). Conditions: 14.3 mM 3a, 11.33 mM internal standard. ....	29
Figure 3.4: NMR stack plot of a) 5a in C <sub>6</sub> D <sub>6</sub> and b) 5a with NaN <sub>3</sub> in MeCN after 4 days, NMR spectrum in C <sub>6</sub> D <sub>6</sub> . Red dots (●) indicate new peaks, the blue (●) and black (●) dots were used in determining overall conversion. ....	34
Figure 3.5: Stacked IR spectra of 3b (solid line) and the azide substituted product 3c (dashed line). ....	35
Figure 3.6: Simulated (top) and obtained (bottom) fragment signals from the MALDI mass spectra of 11 with pyrene as the matrix: a) H[NHC] <sup>+</sup> , b) [Ni(NHC) <sub>2</sub> ] <sup>+</sup> , and c) [5a – cinnamyl] <sup>+</sup> .....	36
Figure 4.1: Structure of 4 with a) $\kappa^1$ -C NHC binding mode, and b) $\kappa^2$ -CN NHC binding mode.....	39
Figure 4.2: UV-Vis spectra of 5 mM 4 at: 20 °C (red); –65 °C (blue); and at 20 °C after having been cooled to –65 °C (purple). ....	40
Figure 4.3: Kinetics trace of 4 flushed with O <sub>2</sub> for 10 seconds over 2 hours. The reaction time between each trace is 20 minutes.....	41
Figure 4.4: UV-Vis spectra of Int. 1 warmed to –65 °C and monitored for one hour. The reaction time between each trace is 5 minutes.....	42
Figure 4.5: UV-Vis spectra of Int. 2 warmed to –30 °C for 30 minutes. The reaction time between each trace is 5 minutes.....	43

Figure 4.6: UV-Vis spectra of 5 mM <b>4</b> at $-78\text{ }^{\circ}\text{C}$ (red), 3 hours after $\text{O}_2$ addition at $-78\text{ }^{\circ}\text{C}$ (light blue), and after being sparged with $\text{N}_2$ . Traces were obtained every 5 minutes after $\text{N}_2$ addition for 100 minutes, and a final trace was obtained at 160 minutes. ....	44
Figure 4.7: Comparison of 5 mM <b>4</b> exposed to $\text{O}_2$ at $-78\text{ }^{\circ}\text{C}$ for two hours, then: sparged with $\text{N}_2$ for 30 seconds, left for 160 minutes (blue); Int. 2 (red). ....	45
Figure 4.8: UV-Vis spectra of <b>4</b> exposed to $\text{O}_2$ at $-78\text{ }^{\circ}\text{C}$ for two hours to give Int. 1 (blue), the sample was warmed to $-65\text{ }^{\circ}\text{C}$ for one hour to give Int. 2 (red), and cooled back to $-78\text{ }^{\circ}\text{C}$ for 30 minutes (green). ....	46
Figure 4.9: UV-Vis spectra of Int. 2, warmed to $-40\text{ }^{\circ}\text{C}$ and held for one hour (blue), the sample was warmed to $-30\text{ }^{\circ}\text{C}$ for 55 minutes to give the decomposition products (red), and cooled back to $-40\text{ }^{\circ}\text{C}$ for 15 minutes (green). ....	47
Figure 4.10: UV-Vis spectra of: 5mM <b>4</b> at $-78\text{ }^{\circ}\text{C}$ (red), Int. 1 (blue), and Int. 1 after 0.2 equivalent additions of DPH (orange, green, dark blue, purple, dark red, respectively). The reaction time between each trace is 10 minutes. The inset shows an expansion of the region between 400 nm and 460 nm. ....	49
Figure 4.11: Int. 2 (blue), with: 0.2 molar equivalence $\text{py}\cdot\text{HCl}$ (red), 0.4 molar equivalence $\text{py}\cdot\text{HCl}$ (black), and 0.6 molar equivalence $\text{py}\cdot\text{HCl}$ (green). The reaction time between each trace is 10 minutes. ....	52
Figure 4.12: Int. 2 (blue), with 0.6 molar equivalents $\text{py}\cdot\text{HCl}$ (red), 0.8 molar equivalents $\text{py}\cdot\text{HCl}$ (black), 1.0 molar equivalents $\text{py}\cdot\text{HCl}$ (green), and 1.2 molar equivalents $\text{py}\cdot\text{HCl}$ (orange). ....	53
Figure 4.13: Stacked $^1\text{H}$ NMR spectra of 10 mM <b>4</b> in $\text{DCM}-d_2$ with trimethoxybenzene as the internal standard a) at $-78\text{ }^{\circ}\text{C}$ , and b) after addition of $\text{O}_2$ and reaction for 2 h. at $-78^{\circ}\text{C}$ . ....	55
Figure 4.14: Pertinent region of the $^1\text{H}$ NMR spectrum of 10 mM <b>4</b> with a $\text{DCM}:\text{DCM}-d_2$ sealed capillary present at $-78\text{ }^{\circ}\text{C}$ a) before $\text{O}_2$ addition, and b) 2 hours after $\text{O}_2$ addition. ....	56
Figure 4.15: Formation of potential superoxo species from <b>4</b> and $\text{O}_2$ . ....	57

Figure 4.16: Crystal field d-orbital splitting of: a) tetrahedral Ni <sup>III</sup> , b) high-spin square pyramidal Ni <sup>III</sup> , c) low-spin square planar Ni <sup>III</sup> , and d) high-spin tetrahedral Ni <sup>II</sup> . .....	57
Figure 4.17: Stacked <sup>1</sup> H NMR spectra of 10 mM 4 in DCM- <i>d</i> <sub>2</sub> with trimethoxybenzene as an internal standard: a) at -78 °C before O <sub>2</sub> addition, b) -78 °C 2 hours after O <sub>2</sub> addition, and c) warmed to -65 °C for one hour. ● indicates propenal, ● is the broadened signal, and ● indicates the internal standard.....	59
Figure 4.18: <sup>1</sup> H NMR stack plot of 10 mM 4 with trimethoxybenzene as the internal standard, at a) 25 °C, b) 0 °C, c) -25 °C, d) -30 °C, e) -40 °C, f) -65 °C. ● indicates the position of the broadened signal, ● indicates propenal.....	60
Figure 4.19: Proposed intermediate structure of: a) Int. 1 and b) Int. 2.....	61
Figure 5.1: Ni-NHC complex used to model hydrogen-bonding interactions for computational methods. ....	63
Figure 5.2: Optimized structures for compound 4 used for thermodynamic analysis at -65 °C, with the corresponding calculated ΔG values shown below in kJmol <sup>-1</sup> . ....	63
Figure 5.3: Ni-O <sub>2</sub> adducts studied to determine the reaction pathway. ....	64
Figure 5.4: Thermodynamic plot for the conversion of structures I-III to the proposed Ni-O <sub>2</sub> adducts, IV and V. Numbers are energy differences from I in kJmol <sup>-1</sup> . ....	65
Figure 5.5: Structure of potential metallocycle intermediates VIII and IX. ....	66
Figure 5.6: Reaction coordinate showing different conformations of 4 with O <sub>2</sub> (I-III), Ni <sup>III</sup> -O <sub>2</sub> adducts IV and V, and the metallocycles VIII and IX. Numbers are energy differences from I in kJmol <sup>-1</sup> . ....	66
Figure 5.7: Structure of X. ....	67
Figure 5.8: Reaction coordinate of different conformations of 4 with O <sub>2</sub> (I-III), Ni <sup>III</sup> -O <sub>2</sub> adducts IV and V, metallocycles VIII and IX, and the propenal bound intermediate X. Numbers are energy differences from I in kJmol <sup>-1</sup> . Sigman's proposed reaction pathway (blue dash). Our proposed reaction pathway (red dash). ....	68

Figure 5.9: Proposed reaction pathway from a Ni <sup>III</sup> -superoxo species that forms the organoperoxo metallocycle <b>IX</b> and subsequent reactivity to <b>XI</b> . .....	69
Figure 5.10: Proposed monomeric Ni <sup>II</sup> -OH structures. ....	70
Figure 5.11: Reaction coordinate of the different conformations of <b>4</b> with O <sub>2</sub> (I-III), Ni <sup>III</sup> -O <sub>2</sub> adducts (IV and V), metallocycles (VIII and IX), propenal bound Ni <sup>II</sup> -OH (X), proposed monomeric Ni <sup>II</sup> -OH species after propenal release (XI-XIII). Numbers are energy differences from I in kJmol <sup>-1</sup> . Sigman's proposed reaction pathway (blue dash). Our proposed reaction pathway (red dash). .....	70
Figure 5.12: Potential dimeric structures studied. ....	71
Figure 5.13: Reaction coordinate depicting energy values for the different conformations of <b>4</b> with O <sub>2</sub> (I-III), Ni <sup>III</sup> -O <sub>2</sub> adducts (IV-V), metallocycles (VIII-IX), propenal-bound Ni <sup>II</sup> -OH (X), monomeric Ni <sup>II</sup> -OH structures (XI-XIII), and possible dimeric species (XV-XVII). Numbers are energy differences from I in kJmol <sup>-1</sup> . Sigman's proposed reaction pathway (blue dash). Our proposed reaction pathway (red dash). ....	72
Figure 5.14: Structure of XVIII .....	73
Figure 5.15: Reaction coordinate of the different conformations of <b>4</b> with O <sub>2</sub> (I-III), Ni <sup>III</sup> -O <sub>2</sub> adducts (IV and V), metallocycles (VIII and IX), propenal-bound Ni <sup>II</sup> -OH (X), monomeric Ni <sup>II</sup> -OH species (XI-XIII), dimer species (XV-XVII) and NiCl <sub>2</sub> (NHC) <sub>2</sub> (XVIII). Numbers are energy differences from I in kJmol <sup>-1</sup> . Sigman's proposed reaction pathway (blue dash). Our proposed reaction pathway (red dash). ....	73
Figure 5.16: Proposed reaction pathway for the oxidation of <b>4</b> based on DFT calculated ΔG values. ....	74
Figure 5.17: Structures chosen from Section 5.1 to be studied by TD-DFT methods.....	76
Figure 5.18: UV-Vis traces of <b>4</b> at -65 °C (blue), TD-DFT simulated trace of I (red), and TD-DFT simulated trace of II (green). ....	77

Figure 5.19: UV-vis spectrum of Int. 1 $-78\text{ }^{\circ}\text{C}$ (blue) and TD-DFT simulation of end-on superoxo structure IV (red).	78
Figure 5.20: UV-vis spectrum of Int. 1 $-78\text{ }^{\circ}\text{C}$ (blue) and TD-DFT simulation of side-on superoxo V (red).	79
Figure 5.21: UV-vis spectrum of Int. 1 at $-78\text{ }^{\circ}\text{C}$ (blue) and TD-DFT simulation of metallocycle VIII (red).	80
Figure 5.22: UV-Vis trace of Int. 2 at $-65\text{ }^{\circ}\text{C}$ (blue) and TD-DFT simulation of structure X (red).	81
Figure 5.23: UV-vis spectrum of Int. 2 at $-65\text{ }^{\circ}\text{C}$ (blue) and TD-DFT simulation of XIII (red).	82
Figure 5.24: UV-vis spectrum of Int. 2 at $-65\text{ }^{\circ}\text{C}$ (blue), TD-DFT simulation of X (red), and TD-DFT simulation of XIII (green).	83
Figure 5.25: UV-vis spectrum of Int. 2 at $-65\text{ }^{\circ}\text{C}$ (blue) and TD-DFT spectrum of XVII (red).	84
Figure 5.26: UV-vis spectrum of Int. 2 at $-65\text{ }^{\circ}\text{C}$ (blue) and TD-DFT spectrum of dimer species XVI (red).	85
Figure 5.27: Obtained UV-vis spectrum of Int. 2 at $-65\text{ }^{\circ}\text{C}$ (blue) and the TD-DFT simulated spectrum of XV (red).	86
Figure 6.1: Proposed reaction of a $\text{Ni}^{\text{III}}\text{-O}_2$ with $\text{PPh}_3$ to form $\text{OPPh}_3$ .	92
Figure 6.2: Proposed bi- and tridentate ligands to be used for the stabilization of Int. 2.	93
Figure 0.1: $^1\text{H}$ NMR spectrum of Int. 2 at $-65\text{ }^{\circ}\text{C}$ in $\text{DCM-}d_2$ with a capillary tube of 1:8 $\text{DCM}:\text{DCM-}d_2$ present. The signal at 5.32 ppm is DCM, while the signal at 5.44 ppm is the paramagnetically shifted DCM.	113

Figure 0.2:  $^1\text{H}$  NMR spectrum of decomposed 4 at 25 °C 3.5 h after  $\text{O}_2$  addition at  $-78$  °C in  $\text{DCM-}d_2$  with a capillary tube of 1:8  $\text{DCM}:\text{DCM-}d_2$  present. The signal at 5.32 ppm is  $\text{DCM}$ , while the signal at 5.44 ppm is paramagnetically shifted  $\text{DCM}$ . ..... 113

Figure 0.3: Obtained UV-vis spectrum of 4 at  $-65$  °C (blue) and TD-DFT simulated spectrum of III (red). ..... 114

Figure 0.4: Obtained UV-vis spectrum of Int. 2 at  $-65$  °C (blue) and TD-DFT simulated spectrum of XI (red). ..... 114

Figure 0.5: Obtained UV-vis spectrum of Int. 2 at  $-65$  °C (blue) and TD-DFT simulated spectrum of XII (red). ..... 115

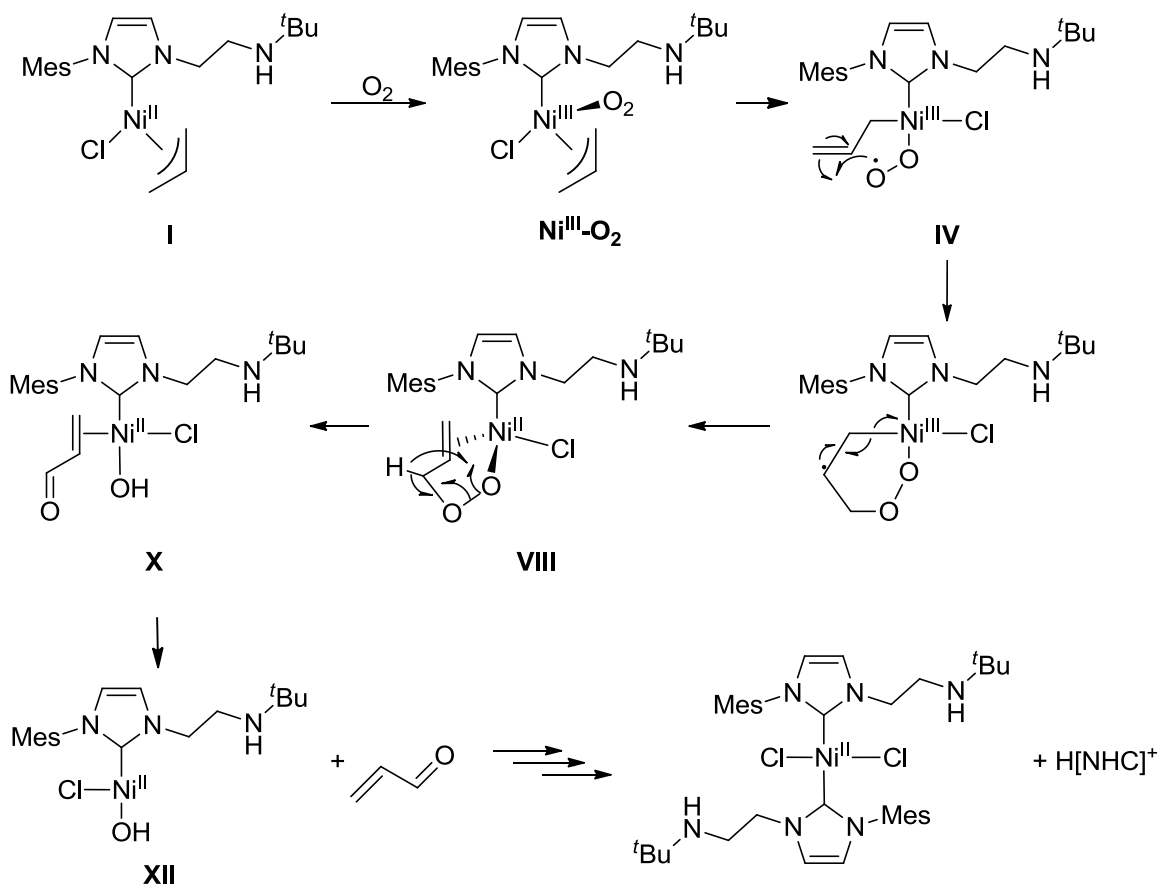
## List of Schemes

Scheme 1.1: Representative reaction of a one-electron oxidation reaction. [R] = reductant, [O] = oxidant, e <sup>-</sup> = electron.....	1
Scheme 1.2: Example oxidation process, showing the conversion of a C(sp <sup>3</sup> )-H bond to a carbonyl bond through Swern oxidation.....	2
Scheme 1.3: The formation of a new ketone group from an allylic C-H group, reported by Jiang <i>et al.</i> Blue atoms indicate site of reaction. TBHP = tert-butyl hydroperoxide.....	3
Scheme 1.4: Allylic oxidation reaction performed by Sha <i>et al.</i> in the total synthesis of peribysin E. Blue atoms indicate site of reaction. TBHP = tert-butyl hydroperoxide.....	4
Scheme 1.5: Reaction scheme for the conversion of allyl benzene to CA as reported by Fu <i>et al.</i> Blue atoms indicate the site of the reaction. ....	4
Scheme 1.6: Possible products from the reaction between cyclohexene and O <sub>2</sub> .....	5
Scheme 1.7: Reaction between cyclohexene and O <sub>2</sub> using Fukuzumi <i>et al.</i> 's iron catalyst, leading to four unique oxidized products.....	6
Scheme 1.8: Reactivity observed by Liu <i>et al.</i> with their manganese catalyst showing high selectivity for the epoxide product.....	6
Scheme 1.9: Optimized catalytic reaction of cyclohexene with a bimetallic Ni <sup>II</sup> catalyst, reported by Salavati-Niasari. ....	7
Scheme 1.10: Formation of Baldwin <i>et al.</i> 's O <sub>2</sub> reactive complex.....	9
Scheme 1.11: Oxygenation reaction observed by Kodama <i>et al.</i> of a pentacoordinate Ni <sup>II</sup> complex.....	10
Scheme 1.12: Sigman's reported oxidation products of a NiCl(η <sup>3</sup> -allyl)(iPr) complex.....	11
Scheme 1.13: Proposed reaction mechanism for the formation of propenal from oxygenation of NiCl(η <sup>3</sup> -allyl)(iPr). ....	12



Scheme 1.14: Observed reactivity of KOtBu with Borovik <i>et al.</i> 's reported Ni <sup>II</sup> -OH species. .....	15
Scheme 1.15: Target catalytic reaction for 4. ....	17
Scheme 2.1: Stoichiometric aerobic oxidation of <b>5a</b> . ....	19
Scheme 2.2: Proposed Ni <sup>III</sup> -superoxo intermediates after O <sub>2</sub> addition to <b>5a</b> in pyridine. Intermediate structures are shown as square pyramidal, but it is possible for them to adopt a trigonal bipyramidal structure. ....	20
Scheme 2.3: Proposed Reaction of LiHMDS with <b>5a</b> . ....	21
Scheme 2.4: Attempted catalytic oxidation of allyl benzene. ....	22
Scheme 2.5: Attempted catalytic oxidation with cinnamyl pinacolborane as the substrate. ..	25
Scheme 3.1: Oxidation of 4 in MeCN- <i>d</i> <sub>3</sub> with dimethyl terephthalate present. ....	27
Scheme 3.2: Observed products after O <sub>2</sub> addition to 4 in MeCN. ....	31
Scheme 3.3: Proposed water source. ....	32
Scheme 3.4: Observed products after O <sub>2</sub> addition to 4 in THF. ....	32
Scheme 3.5: Attempted azide substitution reaction of 5a (32.8 mM) with NaN <sub>3</sub> (36.2 mM). ....	33
Scheme 3.6: Attempted substitution reaction of NaN <sub>3</sub> in MeCN. ....	34
Scheme 4.1: Proposed reaction mechanism by Sigman <i>et al.</i> Boxed structures indicate high interest intermediates that are sought to be trapped out by low temperature studies. ....	38
Scheme 4.2: General reaction scheme for low temperature UV-Vis experiments. ....	39
Scheme 4.3: Formation of Int. 1 and N <sub>2</sub> sparging to test for reversibility of O <sub>2</sub> binding, expected reactivity if Int. 1 was a Ni <sup>III</sup> -superoxo species ([Ni]-O-O•). ....	44
Scheme 4.4: Proposed reaction to assess the thermal reversibility of <b>Int. 2</b> from <b>Int. 1</b> . ....	46

Scheme 4.5: Proposed reactivity to assess the thermal reversibility of the decomposition products to Int. 2. ....	47
Scheme 4.6: Reaction pathway that is observed upon aerobic oxidation of 4.....	48
Scheme 4.7: Expected hydrogen atom transfer from DPH to a Ni <sup>III</sup> -superoxo ([Ni]-O-O <sup>•</sup> ) species to give azobenzene and a Ni-hydroperoxo.....	48
Scheme 4.8: Proposed reaction between a Ni <sup>II</sup> -OH monomer and py•HCl.....	50
Scheme 4.9: Proposed reactivity between a Ni <sup>II</sup> -OH and py•HCl.....	50
Scheme 4.10: Potential reaction of the secondary amine on the NHC ligand with Ni <sup>II</sup> -OH (C) and py•HCl to form dimer species G. ....	51
Scheme 4.11: Potential reaction of the secondary amine on the NHC ligand with Ni <sup>II</sup> -OH (C) and py•HCl to form the Ni-aquo complex D'.....	51
Scheme 4.12: Proposed decomposition pathway upon addition of excess py•HCl to Int. 2. Py = pyridine.....	53
Scheme 4.13: Reaction of 10 mM 4 with O <sub>2</sub> to determine the identities of the Ni oxidation intermediates. IS = 1,3,5-trimethoxy benzene. ....	54



Scheme 6.1: Proposed alternate oxidation pathway of 4..... 91

## List of Abbreviations

AU = Absorbance units

MeCN = Acetonitrile

$pK_a$  = Acid dissociation constant

Å = Angstrom =  $10^{-10}$  meters

ATR = Attenuated total reflectance

B3LYP = Becke 3 Lee Yang Parr

$S_N^2$  = Bimolecular nucleophilic substitution

$\mu_B$  = Bohr magneton

$\mu$  = Bridging ligand

$t$ Bu = *tert*-Butyl

TBHP = *tert*-Butyl hydroperoxide

°C = degrees Celsius

CA = Cinnamaldehyde

CMD = Concerted metalation deprotonation

COSY = Correlation spectroscopy

$\text{cm}^3\text{mol}^{-1}$  = Cubic centimeters per mole

cod = 1,5-Cyclooctadiene

DFT = Density functional theory

$\kappa$  = Denticity

MeCN- $d_3$  = Deuterated acetonitrile

DCM- $d_2$  = Deuterated dichloromethane

DDQ = 2,3-Dichloro-5,6-dicyano-1,4 benzoquinone

DCM = Dichloromethane

DME = Dimethoxyethane

DMF = Dimethylformamide

DPH = 1,2-Diphenyl hydrazine

$\mu_{\text{eff}}$  = Effective magnetic moment

EPR = Electron paramagnetic resonance

EXAFS = Extended X-ray absorption fine structure

FID = Flame ionization detector

FT = Fourier transform

GC = Gas chromatography

$\Delta G$  = Gibbs free energy

g = Gram

$\eta$  = Hapticity

Hz = Hertz

h = Hour

HAT = Hydrogen atom transfer

$\dot{\text{I}}\text{Pr}$  = 1,3-*bis*(2,6-diisopropylphenyl)imidazole-2-ylidene

IR = Infrared

IS = Internal standard

K = degrees Kelvin

$\text{kJmol}^{-1}$  = Kilojoules per mole

LiHMDS = Lithium hexamethyldisilazide

MS = Mass spectrometry

MALDI = Matrix assisted laser desorption ionization

MHz = Megahertz

Mes = Mesityl

Me = Methyl

MeTHF = 2-Methyl tetrahydrofuran

$\mu\text{L}$  = Microliter

mg = Milligram

mL = Milliliter

mM = Millimolar

mmol = Millimole

min = Minute

M = Molar

mol = Mole

nm = Nanometers

NHC = *N*-heterocyclic carbene

NMR = Nuclear magnetic resonance

ppm = Parts per million

Ph = Phenyl

PVK = Phenyl vinyl ketone

$^1\text{H}$  = proton

py = Pyridine

py•HCl = Pyridinium chloride

S = Spin State

SQUID = Superconducting quantum interference device

$\text{O}_2^{\bullet -}$  = Superoxo

THF = Tetrahydrofuran

TD-DFT = Time-dependent density functional theory

TOF = Time of flight

O=PEt<sub>3</sub> = Triethyl phosphine oxide

O=PPh<sub>3</sub> = Triphenyl phosphine oxide

UV-vis = Ultraviolet-visible

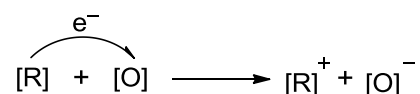
$\lambda$  = Wavelength

## Chapter 1

### 1 Introduction

#### 1.1 Oxidation Chemistry

Oxidation processes are widespread throughout industry and academia, leading to value-added products and new chemicals.<sup>1-3</sup> In an oxidation reaction, the starting material loses at least one electron and becomes more positively charged (Scheme 1.1). Oxidants are required to facilitate these processes and accept the electron(s) from the reactant.

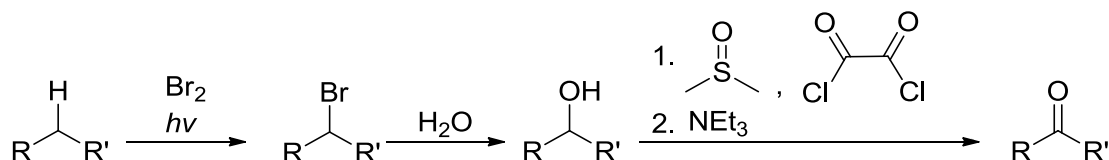


Scheme 1.1: Representative reaction of a one-electron oxidation reaction. [R] = reductant, [O] = oxidant, e<sup>-</sup> = electron

#### 1.2 Oxidation of C-H Bonds

The oxidation of hydrocarbons can lead to a multitude of possible products, including alcohols, epoxides, and peroxides.<sup>4, 5, 6</sup> Of particular interest is the conversion of C(sp<sup>3</sup>)-H bonds to carbonyl (C=O) bonds. Traditional organic methods have a plethora of options to achieve this desired conversion. An example three-step oxidation reaction to obtain the related carbonyl products from a hydrocarbon is shown below (Scheme 1.2). First, light-activated bromination of the hydrocarbon is performed, followed by a S<sub>N</sub><sup>2</sup> reaction with H<sub>2</sub>O to result in the alcohol, and then a Swern oxidation is performed to afford the final carbonyl product.





Scheme 1.2: Example oxidation process, showing the conversion of a C(sp<sup>3</sup>)-H bond to a carbonyl bond through Swern oxidation.

The above example was chosen as it highlights the two main concerns of traditional oxidation strategies; the number of synthetic steps (3), and the choice of oxidant (oxalyl chloride). As the reaction occurs over a number of unique steps, the overall yield of the final product may decrease. If it does, then the atom economy decreases, and generates more chemical waste at each step.<sup>7</sup> These three factors result in an increased cost of the final product. The oxidant chosen to perform these oxidations is also a factor to consider, as typically the oxidants used for the oxidation reactions or their byproducts are toxic to humans. In the above reaction, the oxalyl chloride is corrosive and toxic to human health, and also reacts with water to form CO<sub>2</sub> and CO gas. Other common oxidants that are employed include *tert*-butyl hydroperoxide (flammable),<sup>8-9</sup> Cr<sup>VI</sup>O<sub>3</sub> (toxic),<sup>10</sup> and 2,3-dichloro-5,6-dicyano-1,4-benzoquinone (DDQ) (the reduced form of DDQ is presumably carcinogenic).

### 1.3 One Step C-H Oxidation

Catalysis has previously been employed to convert C-H bonds to the related carbonyl products in one synthetic step, reducing the amount of waste and decreasing the number of unique synthetic steps. The examples discussed below are examples of transition metal complexes that catalyze the oxidation of the C-H bonds.

#### 1.3.1 Catalytic Allylic Oxidation to Carbonyl Products

Due to the high bond strength of C(sp<sup>3</sup>)-H bonds (439 kJmol<sup>-1</sup>), research has typically focused on benzylic or allylic C(sp<sup>3</sup>)-H bonds (361.1 kJmol<sup>-1</sup> and 377 kJmol<sup>-1</sup>, respectively).<sup>2, 11-12</sup> The catalytic transformation typically requires additional base present at the outset. The catalysts that are commonly used are chromium<sup>13</sup> or palladium<sup>14-15</sup>

complexes, although copper<sup>16</sup> has also shown the desired reactivity. The examples here represent only a small selection of these transformations.

First, Jiang *et al.* reported the total synthesis of (+)-quassin (Figure 1.1).<sup>13</sup> One of the reported intermediate steps was the allylic C-H oxidation of a cyclohexene derivative (Scheme 1.3). The reaction used Cr(CO)<sub>6</sub> as a catalyst and 70% *tert*-butyl hydroperoxide (TBHP) as the oxidant, and proceeded in high yield. However, TBHP is highly flammable. The reaction scheme shown below followed a previously reported mechanism.<sup>17</sup>

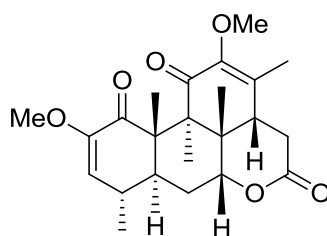
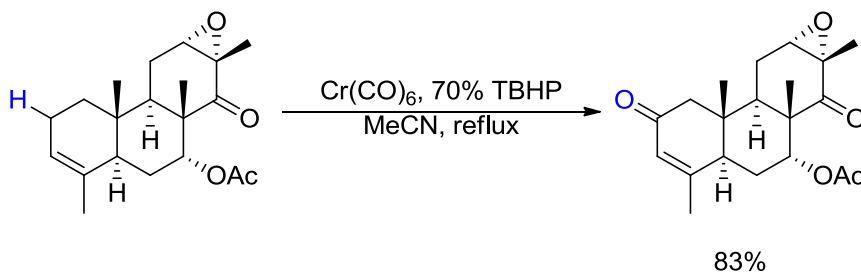


Figure 1.1: Structure of (+)-quassin



Scheme 1.3: The formation of a new ketone group from an allylic C-H group, reported by Jiang *et al.* Blue atoms indicate site of reaction. TBHP = *tert*-butyl hydroperoxide.

A second example comes from Sha *et al.*, who reported the total synthesis of peribysin E (Figure 1.2).<sup>14</sup>

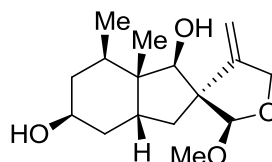
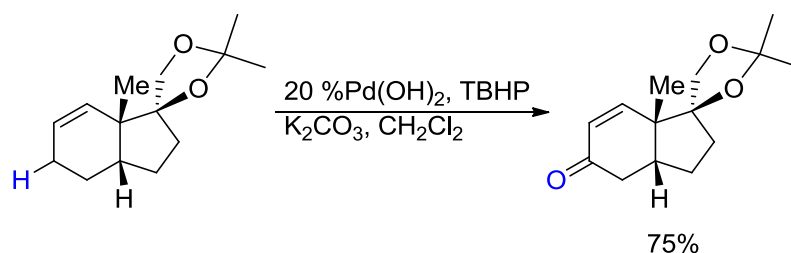


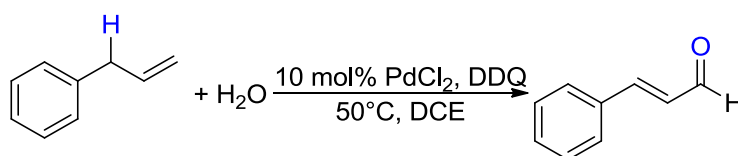
Figure 1.2: Chemical structure of peribysin E.

To form one of the necessary intermediate structures, Sha *et al.* performed a catalytic allylic oxidation, using a palladium hydroxide catalyst, and TBHP as the oxidant (Scheme 1.4). Potassium carbonate was also present at the outset of the reaction, and aided in the final step to form the carbonyl. Once again, the highlighted transformation was previously reported.<sup>17</sup>



Scheme 1.4: Allylic oxidation reaction performed by Sha *et al.* in the total synthesis of peribysin E. Blue atoms indicate site of reaction. TBHP = tert-butyl hydroperoxide.

An example from Fu *et al.* shows the catalytic conversion of allyl benzene and water to cinnamaldehyde (**CA**) could be accomplished in a single step.<sup>18</sup> Once again, a palladium catalyst was employed, with DDQ as the oxidant, and water as the oxygen atom source (Scheme 1.5).



Scheme 1.5: Reaction scheme for the conversion of allyl benzene to **CA** as reported by Fu *et al.* Blue atoms indicate the site of the reaction.

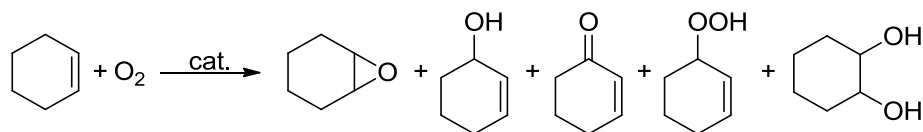
## 1.4 Oxygen as the Oxidant

An alternate oxidant to consider is molecular oxygen ( $O_2$ ) as it is readily accessible and poses limited concern to human health. However,  $O_2$  does promote the combustion of other materials, and the solvents chosen for homogeneous catalysis are usually flammable.<sup>19</sup> This safety concern can be alleviated in academic settings due to the smaller size of the reactions, but industrial applications pose a challenge.<sup>20</sup> The amount of  $O_2$  required in an industrial reactor, coupled with the reaction temperature and possible

pressure, make the reactions unfeasible from a safety perspective. Flow reactors, where the chemical reaction takes place through a continuously flowing tube, can alleviate many of these problems, as the flow reactor design allows for better temperature and pressure control.<sup>21</sup> Another strategy that can be used to overcome these challenges is through the use of dilute air, which is a mixture of O<sub>2</sub> and N<sub>2</sub>, with the mixture being 5-8% O<sub>2</sub>.<sup>22</sup> While there are limited aerobic oxidations used in the fine chemical industry, the discoveries made in the optimization and implementation of reactor design justifies the continued research for aerobic catalysts.

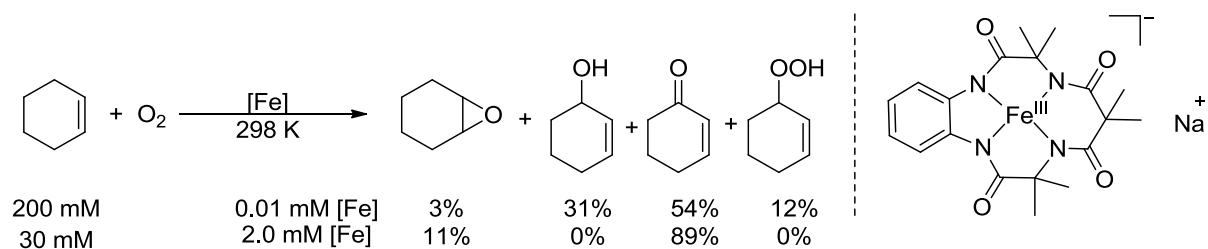
### 1.4.1 Catalytic Allylic Oxidation with O<sub>2</sub>

O<sub>2</sub> is a desirable oxidant as it is readily available and poses limited human health hazards, but suffers from lower selectivity of the final products.<sup>1, 3</sup> O<sub>2</sub> typically reacts through reduced oxygen species, O<sub>2</sub><sup>•-</sup>, after activation by the transition metal catalyst. This radical species is able to promote a wider range of reactivity leading to a multitude of products.<sup>23</sup> As a result of this increased reactivity, a benchmark substrate is required so as to ascertain the selectivity of a catalytic reaction with O<sub>2</sub> as the oxidant. Cyclohexene is a commonly used substrate, as there are a variety of known possible products that can form (Scheme 1.6).<sup>24</sup> A variety of metal complexes have been examined to determine their catalytic properties as well as the selectivity using this system. Typically, these systems employ first-row transition metals such as manganese or cobalt.<sup>25-26</sup> These catalysts commonly employ electron-donating ligands around the metal center to achieve the desired reactivity. The choice of catalyst and reaction conditions will favour the formation of different products, as these choices can influence the reactivity of O<sub>2</sub><sup>•-</sup> and cause certain reaction pathways to become more favorable than others. As a result, there is no “best” catalyst for the allylic oxidation with O<sub>2</sub>. Below are three catalytic examples that do show high selectivity for one of the oxidized products.



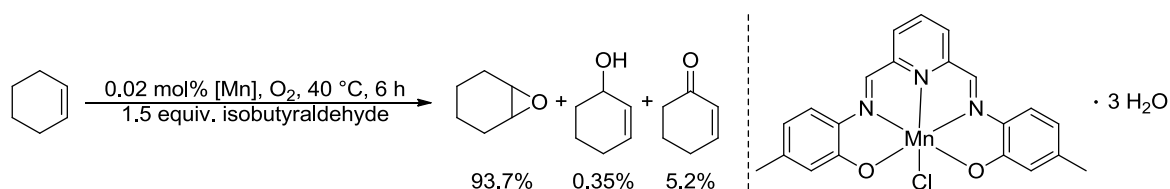
Scheme 1.6: Possible products from the reaction between cyclohexene and O<sub>2</sub>.

Fukuzumi *et al.* demonstrated that the reactions between cyclohexene and O<sub>2</sub> in the presence of an Fe<sup>III</sup>-tetraamido macrocyclic catalyst leads to the corresponding epoxide, alcohol, ketone, and peroxide products (Scheme 1.7).<sup>27</sup> The selectivity of the reaction could be improved for the ketone product by either decreasing the starting concentration of cyclohexene, or increasing the catalyst loading.



Scheme 1.7: Reaction between cyclohexene and O<sub>2</sub> using Fukuzumi *et al.*'s iron catalyst, leading to four unique oxidized products.

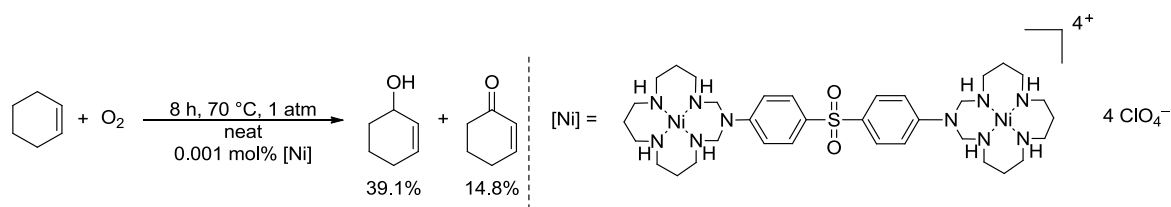
Liu *et al.* also demonstrated the conversion of cyclohexene to various products upon exposure to O<sub>2</sub> (Scheme 1.8).<sup>28</sup> The Mn<sup>II</sup>-pyridine Schiff base catalyst favors the formation of the epoxide product, and the alcohol and ketone byproducts were only observed in trace to minimal amounts.



Scheme 1.8: Reactivity observed by Liu *et al.* with their manganese catalyst showing high selectivity for the epoxide product.

Lastly, Salavati-Niasari demonstrated the conversion of cyclohexene to the corresponding ketone and alcohol products upon exposure to O<sub>2</sub> (Scheme 1.9).<sup>29</sup> This catalytic reaction used a bimetallic Ni<sup>II</sup> complex, with both metal centers bound to a tetradentate ligand and an organic linker. Excitingly, the catalytic reaction proceeded with catalyst loadings of

only 0.001 mol%. While the reaction occurred successfully, there is lower overall conversion compared to the two systems above.



Scheme 1.9: Optimized catalytic reaction of cyclohexene with a bimetallic Ni<sup>II</sup> catalyst, reported by Salavati-Niasari.

## 1.5 Metal-O<sub>2</sub> Reactivity

Research into metal-O<sub>2</sub> reactivity has largely been influenced by research of oxygen reactive enzymes, which typically use copper or iron atoms as the reactive metal centers.<sup>30-31</sup> Cytochrome c oxidase is one of the most famous O<sub>2</sub> reactive enzymes, which catalyzes the conversion of O<sub>2</sub> to H<sub>2</sub>O through active sites that contain Cu and Fe atoms.<sup>32-33</sup> Hemoglobin is also a well-known O<sub>2</sub> reactive protein which utilizes Fe atoms that are responsible for O<sub>2</sub> transportation from the lungs to the rest of the body.

By contrast, there are few Ni-based enzymes that react with O<sub>2</sub>, which decreases the driving force for the synthetic chemistry analysis of Ni-O<sub>2</sub> reactivity. One example of a nickel-containing enzyme that is O<sub>2</sub> reactive is bacterial quercetinase.<sup>34</sup> Quercetinase catalyzes the breakdown of quercetin (3,5,7,3',4'-pentahydroxyflavone), which is found in decomposing plant matter (Figure 1.3). In its resting state, crystalline quercetinase is a dimeric protein with two Ni<sup>II</sup> active sites. The nickel atoms are bound by three histidine residues, a glutamic acid residue, and two water molecules, resulting in an overall octahedral structure. After quercetinase was exposed to both quercetin and O<sub>2</sub>, it was found that the O<sub>2</sub> was bound side-on to the nickel center and perpendicular to the quercetin molecule. The oxygen atoms were both found to have a Ni-O bond of 2.4 Å, and an O-O bond length of 1.3 Å. This bond length could account for either a Ni<sup>II</sup>-superoxo species<sup>35</sup> or a Ni<sup>III</sup>-peroxo species<sup>36</sup>. Conclusive evidence of the Ni-O<sub>2</sub> binding mode is still underway.

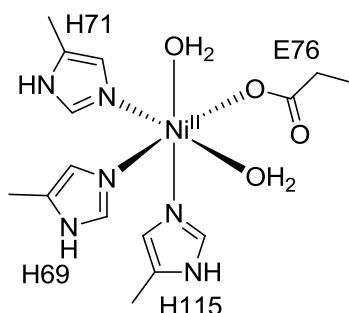


Figure 1.3: Proposed structure of the active site of the quercetinase enzyme in its resting state.

### 1.5.1 Nickel-O<sub>2</sub> Reactivity

Nickel has become a metal of interest for catalysis as it is cheaper and more readily abundant than palladium (\$54.10 for 50 g NiCl<sub>2</sub>, and \$66.50 for 1 g PdCl<sub>2</sub>, prices from Sigma-Aldrich). However, nickel has been previously labelled the “spirited horse” of catalysis, in that it can be difficult to observe or control the desired reactivity.<sup>37</sup> However, Ni can provide unique reaction pathways, such as one-electron processes (e.g. Ni<sup>II</sup> to Ni<sup>III</sup>).<sup>38-39</sup> Nickel has been known to react with O<sub>2</sub> primarily in its Ni<sup>0</sup> and Ni<sup>I</sup> oxidation states.<sup>36, 40-41</sup> These reactions typically lead to Ni<sub>2</sub>-(μO)<sub>2</sub> or [Ni-(μ-OH)]<sub>2</sub> dimers, as shown in Figure 1.4.

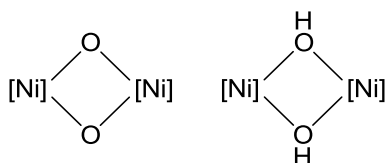


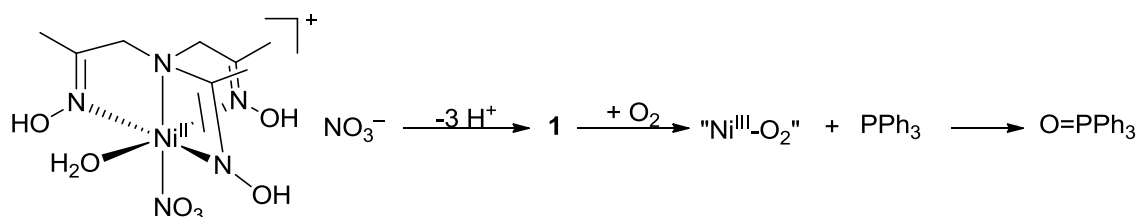
Figure 1.4: Representative structures of Ni<sub>2</sub>(μ-O)<sub>2</sub> and [Ni-μOH]<sub>2</sub> dimers.

### 1.5.2 Ni<sup>II</sup>-O<sub>2</sub> Reactivity

Stoichiometric reactions of Ni<sup>II</sup> complexes with O<sub>2</sub> are not commonly seen in the literature, and this is in part due to the difficulty in oxidizing Ni<sup>II</sup> to Ni<sup>III</sup>.<sup>40</sup> The oxidation potential of Ni<sup>II</sup> to Ni<sup>III</sup> is more positive than the reduction potential of O<sub>2</sub>, leading to a lack of reactivity. This can be overcome by using electron donating ligands, which lowers the oxidation potential of the Ni<sup>II/III</sup> couple such that oxidation by O<sub>2</sub> becomes thermodynamically favorable.<sup>40</sup> Typically, multi-dentate ligands have been used to

accomplish this,<sup>42-43</sup> although *N*-heterocyclic carbenes (NHCs) have also been shown to be effective electron donating ligands.<sup>44-45</sup>

Baldwin *et al.* reported the synthesis of a Ni<sup>II</sup> complex bearing a tetradentate ligand.<sup>46</sup> Three deprotonation steps were performed on the starting complex to give intermediate **1**, which was found to be O<sub>2</sub> reactive. Upon exposure of **1** to O<sub>2</sub> a new complex was observed and proposed to be a “Ni<sup>III</sup>-O<sub>2</sub>” complex (Scheme 1.10). This Ni<sup>III</sup>-O<sub>2</sub> complex was observed by ultraviolet-visible (UV-vis) and electron paramagnetic resonance (EPR) spectroscopy, as well as by the reactivity of the product with PPh<sub>3</sub>. When excess PPh<sub>3</sub> is added to the “Ni<sup>III</sup>-O<sub>2</sub>”, an oxygen-atom transfer reaction is observed, forming O=PPh<sub>3</sub> (Scheme 1.10).



Scheme 1.10: Formation of Baldwin *et al.*'s O<sub>2</sub> reactive complex.

Nam *et al.* later reported on the synthesis and characterization of both an end-on Ni<sup>II</sup>-superoxo (**2**) and a side-on Ni<sup>III</sup>-peroxo (**3**) using a tetradentate ligand and H<sub>2</sub>O<sub>2</sub> as the oxidant (Figure 1.5).<sup>47</sup> While the reagent for this reaction is not O<sub>2</sub>, it is still an important result to discuss, as both complexes were characterized by UV-vis, EPR, and Raman spectroscopy, as well as X-ray crystallography. From the UV-vis spectrum of **2**, there was an intense band at 339 nm, and two weak bands at 416 nm and 684 nm. Complex **2** was also found to undergo reactivity with PEt<sub>3</sub>, forming O=PEt<sub>3</sub> following second-order kinetics. From the UV-vis spectrum of **3**, there are two shoulders at ~350 nm and ~420 nm, and a weak band at ~650 nm. From the crystal structure analysis, it was found that **3** adopts a pseudo-octahedral geometry.



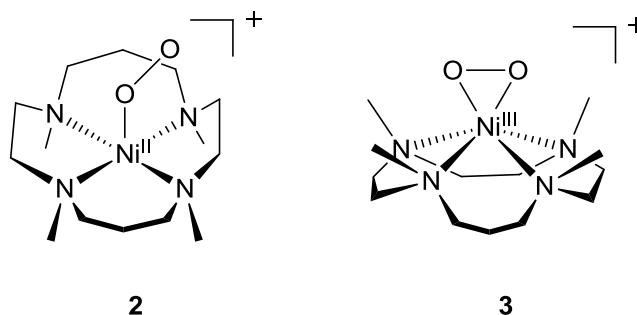
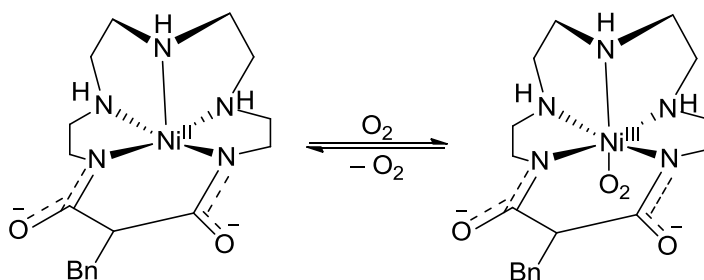


Figure 1.5: Structures of **2** and **3** as reported by Nam *et al.*

Lastly, Kodama *et al.* reported a Ni<sup>III</sup>-O<sub>2</sub> adduct starting from a Ni<sup>II</sup> complex.<sup>48</sup> After exposing a pentacoordinate Ni<sup>II</sup> complex to air, a color change from pink to brown was observed, and the product was studied by UV-vis spectroscopy, proton nuclear magnetic resonance (<sup>1</sup>H NMR) spectroscopy, and cyclic voltammetry (Scheme 1.11). The reaction was also found to be reversible when the product was placed under vacuum.

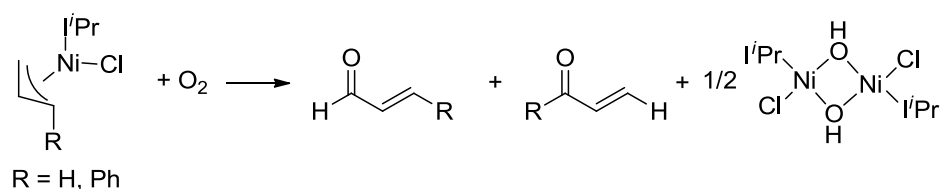


Scheme 1.11: Oxygenation reaction observed by Kodama *et al.* of a pentacoordinate Ni<sup>II</sup> complex.

From the UV-vis spectrum, there is a peak wavelength value,  $\lambda_{\text{max}}$ , of 310 nm. This value is comparable to the  $\lambda_{\text{max}}$  obtained for the related Ni<sup>III</sup> complex that was oxidized by electrochemical methods ( $\lambda_{\text{max}} = 300$  nm). The starting Ni<sup>II</sup> complex was paramagnetic, and exhibited a magnetic susceptibility of 2.83  $\mu_{\text{B}}$ . This value remained unchanged after oxygenation; although a color change was observed. This was believed to be a result of weak interactions of two unpaired electrons ( $S = 1$ ) between the Ni<sup>III</sup> with the superoxide ion. Instead of formal oxidation by O<sub>2</sub> however, it was suggested that the cause of the reaction was through polar solvation effects of water, as it would facilitate the formation of the charged products (Ni<sup>III</sup>-O<sub>2</sub><sup>-</sup>).

## 1.6 Oxygen Reactivity of NiCl( $\pi$ -allyl)NHC Complexes

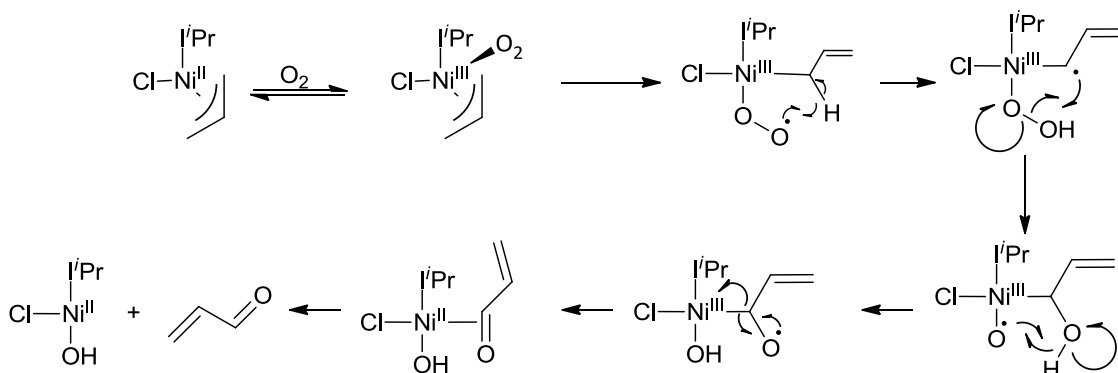
A ligand class that is highly electron donating is the NHCs, which are also highly tunable through their nitrogen-bound substituents.<sup>44-45</sup> This allows for a large library of potential ligands that can be used to achieve the desired oxygen reactivity of Ni<sup>II</sup>. Of particular interest was the system reported by Sigman *et al.* in which a NiCl( $\eta^3$ -allyl)NHC (NHC: <sup>i</sup>Pr; 1,3-bis(2,6-diisopropylphenyl)imidazole-2-ylidene) was exposed to O<sub>2</sub> and formed the corresponding carbonyl products with no observation of epoxide, alcohol, or peroxide products (Scheme 1.12).<sup>49</sup> This chemical selectivity was determined by repeating the oxidation reaction with an  $\eta^3$ -cinnamyl group and analyzing the products by <sup>1</sup>H NMR spectroscopy and mass spectrometry (MS). The observed products were cinnamaldehyde (CA) and phenyl vinyl ketone (PVK). This reaction overcomes one of the main problems observed when O<sub>2</sub> is used for organic transformations (i.e. poor selectivity). The nickel based byproduct is a Ni<sup>II</sup>- $\mu$ OH dimer, and was characterized by <sup>1</sup>H NMR spectroscopy, mass spectrometry, and X-ray crystallography. Stability tests of the Ni- $\mu$ OH dimer found that it decomposed if it was left in solution over several days. The observation of the dimer species indicates that during the reaction, a Ni<sup>II</sup>-OH is formed as an unstable intermediate, and subsequently stabilizes itself through dimerization. Lastly, Sigman investigated the initial kinetics of O<sub>2</sub> binding through UV-vis spectroscopy. It was found that the complex displayed saturation behavior, which is consistent with reversible O<sub>2</sub> binding followed by an irreversible rate-limiting step.



Scheme 1.12: Sigman's reported oxidation products of a NiCl( $\eta^3$ -allyl)(<sup>i</sup>Pr) complex.

The suggested reaction mechanism is shown below (Scheme 1.13). First, oxygen reversibly coordinates to the nickel center, forming an activated five-coordinate species. Next, the oxygen atom abstracts a hydrogen atom from the  $\kappa^1$  carbon atom of the allyl, forming a nickel-hydroperoxo species. The carbon based radical then abstracts the OH

group from the nickel-hydroperoxo, forming an organic alcohol and a Ni-O<sup>•</sup> species. The radical oxygen atom then abstracts the H atom of the alcohol. At the same time, the remaining electron from the O-H bond enters the  $\pi$  system of the adjacent C-O bond, and the Ni<sup>III</sup>-C bond homolytically cleaves, forming a C=O bond and reducing the Ni<sup>III</sup> to Ni<sup>II</sup>.



Scheme 1.13: Proposed reaction mechanism for the formation of propenal from oxygenation of NiCl(η<sup>3</sup>-allyl)(iPr).

The role of the *N*-bound substituents on the NHC ligand were then investigated.<sup>50</sup> It was found that sterically bulky substituents, such as *tert*-butyl (<sup>t</sup>Bu) or adamantyl groups, blocked the axial metal sites and prevented the O<sub>2</sub> reaction from occurring (Figure 1.6). This observation was confirmed through the use of asymmetric NHC ligands, where one side was sterically encumbered, and the other side was open. This led to a decrease in the reaction rate compared to smaller substituents, but was still faster when compared to the sterically bulky substituents. It was also found that free rotation about the Ni-NHC bond was observed for non-sterically hindered substituents and these complexes displayed rapid O<sub>2</sub> reactivity. From the observed reactivity, it was proposed that an open axial site is necessary for the oxidation reaction to occur. From this, Sigman proposed that the initial O<sub>2</sub> adduct is a 5-coordinate superoxo complex, although whether this initial intermediate is square pyramidal or trigonal bipyramidal is currently unknown (Figure 1.7).

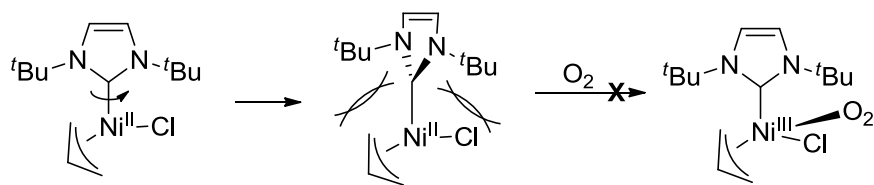


Figure 1.6:  $\text{NiCl}(\eta^3\text{-allyl})(\text{ItBu})$  with the axial sites blocked by the sterically bulky  $t\text{Bu}$  groups, leading to a loss of reactivity.

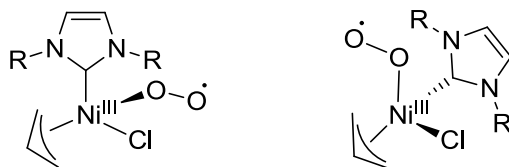


Figure 1.7: Proposed square pyramidal and trigonal bipyramidal  $\text{Ni}^{\text{III}}$ -superoxo intermediates.

## 1.7 $\text{Ni}^{\text{II}}$ -OH Reactivity

From Sigman's proposed reaction pathway, a monomeric  $\text{Ni}^{\text{II}}$ -OH intermediate is proposed, which undergoes dimerization and subsequent decomposition. Reported  $\text{Ni}^{\text{II}}$ -OH species tend to rapidly dimerize and form structures that are more stable than their monomeric counterparts.<sup>41, 50</sup> The monomeric  $\text{Ni}^{\text{II}}$ -OH species are not well studied, and could open new avenues for catalytic allylic oxidation. There are two commonly used approaches to prevent this dimerization process: 1) by increasing the coordination number of the bound ligands, or 2) by providing a hydrogen-bonding group in the secondary coordination sphere, which bonds to the  $\text{Ni}^{\text{II}}$ -OH group and prevents the dimerization.

An example where a ligand with a higher coordination number was used to prevent dimerization of a  $\text{Ni}^{\text{II}}$ -OH comes from Holm *et al.* A tridentate ligand was used to stabilize a monomeric  $\text{Ni}^{\text{II}}$ -OH species, and the reactivity was probed to a variety of reagents, including:  $\text{CO}_2$ ,  $\text{HCO}_2\text{Et}$ ,  $\text{DCM}$ ,  $\text{MeOH}$ ,  $\text{Et}_4\text{NSH}$ , and  $\text{Et}_4\text{NCN}$ .<sup>51</sup> The reactions are shown below in Figure 1.8. When the complex is exposed to  $\text{DCM}$ ,  $\text{MeOH}$ , or  $\text{HCO}_2\text{Et}$ , a ligand exchange reaction occurs. When the complex was exposed to  $\text{Et}_4\text{NSH}$  or  $\text{Et}_4\text{NCN}$ , a metathesis reaction occurs. Lastly, when the complex was exposed to  $\text{CO}_2$ ,

an insertion reaction occurs. Once again, the coordination number of the ligand prevents the dimerization process and allows for characterization and reactivity studies.

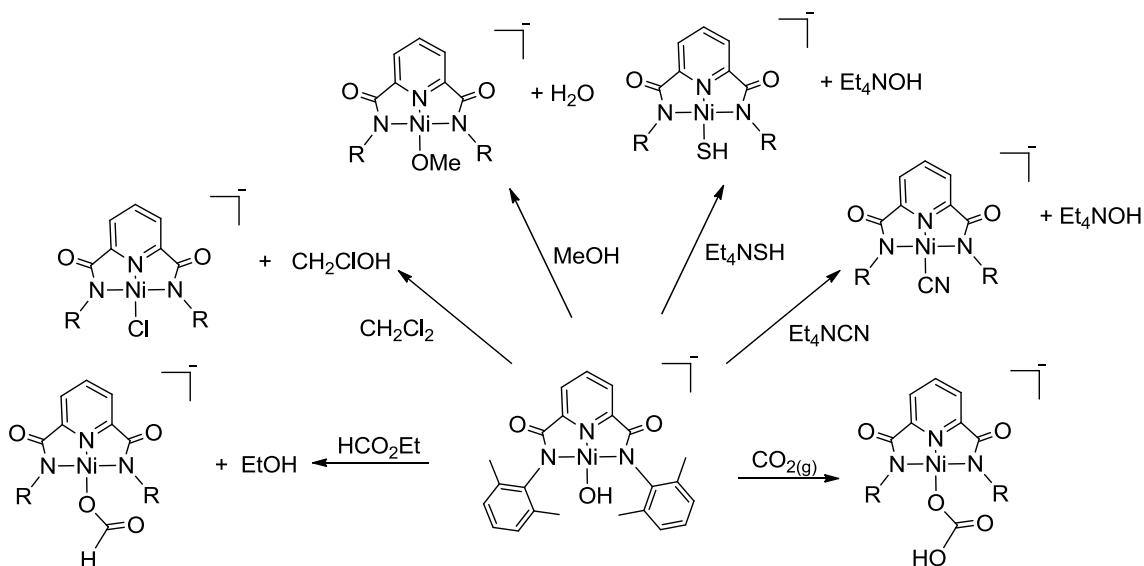


Figure 1.8: Reported reactivity of a  $\text{Ni}^{\text{II}}\text{-OH}$  monomer by Holm *et al.*

The other method to stabilize monomeric  $\text{Ni}^{\text{II}}\text{-OH}$  species is through the use of hydrogen bond donors in the secondary coordination sphere. The secondary coordination sphere describes a section of a ligand that does not bind directly to the metal, but plays a role in its structure or related chemistry. An example of this type of interaction comes from Borovik *et al.* using a tridentate ligand with two hydrogen bond donor groups (Figure 1.9).<sup>52</sup>

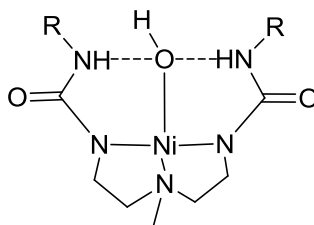
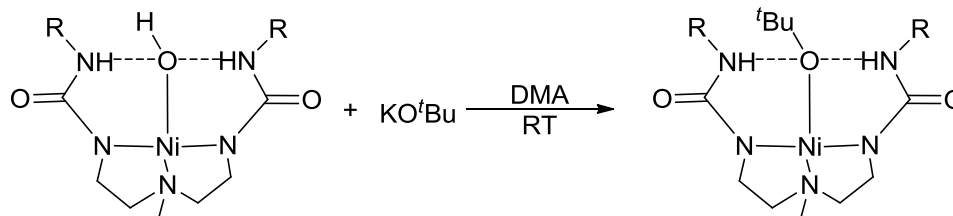


Figure 1.9:  $\text{Ni}^{\text{II}}\text{-OH}$  monomer reported by Borovik *et al.* stabilized by hydrogen bonding interactions from amine N-H moieties in the secondary coordination sphere.

In addition to synthesizing and characterizing the complex, Borovik also investigated the reactivity of the complex with bases. Upon addition of 1 equiv.  $\text{KO}^t\text{Bu}$ , a ligand

substitution reaction occurred, leading to a new Ni-O<sup>t</sup>Bu bond and KOH as a by-product (Scheme 1.14). This reaction shows that the Ni<sup>II</sup>-OH moiety is able to undergo further reactivity such as anion exchange reactions.



Scheme 1.14: Observed reactivity of KO<sup>t</sup>Bu with Borovik *et al.*'s reported Ni<sup>II</sup>-OH species.

Another report comes from Ghosh *et al.*, which detailed the synthesis and catalytic reactivity of a square planar Ni<sup>II</sup>-OH monomer containing two NHC ligands.<sup>53</sup> The monomeric Ni<sup>II</sup>-OH was stabilized by only one hydrogen bond donor, and was sufficiently stable to obtain X-ray quality crystals as well as <sup>1</sup>H NMR and infrared (IR) spectra (Figure 1.10). However, the OH group was sufficiently basic such that it can deprotonate the pendent amide, which promotes catalytic reactivity.

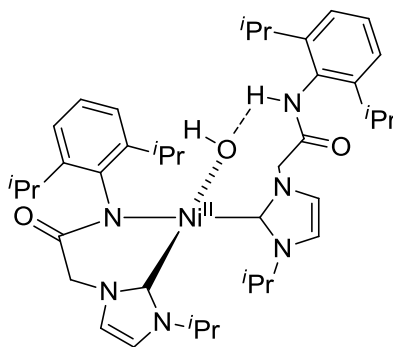


Figure 1.10: The structure of a Ni<sup>II</sup>-OH species stabilized by hydrogen bonding interactions, reported by Ghosh *et al.*

## 1.8 Oxidation of Asymmetric NiCl( $\pi$ -allyl)(NHC) Complexes

A previous member of the Blacquiere group synthesized three new NiCl( $\pi$ -allyl/cinnamyl)(NHC) species with a pendent amine in the secondary coordination sphere (**4**, **5a**, **5b**, Figure 1.11).<sup>54</sup> The goal of including the pendent amine was to provide a

hydrogen bond donor group to help stabilize the hydroxide of the proposed Ni<sup>II</sup>-OH monomer (**7**, Scheme 1.15). The complexes were active towards aerobic oxidation of the allyl and cinnamyl groups, forming the same observed products as previously reported (propenal, or **CA** and **PVK**, respectively). The complexes were proposed to undergo a similar reaction mechanism as Sigman's proposed mechanism, which includes a Ni<sup>II</sup>-OH intermediate (Scheme 1.13). The ideal application of these complexes is for catalysis, and a proposed catalytic cycle is shown below (Scheme 1.15). In step **A** of the catalytic cycle, oxidation of the nickel center forms the proposed Ni<sup>III</sup>-superoxo species (**6**). In step **B**, the products are released and the proposed Ni<sup>II</sup>-OH monomer (**7**) is formed. To close the cycle, a C-H activation event would occur at step **C** between the allylbenzene and hydroxide of **7**. This stabilized Ni<sup>II</sup>-OH species may be sufficiently basic to promote a concerted metalation deprotonation (CMD) with an allylic C-H bond, producing a Ni(allyl) species and water as the byproduct.<sup>55</sup> However, previous work involving CMD has not used metal-bound hydroxo groups as the base.

The complexes **4**, **5a**, and **5b** reacted with O<sub>2</sub>, similar to the complexes previously reported by Sigman *et al.*, producing the expected propenal from **4**, or **CA** and **PVK** from **5a** and **5b**. Product yields of **CA** and **PVK** from **5a** were determined in THF, acetone, MeCN, DMF, and DCM, and found that **CA** and **PVK** are formed in ~1:1 yields, with the highest conversion occurring in MeCN. It was also found that switching the amine substituent from a <sup>t</sup>Bu group to a mesityl group (Mes) had little effect on the conversion and selectivity. Initial catalytic testing was performed in THF or MeCN with allyl benzene as the substrate, but no catalytic turnover observed.

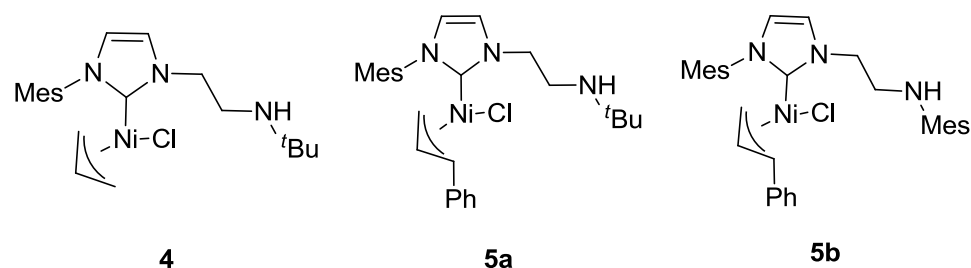
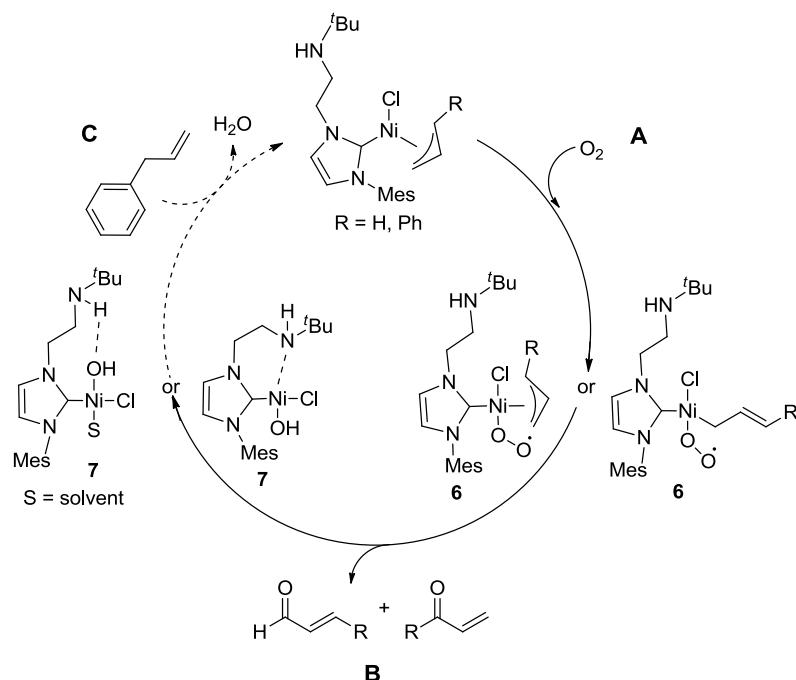


Figure 1.11: The three asymmetric NiCl( $\pi$ -allyl)(NHC) complexes used throughout this work.



Scheme 1.15: Target catalytic reaction for **4**.

## 1.9 Project Goals

### 1.9.1 Determination of Optimal Oxidation and Catalysis Conditions

The first goal of this project was to assess the optimal solvent system for the oxidation of **5a** and **5b**. The second goal of this project was to assess the catalytic activity of **4** at high temperature, low temperature, and with external base present using allylbenzene or cinnamyl pinacolborane as the substrates. Cinnamyl pinacolborane was chosen as a substrate due to the byproduct B-O bond being stronger than the byproduct O-H bond.<sup>56</sup> By altering the solvent, temperature, and additives present, it could be possible to find a set of conditions that favor catalytic turnover.

### 1.9.2 Study of Ni Decomposition Products and Reaction Intermediates Following Oxidation

The third goal of this project was to identify and characterize the reactive intermediates that are proposed within the catalytic cycle. By determining the identity and reactivity of the reactive intermediates, it is possible to determine the mechanism that is occurring upon oxidation. Additionally, this analysis could help determine conditions that could



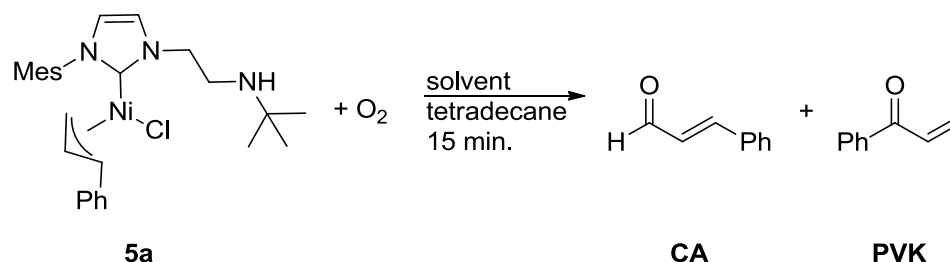
favor catalytic turnover. Lastly, the decomposition products formed after oxidation of **4** were studied. If the decomposition products are known, then steps can be taken to help prevent these decomposition reactions from occurring such as using additives or different reaction temperatures.

## Chapter 2

### 2 Stoichiometric Oxidation of **5a** and **5b** and Catalysis with **4**

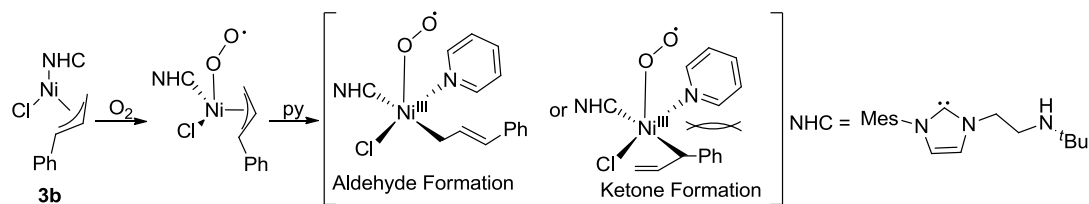
#### 2.1 Stoichiometric Determination of Oxidation Products

Stoichiometric oxidation of **5a** was conducted as an extension of work completed by a previous member of the Blacquiere group (Scheme 2.1). Previous work had been conducted to quantify the amounts of **CA** and **PVK** formed after O<sub>2</sub> addition to 10 mM solutions of species **5a** in THF, DCM, acetone, MeCN, and DMF. Stoichiometric oxidation of **5a** was repeated at 5 mM concentration in a greater variety of solvents for two reasons: 1) to be in a more linear range of the product GC-FID calibration curves and 2) to better compare to the obtained UV-vis spectroscopy data (*vide infra*).



Scheme 2.1: Stoichiometric aerobic oxidation of **5a**.

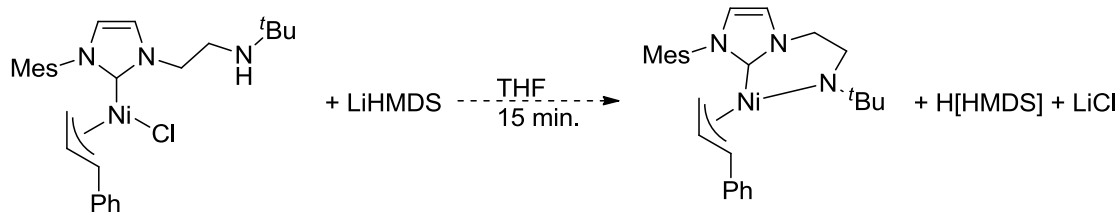
The data obtained at 5 mM was consistent with previous findings at 10 mM, and the only observed products were **CA** and **PVK**.<sup>57</sup> New solvents were also tested, and moderate to good conversion was observed with the products consistently formed in approximately a 1:1 ratio (Table 2.1, Entries 1-9). It was also found that the oxidation of **5a** was unaffected by the presence of H<sub>2</sub>O (Entry 6 vs. Entry 1). When pyridine was used as the solvent, a selectivity change was observed, favoring the formation of the aldehyde product. This was proposed to occur due to pyridine coordination that would favor a linear oxidation product to avoid steric clash (Scheme 2.2).



Scheme 2.2: Proposed Ni<sup>III</sup>-superoxo intermediates after O<sub>2</sub> addition to **5a** in pyridine. Intermediate structures are shown as square pyramidal, but it is possible for them to adopt a trigonal bipyramidal structure.

Upon dissolution of **5a** in dioxane, a bright pink solution was formed, although there was no evidence of **CA** or **PVK** by GC-FID after O<sub>2</sub> addition (Table 2.1, Entry 11). A control reaction was performed where no O<sub>2</sub> was added to **5a** in dioxane, and a similar color change was observed. Once again, there was no evidence of product formation by GC-FID (Table 2.1, Entry 12). This result shows that the complex is unstable in dioxane.

A variety of additives were also studied to see their potential effect on the oxidation step. Oxidation of **5a** in THF in the presence of LiHMDS was first studied, as LiHMDS would be able to abstract the proton from the secondary amine and the chloride ligand (Scheme 2.3). This would make the NHC adopt a  $\kappa^2$ -CN bonding mode, which could affect the yield and selectivity of the products. The oxidation of **5a** in THF, with LiHMDS present at the outset, had lower product yields (ca. 20% lower) than oxidation in THF without base (Table 2.1, Entry 14). It was predicted that LiHMDS could be reacting with the generated products **PVK** and **CA**, thereby lowering the observed yield. To confirm this, a control reaction was performed where LiHMDS was added to a sample after oxidation of **5a** by treatment with O<sub>2</sub> (Table 2.1, Entry 13). Upon the addition of LiHMDS, the yields of **PVK** and **CA** decreased by 8 and 22%, respectively. This indicates that LiHMDS reacts with the products under these conditions and on the timescale for oxidation (Table 2.1, Entry 14).



Scheme 2.3: Proposed Reaction of LiHMDS with **5a**.

$\text{PPh}_3$  was added after the oxidation of **5a** in both THF and MeCN, as  $\text{PPh}_3$  would react with potential peroxides to form the corresponding carbonyl product.<sup>46-47</sup> After the addition of  $\text{PPh}_3$ , both the samples in THF and MeCN showed minimal change in the observed yields, indicating that there are no peroxides formed during the reaction (Table 2.1, Entries 15 and 16).

**Table 2.1 Product Yields for Stoichiometric Oxidation of **5a**<sup>a</sup>**

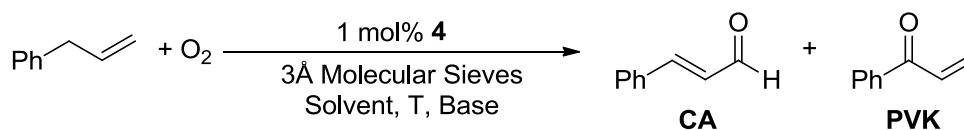
Entry	Solvent	%PVK	%CA	Selectivity (K:A)
1	THF	27	32	0.8:1
2	DCM	35	49	0.66:1
3	Acetone	33	46	0.8:1
4	MeCN	43	46	1:1
5	DMF	35	48	1.1:1
6	THF + H <sub>2</sub> O <sup>b</sup>	26	29	0.9:1
7	MeTHF	33	37	0.9:1
8	Toluene	36	35	1:1
9	DME	32	37	0.9:1
10	Pyridine	11	22	0.5:1

11	Dioxane <sup>c</sup>	0	3	N/A
12	Dioxane <sup>c,d</sup>	0	3	N/A
13 <sup>e</sup>	THF+LiHMDS <sup>f</sup>	5	11	0.5:1
14 <sup>e</sup>	THF	13	46	0.29:1
	THF+LiHMDS <sup>f</sup>	5	24	0.15:1
15	THF	33±20	31±2	1.1:1
	THF + PPh <sub>3</sub> <sup>g</sup>	34±1	38±0	0.9:1
16	MeCN	37±5	23±6	1.6:1
	MeCN + PPh <sub>3</sub> <sup>g</sup>	41±1	30±2	1.4:1

<sup>a</sup> General Conditions: 5 mM **5a**, 5 mM tetradecane, 1 mL solvent, 1 mol% **5a**. Yields quantified using GC-FID. <sup>b</sup>10 equiv. H<sub>2</sub>O relative to **5a** <sup>c</sup>Evidence of decomposition <sup>d</sup>No O<sub>2</sub> added <sup>e</sup>10 mM **5a** <sup>f</sup>11 mM LiHMDS <sup>g</sup>50 mM PPh<sub>3</sub>. Yields shown are an average of 2 runs.

## 2.2 Attempted Catalytic Oxidation of Allylbenzene

Catalytic oxidation of allyl benzene was attempted with 1 mol% of the nickel allyl species **4** as the catalyst (Scheme 2.4). The catalytic conditions were assessed under different solvents, temperatures, and the addition of excess base, with product formation analyzed by GC-FID. **4** was chosen as the catalyst as propenal is the initial product formed, which has high volatility and would exit the GC as part of the solvent peak. To prevent water from interfering with the results, the attempted catalysis was performed in the presence of 3Å molecular sieves.



Scheme 2.4: Attempted catalytic oxidation of allyl benzene.

In MeCN at room temperature, the oxidation products **CA** and **PVK** were not observed (Table 2.2, Entry 1). There are two possible reasons that the reaction did not occur: 1) the Ni<sup>II</sup>-OH intermediate cannot overcome the energy barrier of C-H activation, or 2) the intermediate was highly reactive and follows a non-productive deactivation route. To attempt to overcome a high-energy activation barrier, the reaction was heated, but no oxidation products were observed (Table 2.2, Entry 2). Related studies that involve C-H activation benefit from an added base present during the reaction.<sup>58</sup> *N,N*-diisopropyl ethyl amine was used due to its p*K*<sub>a</sub> (11.44) compared to other potential bases.<sup>59</sup> To this end, a reaction was conducted with excess base, but once again no oxidation products were formed (Table 2.2, Entry 3). To address the potential that deactivation was inhibiting turnover, the reaction flask was cooled to stabilize the reactive intermediates; however, no oxidation products were observed (Table 2.2, Entry 4).

Analogous oxidation reactions were then carried out in pyridine. Pyridine is a good donor ligand that is capable of binding to metals, and was believed to be able to coordinate and stabilize the Ni<sup>II</sup>-OH intermediate that theoretically forms during the catalytic reaction. The catalytic reactions were attempted under similar conditions; with the exception that pyridine was used as the solvent. However, no oxidation products were observed (Table 2.2, Entries 5-8).

The solvents chosen for catalysis do display coordinating ability, and could be forming an adduct with the reactive species that then cannot undergo catalytic turnover. By conducting the catalytic reaction neat, this removes the possibility of forming these adducts, and could allow for the intermediate species to achieve turnover. However, this was not observed.

Lastly, from the <sup>1</sup>H NMR spectroscopy studies conducted (*vide infra*); a unique intermediate was observed at -65 °C, which may contain a Ni<sup>II</sup>-OH moiety. Catalysis was attempted at -50 °C to see if this intermediate was catalytically active. No catalytic turnover was observed. It can be concluded that catalytic oxidation does not occur for the conditions listed in Table 2.2 with **4** as the catalyst.

**Table 2.2: Conditions Screened for the Attempted Catalytic Oxidation<sup>a</sup>**

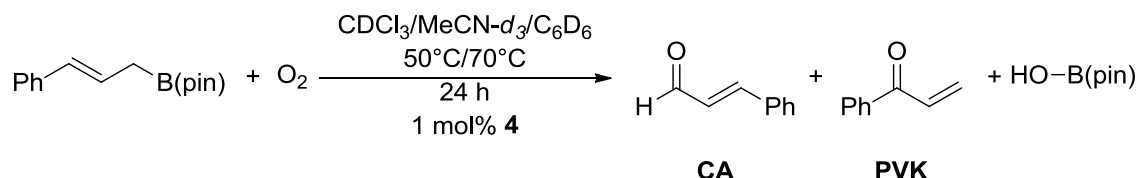
Entry	Solvent	Temperature (°C)	Equiv. base <sup>b</sup>	% CA	% PVK
1	MeCN	22	0	0	0
2	MeCN	70	0	0	0
3	MeCN	22	1.35	0	0
4 <sup>c</sup>	MeCN	-30	0	0	0
5	Pyridine	22	0	0	0
6	Pyridine	100	0	0	0
7	Pyridine	22	1.1	0	0
8 <sup>c</sup>	Pyridine	-30	0	0	0
9	Neat	22	0	0	0
10	DCM	-50	0	0	0

<sup>a</sup> Conditions: 100 mM allyl benzene, 10 mM tetradecane, 1 mol% **4**, and reaction aliquots were analyzed by GC-FID at 0.25, 1, 4, and 6 hours. The 6 h time point data is provided here. <sup>b</sup> *N,N*-diisopropyl ethyl amine. <sup>c</sup> Tetradecane was not used as an internal standard due to its insolubility at low temperatures.

### 2.3 Attempted Catalytic Oxidation with Cinnamyl Pinacolborane as the Substrate

As stated above, there are two possible reasons for the non-catalytic behavior. The first was that the proposed Ni<sup>II</sup>-OH intermediate is unable to overcome the energy barrier at the C-H activation step with the allyl benzene substrate. It was postulated that a more favorable product bond formation would give a Ni<sup>II</sup>-(cinnamyl) intermediate and promote catalytic turnover. To accomplish this, cinnamyl pinacolborane was chosen as a substrate as the byproduct would have a new B-O bond (715 kJmol<sup>-1</sup>) that is more favorable than

an O-H bond ( $431.4 \text{ kJmol}^{-1}$ ), making the reaction thermodynamically favorable.<sup>56</sup> However, the C-B bond is stronger than the allylic C-H bond ( $448 \text{ kJ/mol}$  vs  $361.1 \text{ kJ/mol}$ , respectively).<sup>12, 56</sup> The cinnamyl pinacolborane was synthesized according to literature procedures and catalysis was attempted in a variety of solvents ( $\text{CDCl}_3$ ,  $\text{MeCN-}d_3$ , or  $\text{C}_6\text{D}_6$ ) at both room temperature and elevated temperatures (Scheme 2.5).<sup>60</sup>



Scheme 2.5: Attempted catalytic oxidation with cinnamyl pinacolborane as the substrate.

From the reaction, it was found that the reaction occurring in  $\text{MeCN-}d_3$  showed new resonances in the  $^1\text{H}$  NMR spectrum. Some of the resonances matched to that of authentic cinnamaldehyde, but not all of the peaks were observed. There was also no evidence of **PVK**, but it has known instability on the order of hours at RT. With the increased temperature used in the experiment, it was presumed that any ketone would decompose much faster, and be a poor handle to analyze the reactivity. The catalytic reaction was repeated with an internal standard present, and series of control reactions were conducted, varying the addition of  $\text{O}_2$  or **4**. The control reactions were all conducted at  $70^\circ\text{C}$  in  $\text{MeCN-}d_3$ . The control reactions were analyzed by  $^1\text{H}$  NMR spectroscopy over 48 hours with dimethyl terephthalate as an internal standard to determine conversion (Figure 2.1). First the consumption of cinnamyl pinacolborane was determined and plotted over time. When the substrate was heated in the absence of  $\text{O}_2$  and **4** ( $\blacklozenge$ ), 46% of the substrate remained after 48 hours. This indicates that cinnamyl pinacolborane is unstable to either the temperature or the solvent. When the substrate was exposed to  $\text{O}_2$  ( $\blacksquare$ ), 21% of the substrate was found to remain after 48 hours. While this could indicate catalytic turnover, the consumption of cinnamyl pinacolborane is not drastically affected by the addition of the catalyst ( $\blacktriangle$ ). When cinnamyl pinacolborane is exposed to both  $\text{O}_2$  and **4** ( $\bullet$ ), 8% of the substrate was found after the reaction. If the reaction of cinnamyl pinacolborane with  $\text{O}_2$  were catalytic with **4**, then it would be expected to see faster consumption of the substrate within the first 48 hours. However, the two traces overlap



for the first 24 hours (■ vs. ●, Figure 2.1). In conclusion, complex **4** is non-catalytic with cinnamyl pinacolborane as the substrate.

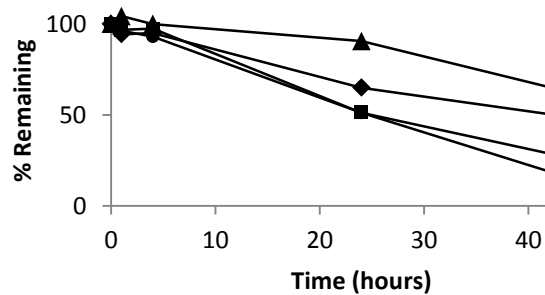


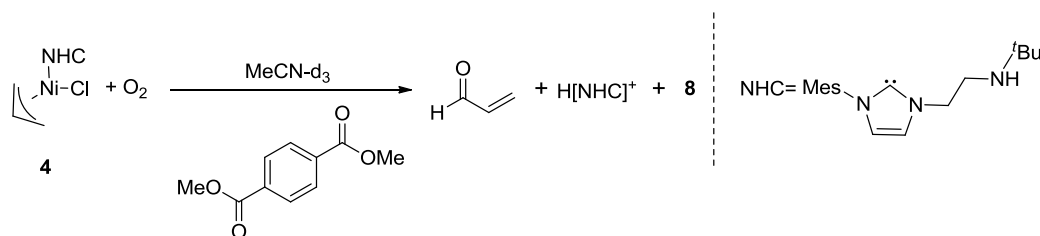
Figure 2.1: Percent of cinnamyl pinacolborane remaining over 48 hours. Traces are: control (◆); O2 (■); 1 mol% **4** (▲); O2, 1 mol% **4** (●).

## Chapter 3

### 3 Analysis of Decomposition Products after Oxidation and Attempted Synthesis of Intermediate Structures

#### 3.1 Determination of Intermediate Species by $^1\text{H}$ NMR Spectroscopy at Room Temperature

To determine the products that form after oxidation of the nickel allyl species **4**, a small-scale oxidation was performed with an internal standard (dimethyl terephthalate) and the reaction was monitored by  $^1\text{H}$  NMR spectroscopy (Scheme 3.1). The allyl species was chosen for ease of analysis, as propenal is the only product formed after  $\text{O}_2$  addition. The reaction was performed three separate times in the presence of dimethyl terephthalate, in  $\text{MeCN-}d_3$ ,  $\text{C}_6\text{D}_6$ , or  $\text{DCM-}d_2$ . The concentrations of the internal standard and **4** were set to 10 mM. After  $\text{O}_2$  addition, the  $\text{DCM-}d_2$  sample produced many solids, making data analysis difficult. The  $\text{MeCN-}d_3$  sample and  $\text{C}_6\text{D}_6$  samples produced similar results. To make the discussion easier, the  $\text{MeCN-}d_3$  will be discussed. For the sample dissolved in  $\text{MeCN-}d_3$ , the expected propenal product was formed (72% yield after four hours), as well as the imidazolium salt  $\text{H}[\text{NHC}]^+$  and another product containing the NHC ligand (**8**) were observed (Figure 3.1).<sup>54</sup> The observed yield of propenal was lower than the combined yields of **CA** and **PVK** from the related stoichiometric oxidation reaction (Table 2.1, Entry 4). The formation of  $\text{H}[\text{NHC}]^+$  was confirmed by matching the chemical shift and integrations of the authentic imidazolium salt and by spiking the reaction sample with the authentic salt, and was formed in a 19% yield based on the starting material. Product **8** was found to form in an overall yield of 16% (Figure 3.2, a)).



Scheme 3.1: Oxidation of **4** in  $\text{MeCN-}d_3$  with dimethyl terephthalate present.

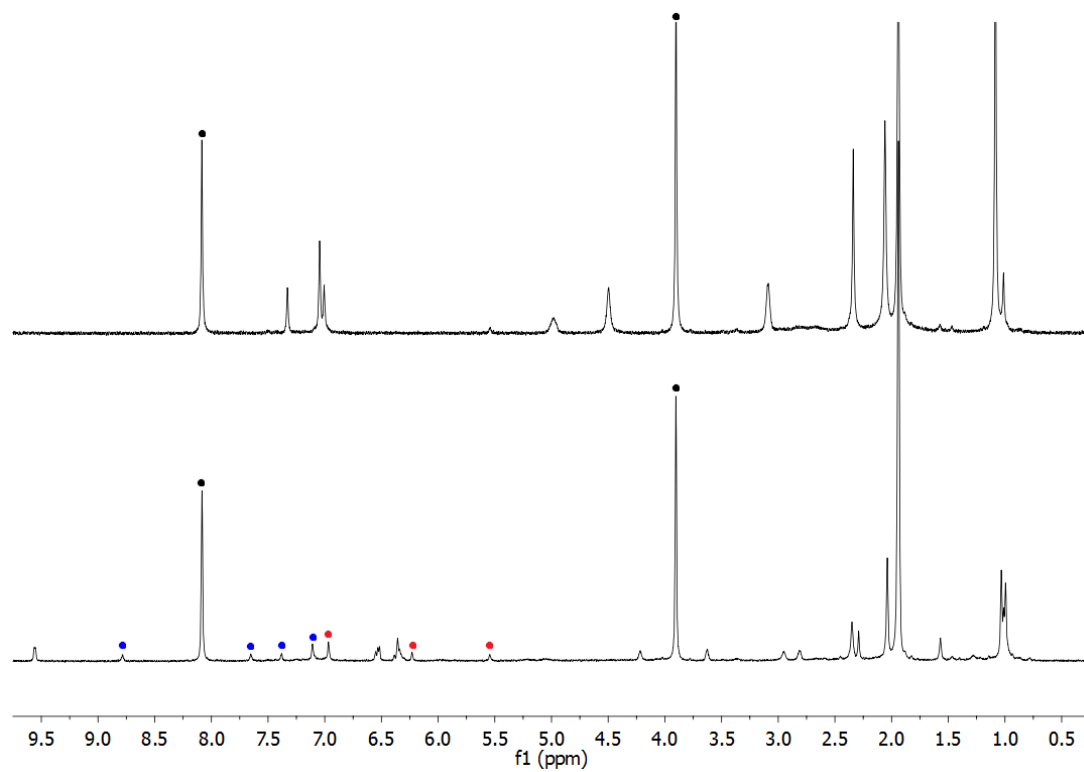


Figure 3.1:  $^1\text{H}$  NMR spectra in as-received  $\text{MeCN-}d_3$  of a) **4** with dimethyl terephthalate, b) **4** with dimethyl terephthalate treated with  $\text{O}_2$ , after 4 hours. Species are labelled as follows:  $\text{H}[\text{NHC}]^+$  (●), an unknown species containing the NHC ligand (●), and dimethyl terephthalate (●).

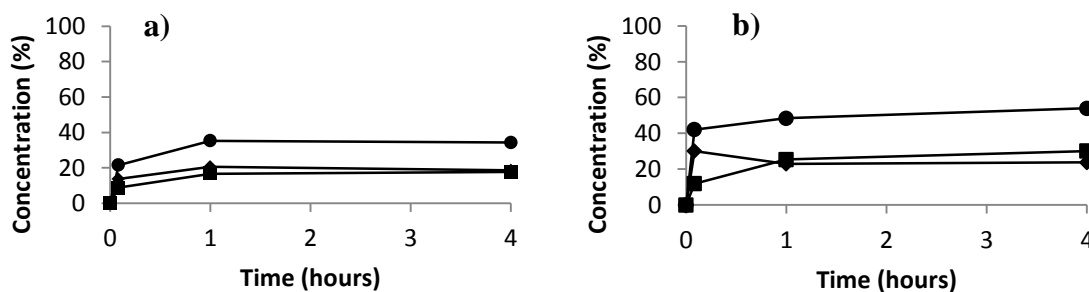


Figure 3.2: a) Product Formation over time in as-received  $\text{MeCN-}d_3$ . b) Product Formation over Time in dry  $\text{MeCN-}d_3$ . Product **8** (◆),  $\text{H}[\text{NHC}]^+$  (■), Combined Yield (●). Conditions: 11.88 mM **4**, 10.30 mM internal standard.

To determine if water played a role in the formation of  $\text{H}[\text{NHC}]^+$ , the reaction was repeated in  $\text{MeCN-}d_3$  that was dried over molecular sieves ( $3\text{\AA}$ ) (Figure 3.2, b)). After exposure to oxygen, **8** is once again the major species initially, but product  $\text{H}[\text{NHC}]^+$

becomes the major product after 1 hour, reaching a final concentration of 30% in dry MeCN- $d_3$ . In as-received MeCN- $d_3$ , H[NHC] $^+$  reaches a final concentration of 19%. This observation shows that water does not play a role in the formation of H[NHC] $^+$ .

Lastly, the majority of the material from the oxidation reaction was unobserved by  $^1\text{H}$  NMR spectroscopy in MeCN- $d_3$ . The three most likely causes for the absence of signal are; 1) the formation of solid products, 2) the formation of NMR silent, paramagnetic species, or 3) the product is highly dynamic, and at room temperature, broadens the related  $^1\text{H}$  NMR signals into the baseline. Solids were observed after 5 minutes upon exposure to  $\text{O}_2$ ; and low temperature NMR spectroscopy pointed to the formation of paramagnetic species being formed (*vide infra*).

After the initial results, the experiment was conducted again, changing the solvent to pyridine- $d_5$  to mimic conditions tested for attempted catalysis. The experiment also compared the effects of as-received pyridine- $d_5$  vs. dry pyridine- $d_5$ . Pyridine is known to coordinate to metal complexes, and as such, the  $^1\text{H}$  NMR spectra were more complex to analyze. In the case of as-received pyridine- $d_5$ , **8** was the major product formed even after 5 minutes, while H[NHC] $^+$  had a delay period before formation. This was especially noticeable in dry pyridine- $d_5$ , where formation of H[NHC] $^+$  was not observed until the 24 hour time point (Figure 3.3 a) and b)).

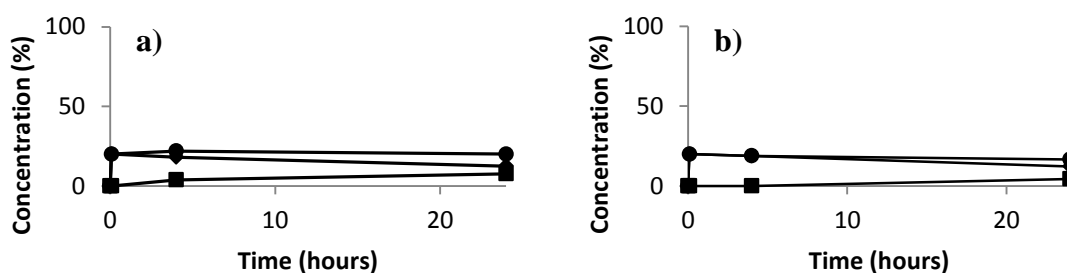


Figure 3.3: a) Oxidation Products over Time in as-received Pyridine- $d_5$ a. b) Oxidation Products over Time in Dry Pyridine- $d_5$ . Product X, ( $\blacklozenge$ ). H[NHC] $^+$ , ( $\blacksquare$ ). Product A + Product B, ( $\bullet$ ). Conditions: 14.3 mM **3a**, 11.33 mM internal standard.

Once again, a large amount of material was unaccounted for by integration in the  $^1\text{H}$  NMR spectra. In both pyridine experiments however, no solids were formed, even after

24 hours in solution. This indicates that the solids observed in MeCN are soluble in pyridine, making pyridine an attractive solvent for potential isolation and determination of other decomposition products *vide infra*. Aside from the formation of paramagnetic species, another possible reason could be lower conversion to the products. Oxidation in pyridine showed a lower overall conversion to **CA** and **PVK** (ca. 30% combined yield) (Table 2.1, Entry 10). Analysis of the  $^1\text{H}$  NMR spectra showed that there is unreacted starting material **4**.

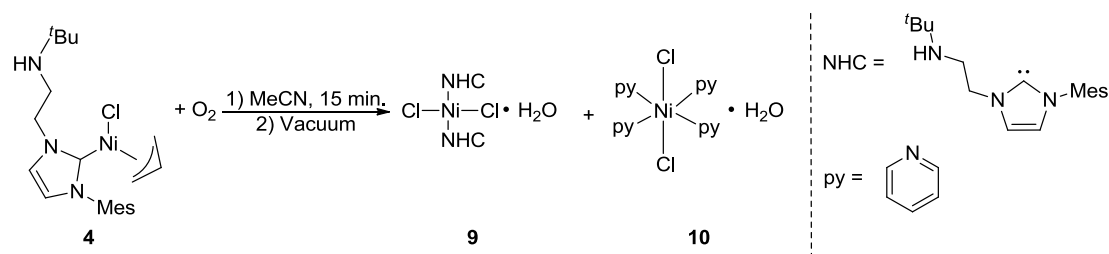
When similar complexes are exposed to the above conditions, the final inorganic product was a  $\text{Ni}^{\text{II}}-\mu\text{OH}$  dimer, with a characteristic upfield  $^1\text{H}$  NMR resonance at  $-7.8$  ppm.<sup>49</sup> Throughout these NMR studies, there has been no evidence of formation of a  $\text{Ni}^{\text{II}}-\mu\text{OH}$  dimer. This could occur for two reasons; 1) the  $\text{Ni}^{\text{II}}-\mu\text{OH}$  dimer was formed, but decomposes rapidly and is not observed, or 2) the  $\text{Ni}^{\text{II}}-\mu\text{OH}$  dimer was formed, but is paramagnetic. Low temperature UV-vis and  $^1\text{H}$  NMR spectroscopy studies have been employed to better probe the intermediate formation of this reaction (*vide infra*).

In conclusion, the imidazolium salt was formed during the oxidation reaction of species **4**. Pyridine has also shown its usefulness by solubilizing solids, which can lead to further identification of the decomposition products. The majority of the material was missing by integration, and may be accounted for by either the formation of solids or the formation of high spin  $\text{Ni}^{\text{II}}$  species. There was no evidence of formation of a  $\text{Ni}^{\text{II}}-\mu\text{OH}$  dimer throughout the NMR studies.

### 3.2 Determination of Inorganic Decomposition Products by X-ray Crystallography

After determining that  $^1\text{H}$  NMR spectroscopy was not able to account for all of the products formed after  $\text{O}_2$  addition, the reaction was scaled up and X-ray crystallography was used to determine the products formed after oxidation. Compound **4** was dissolved in MeCN and was exposed to  $\text{O}_2$ . Once again, the allyl species was used as the propenal is volatile and can be removed with the solvent *in vacuo*. Pyridine was used in the isolation process as it had previously been shown to dissolve the solid species formed after oxidation. The products were separated and crystals suitable for X-ray crystallography

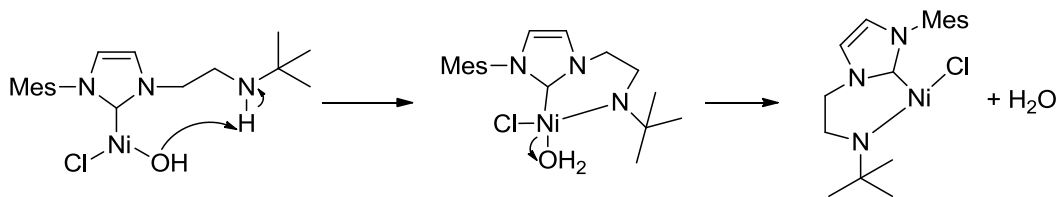
were obtained. The observed products are  $\text{NiCl}_2(\text{NHC})_2 \cdot \text{H}_2\text{O}$  (**9**),<sup>61</sup> and  $\text{NiCl}_2(\text{pyridine})_4 \cdot \text{H}_2\text{O}$  (**10**) (Scheme 3.2).<sup>62</sup> Red crystals of **9** were obtained by slow vapor diffusion of hexanes into toluene, and blue crystals of **10** were obtained by slow vapor diffusion of hexanes into pyridine, respectively. The crystal structures of both **9** and **10** were previously reported and the diffraction patterns matched the reports. Black material unsuitable for X-ray crystallography was also observed.



Scheme 3.2: Observed products after  $\text{O}_2$  addition to **4** in  $\text{MeCN}$ .

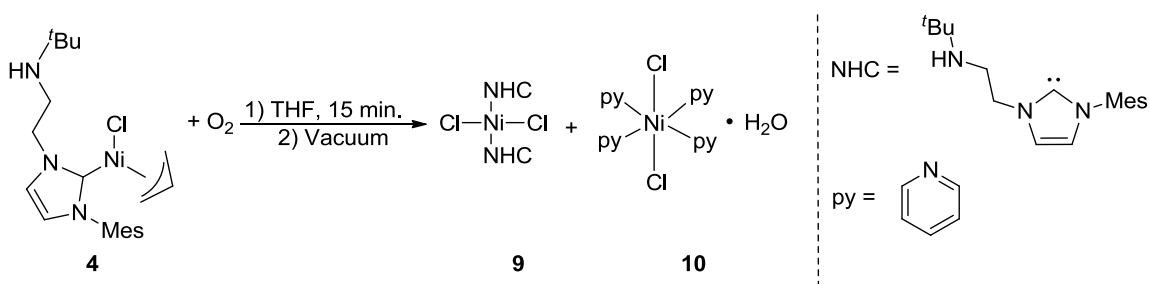
For both products to form, ligand rearrangement must occur, though the mechanism of formation is not yet known. The formation of  $\text{NiCl}_2(\text{NHC})_2$  was observed in Section 3.1 when the oxidation of **4** was carried out in  $\text{C}_6\text{D}_6$ , and was observed in a ~10% yield. Product **10** is postulated to initially be a  $\text{NiCl}_2$  species that is insoluble in  $\text{MeCN}$ . Pyridine is then able to coordinate to the  $\text{NiCl}_2$  and solubilize it, forming the observed species.

The  $\text{Ni}^{\text{II}}\text{-OH}$  dimer that Sigman reported was not observed in these reactions, and the source of the water molecule is unknown as well. A proposed pathway that forms water is the  $\text{Ni}^{\text{II}}\text{-OH}$  dimer is formed, but deprotonates the secondary amine of the NHC to form water (Scheme 3.3). The  $\text{p}K_{\text{a}}$  of the  $\text{Ni}^{\text{II}}\text{-OH}$  intermediate is not known, but the  $\text{p}K_{\text{aMeCN}}$  of related  $\text{R}_2\text{NH}$  ( $\text{R}$  = methyl, ethyl, isobutyl, butyl) was found to be in the range of 17.88-18.75.<sup>63</sup>



Scheme 3.3: Proposed water source.

An analogous reaction in THF results in a color change from brown to dark red after oxidation, with dark red solids found in the flask after removal of the solvent *in vacuo* (Scheme 3.4). Upon workup, purple solids were observed, and were also collected.

Scheme 3.4: Observed products after O<sub>2</sub> addition to **4** in THF.

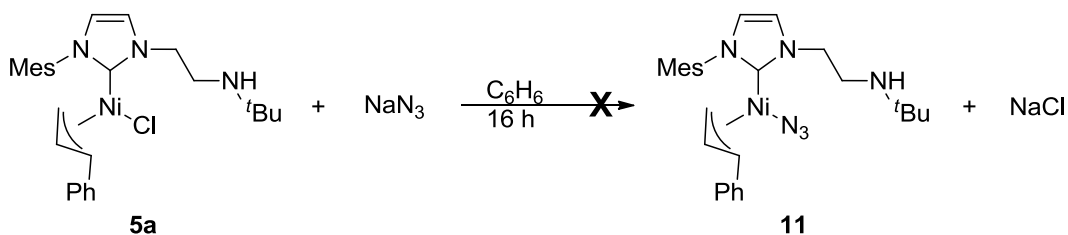
Blood red crystals suitable for X-ray crystallography were grown by slow vapor diffusion of hexanes into THF. These crystals were determined to be NiCl<sub>2</sub>(NHC)<sub>2</sub>, without water in the crystal lattice. This could be a result of a change in reactivity, or a result of the solvents used for crystallization. This reaction was not exposed to pyridine at any point, and purple material was observed to form at the bottom of the crystallization vial. From this experiment, it was found that pyridine is not required to form **9**, indicating that ligand rearrangement is an innate aspect of the reaction.

X-ray quality crystals of the purple material were grown by slow vapor diffusion of hexanes into pyridine at room temperature. After one week, the resulting crystals were found to be a combination of the previously found **9** and **10**. This indicates that isolation of a Ni<sup>II</sup>-μOH dimer is either difficult or the product Ni<sup>II</sup>-μOH dimer is highly unstable and decomposes before crystals can be obtained.

In conclusion, two products from the decomposition reaction were determined by X-ray crystallography;  $\text{NiCl}_2(\text{NHC})_2$  (**9**) and  $\text{Ni-trans-Cl}_2(\text{py})_4$  (**10**). While the mechanisms of formation to these complexes are currently unknown, it is presumed that both of them are formed through ligand displacement reactions of the presumed unstable  $\text{Ni}^{\text{II}}\text{-OH}$  monomers. Future experiments will avoid the use of pyridine to prevent the pyridine from reacting with the products. Water was observed to form in the reaction, presumably through a deprotonation event with the pendent amine of the ligand.

### 3.3 Attempted Synthesis of Azide Substituted **5a** (**11**)

In an attempt to study the proposed superoxo structure, azide ( $\text{N}_3^-$ ) substitutions were investigated, as azides have been shown to have similar steric and electronic properties as superoxo groups.<sup>64-66</sup> The azide substitution reactions were conducted by reacting the cinnamyl nickel species **5a** with  $\text{NaN}_3$  to form **11** and analyzing the crude reaction product by  $^1\text{H}$  NMR spectroscopy, MALDI-MS, and ATR-FTIR spectroscopy. Initial substitution reactions were conducted in benzene (Scheme 3.5), but there was no reaction as shown by the lack of an azide stretch in the ATR-FTIR of the crude solid obtained by solvent evaporation. Also, the MALDI-MS spectrum matched the spectrum for the starting material **5a**. A possible reason that the reaction did not proceed was the noted poor solubility of  $\text{NaN}_3$  in benzene.

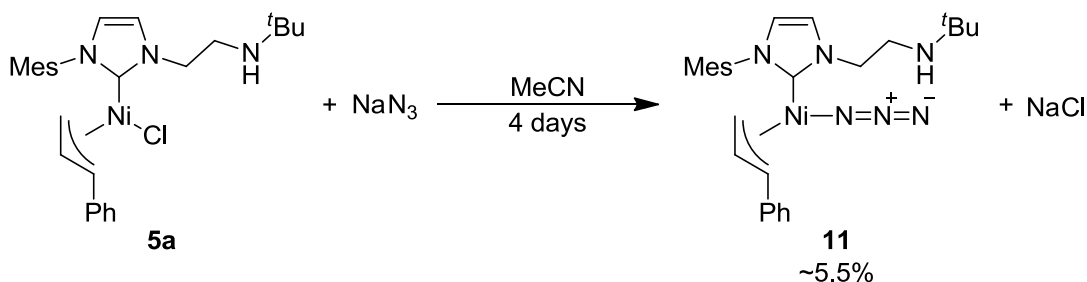


Scheme 3.5: Attempted azide substitution reaction of **5a** (32.8 mM) with  $\text{NaN}_3$  (36.2 mM).

To address the poor solubility, azide installation was instead conducted in MeCN with the hopes that the increased polarity of MeCN would sufficiently dissolve the  $\text{NaN}_3$  reagent (Scheme 3.6). The concentration of the  $\text{NaN}_3$  and **5a** was reduced to aid in the dissolution of the reagents (2.21 mM **5a**, 3.46 mM  $\text{NaN}_3$ ), and while the solubility of  $\text{NaN}_3$  was improved in MeCN, there was only slight insolubility observed. As a result the reaction



time was increased to overcome the reduction in collision probability as a result of the dilution.



Scheme 3.6: Attempted substitution reaction of NaN<sub>3</sub> in MeCN.

After four days, the orange-brown solution changed color to an orange-yellow, and new peaks were observed in the resulting <sup>1</sup>H NMR spectrum (Figure 3.4). However, several signals in the product spectra match to the starting material, suggesting that there was incomplete conversion of starting material to product. By relative integration, there was approximately 5.5% product. This was assuming that the signal at 3.87 ppm (●) accounts for two protons in the product, and the signal at 7.47 ppm (●) accounts for one proton.

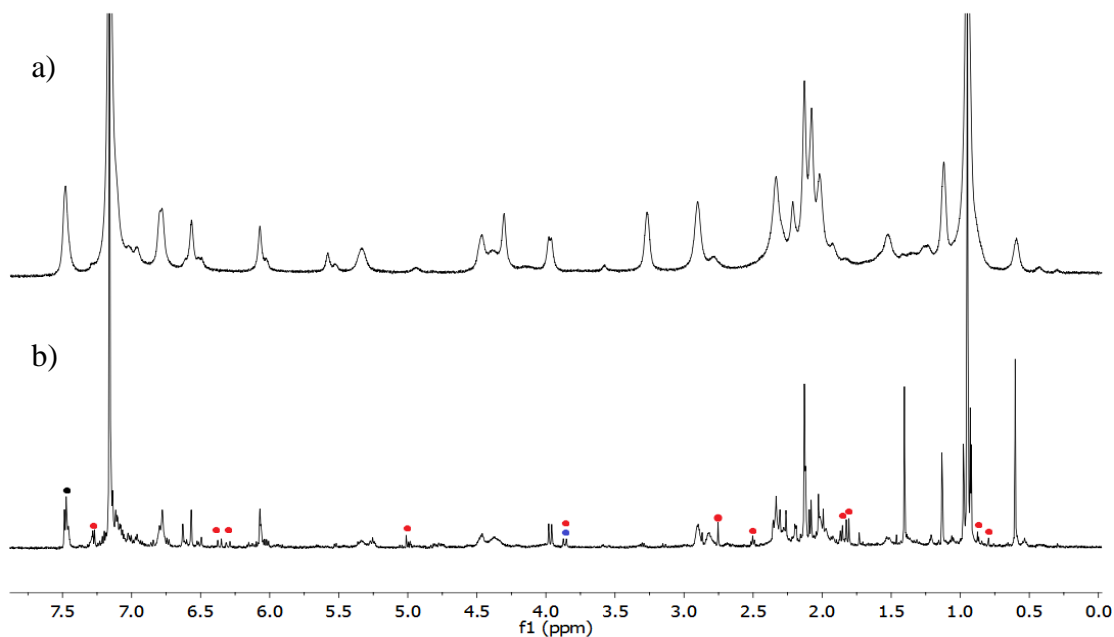


Figure 3.4: NMR stack plot of a) 5a in C<sub>6</sub>D<sub>6</sub> and b) 5a with NaN<sub>3</sub> in MeCN after 4 days, NMR spectrum in C<sub>6</sub>D<sub>6</sub>. Red dots (●) indicate new peaks, the blue (●) and black (●) dots were used in determining overall conversion.

The crude solid that was obtained from the reaction mixture by solvent evaporation was analyzed by ATR-FTIR and compared to the starting material **5a** (Figure 3.5). The sharp peak that appears in the bottom spectrum was found at  $2039\text{ cm}^{-1}$ , which was assigned to the asymmetric stretching unit of the azide and is in the same region as other Ni-N<sub>3</sub> species reported in the literature.<sup>67-70</sup> The FTIR spectrum of authentic NaN<sub>3</sub> has a stretch at  $2100\text{ cm}^{-1}$ .<sup>71</sup> This shift in the azide stretch was consistent with ligation of the azide to the metal center, (Figure 3.5). From the <sup>1</sup>H NMR spectrum, a low-yielding product was observed that likely contains an azide ligand, as seen in the ATR-FTIR spectrum.

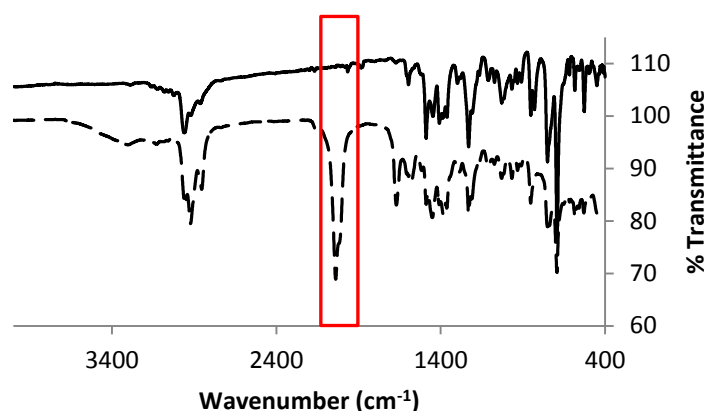


Figure 3.5: Stacked IR spectra of **3b** (solid line) and the azide substituted product **3c** (dashed line).

Lastly, the MALDI-MS was collected of the crude reaction sample, which resulted in a complex mass spectrum. The molecular ion peaks for **11** was not detected, instead, there were signals consistent with:  $\text{H}[\text{NHC}]^+$ ,  $[\text{Ni}(\text{NHC})_2]^+$ , and  $[\mathbf{5a} - \text{cinnamyl}]^+$  (Figure 3.6). The presented spectra are expansions of the full MALDI-MS spectrum and overlaid with their corresponding simulated mass spectrum. The assignment of the peaks was tentative as there was overlap with other unidentified species.

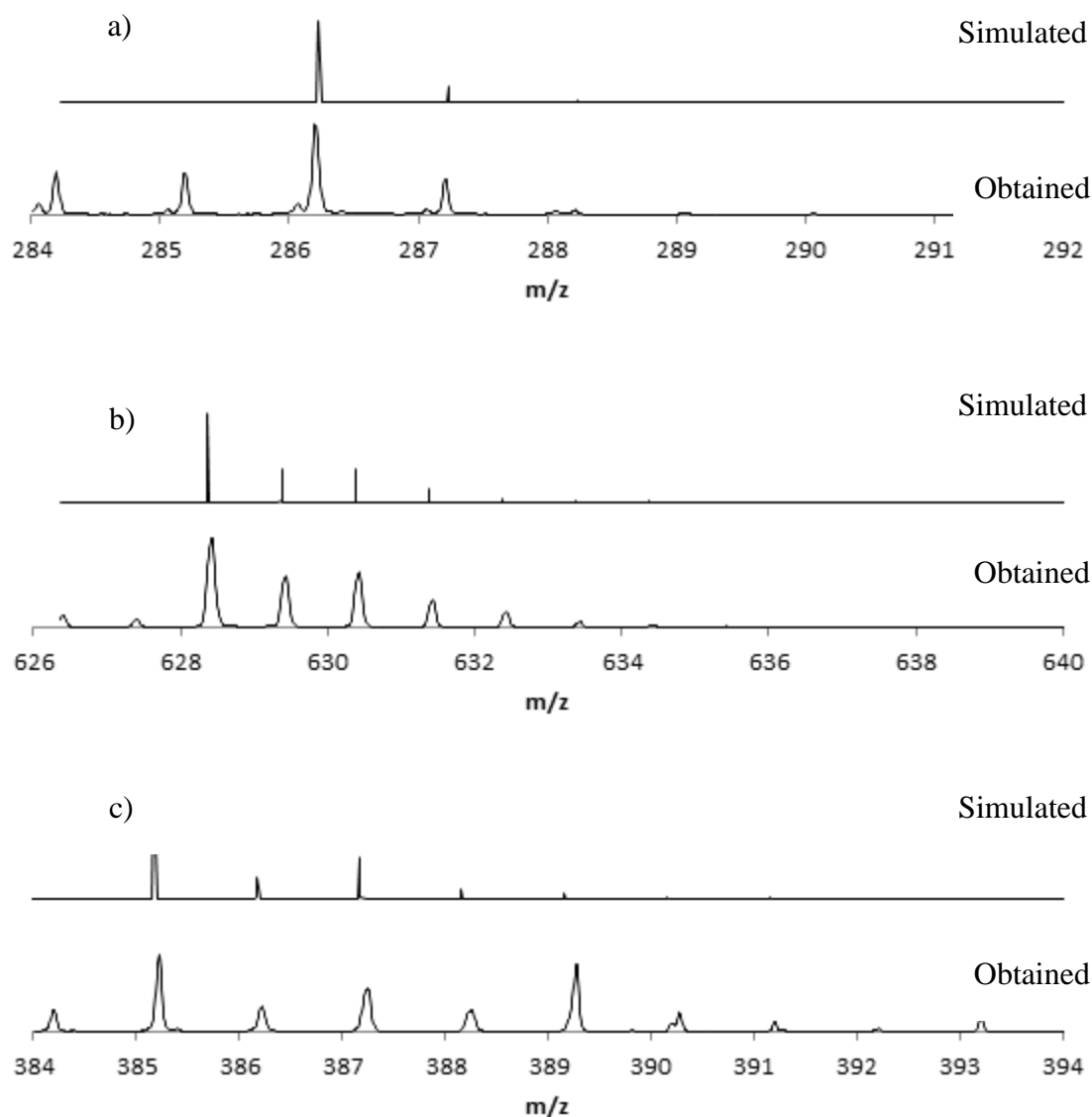


Figure 3.6: Simulated (top) and obtained (bottom) fragment signals from the MALDI mass spectra of **11** with pyrene as the matrix: a)  $\text{H}[\text{NHC}]^+$ , b)  $[\text{Ni}(\text{NHC})_2]^+$ , and c)  $[\mathbf{5a} - \text{cinnamyl}]^+$ .

In an effort to obtain clean material of **11**, a sample was left to crystallize by slow vapor diffusion. Over an extended period of time, orange colored crystals were observed, although these were determined to be the previously reported compound  $\text{NiCl}_2(\text{NHC})_2$  (**9**). This observation was unique, as its related fragmentation pattern was not observed in the MALDI-MS. In conclusion, azide installation was successful as observed from the FT-IR spectrum, but the conversion was not clean and leads to a variety of byproducts as

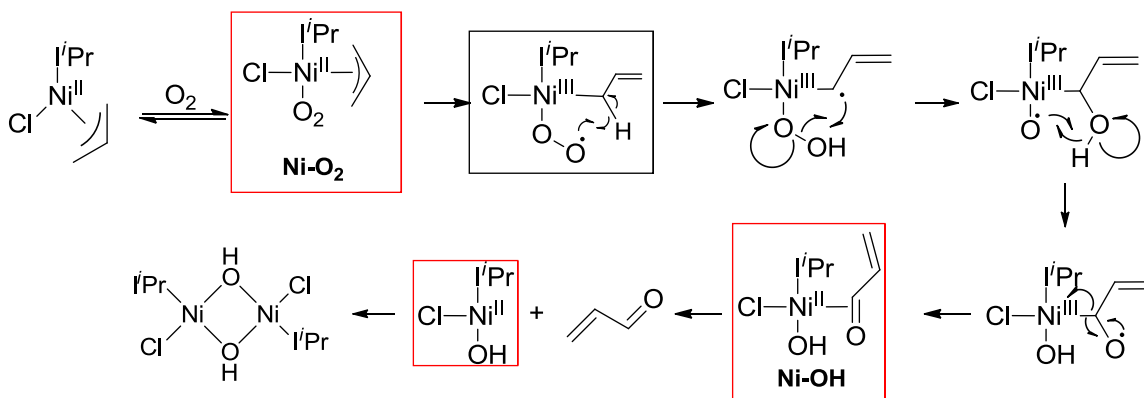
observed in the  $^1\text{H}$  NMR spectroscopy and MALDI-MS spectra, respectively. Due to the difficulty in synthesizing clean material, and with other areas of research with more promising leads, this section of the project was not explored further.

## Chapter 4

### 4 Experimental Determination of Intermediate Species by UV-vis and $^1\text{H}$ NMR Spectroscopy

#### 4.1 Determination of Intermediate Species by UV-vis Spectroscopy

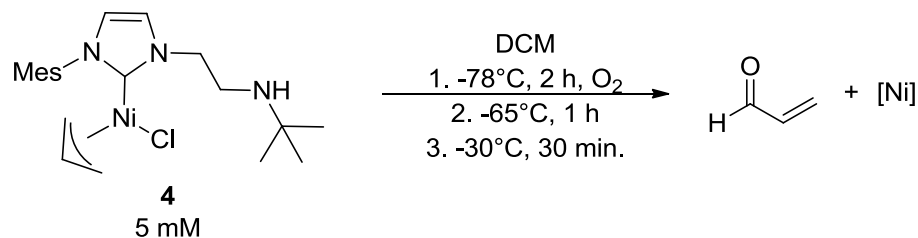
From the above sections, it was found that room temperature studies provided some insight into the reactivity of the nickel complex **4**, but the reaction pathways that are observed are complex and fast, making interpretation difficult. To gain a better handle on the oxidation mechanism, low temperature studies were conducted to attempt to trap out reaction intermediates. Before the results are presented, the mechanism proposed by Sigman *et al.* is shown again.<sup>49</sup> The boxed intermediates are the expected identities of the expected intermediates when conducting these low temperature experiments (Scheme 4.1). The first is **Ni-O<sub>2</sub>**, which was originally proposed by Sigman *et al.* to be a five-coordinate Ni<sup>III</sup>-superoxo structure. The second proposed intermediate structure is the **Ni-OH** species.



Scheme 4.1: Proposed reaction mechanism by Sigman *et al.* Boxed structures indicate high interest intermediates that are sought to be trapped out by low temperature studies.

Low temperature UV-Vis spectroscopy was performed in an effort to determine temperature regimes that would allow for trapping of the reaction intermediates. The

experiments were conducted using a 5 mM solution of **4** in DCM and UV-vis spectra were obtained at various temperatures and times after O<sub>2</sub> addition (Scheme 4.2).



Scheme 4.2: General reaction scheme for low temperature UV-Vis experiments.

Upon initial cooling of **4**, a change in the UV-Vis spectrum was observed at  $-65^\circ\text{C}$  compared to room temperature. This change in the UV-Vis spectrum was found to be reversible since the original room temperature UV-vis spectrum was observed on warming the sample back to  $20^\circ\text{C}$  (Figure 4.2). From the low temperature  $^1\text{H}$  NMR spectrum of **4**, the complex is fluxional on the  $^1\text{H}$  NMR timescale until the static regime was reached at  $-70^\circ\text{C}$ .<sup>54</sup> At this low temperature, the allyl ligand was confirmed to be in the  $\eta^3$  binding mode. From the crystallographic results, the NHC ligand was found to be in a  $\kappa^1\text{-C}$  NHC binding mode. It is believed that at room temperature, the complex undergoes isomerization between a  $\kappa^1\text{-C}$  NHC binding mode and a  $\kappa^2\text{-CN}$  NHC binding mode (Figure 4.1). Upon cooling, it was found that the complex adopts the  $\eta^3\text{-allyl } \kappa^1\text{-C}$  NHC binding mode readily and was believed to be the species observed here.

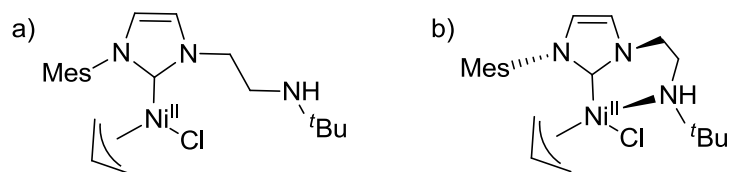


Figure 4.1: Structure of **4** with a)  $\kappa^1\text{-C}$  NHC binding mode, and b)  $\kappa^2\text{-CN}$  NHC binding mode.

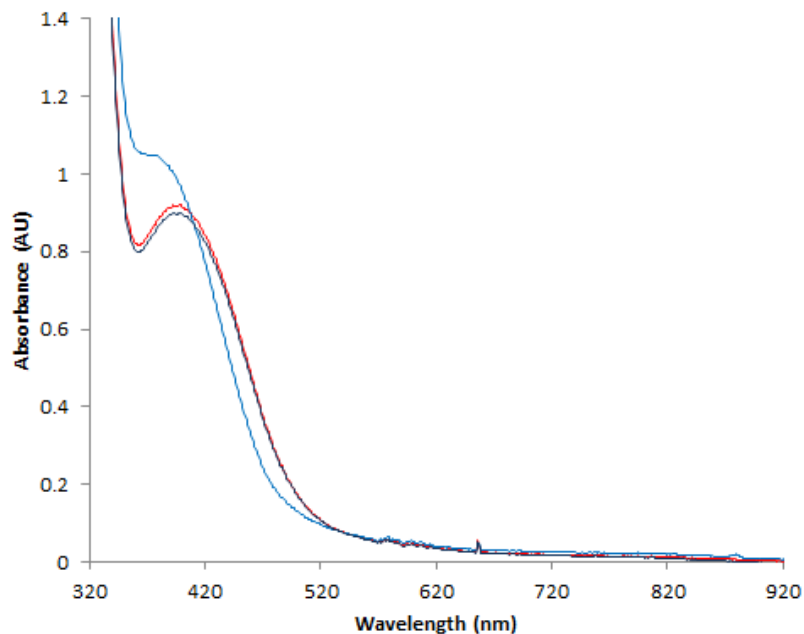


Figure 4.2: UV-Vis spectra of 5 mM **4** at: 20 °C (red); -65 °C (blue); and at 20 °C after having been cooled to -65 °C (purple).

After O<sub>2</sub> addition to **4** at -78 °C, a reaction was observed by UV-vis spectroscopy and was finished by two hours. During the reaction, the UV-vis spectrum showed a decrease in the absorbance at 430 nm, with a related growth at 750 nm (Figure 4.3). An isosbestic point was observed at 454 nm, which is consistent with conversion to a single product. The species observed at this temperature was labelled **Int. 1**. Currently, **Int. 1** is known to be stable for at least 15 minutes by <sup>1</sup>H NMR spectroscopy, but its total lifetime is currently unknown.

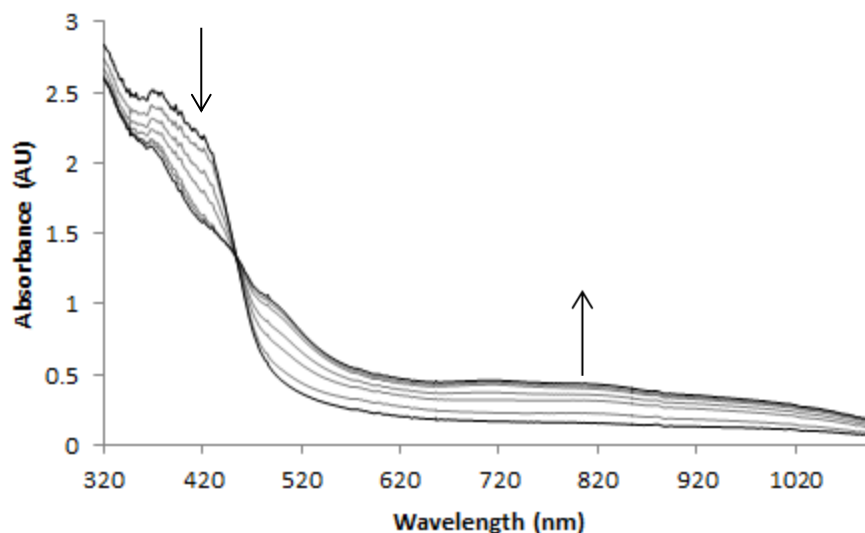


Figure 4.3: Kinetics trace of **4** flushed with O<sub>2</sub> for 10 seconds over 2 hours. The reaction time between each trace is 20 minutes.

Upon warming **Int. 1** to  $-65$  °C, a reaction was observed by UV-vis spectroscopy over the course of an hour, and was found to be complete at this time. A decrease in absorbance at 395 nm and an increase at 825 nm was observed, with an isosbestic point observed at 725 nm (Figure 4.4). The species observed by UV-vis spectroscopy at this temperature was labelled **Int. 2**. The stability of **Int. 2** has not yet been probed by UV-vis spectroscopy, but was stable for up to two hours based on <sup>1</sup>H NMR spectroscopy.



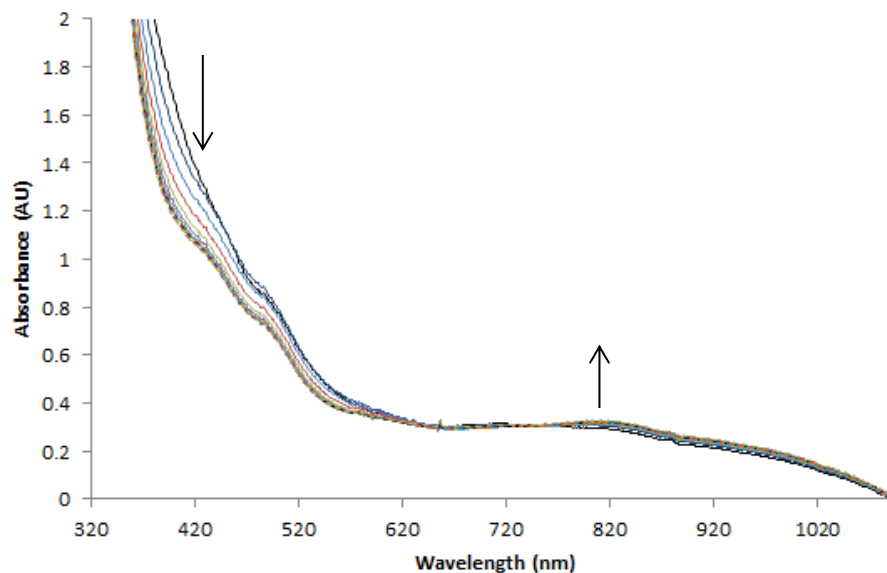


Figure 4.4: UV-Vis spectra of **Int. 1** warmed to  $-65\text{ }^{\circ}\text{C}$  and monitored for one hour. The reaction time between each trace is 5 minutes.

Lastly, the sample was warmed to  $-30\text{ }^{\circ}\text{C}$ , and the reaction was complete by 30 minutes. The UV-vis spectra changes on warming above  $-60\text{ }^{\circ}\text{C}$ , but the changes are slow until  $-30\text{ }^{\circ}\text{C}$ , after which the UV-vis spectrum changes rapidly. There was a loss of the absorbance around 430 nm, and no corresponding band increases are observed (Figure 4.5). There was no observed isosbestic point, which suggests that **Int. 2** likely converts to more than one species as the temperature was raised. There were no further spectral changes observed above  $-30\text{ }^{\circ}\text{C}$ , even with continued warming up to  $20\text{ }^{\circ}\text{C}$ . As there was no further reactivity observed, it was presumed that the products formed at  $-30\text{ }^{\circ}\text{C}$  are decomposition species that were studied previously by room temperature  $^1\text{H}$  NMR spectroscopy and X-ray crystallography studies (Chapter 3).

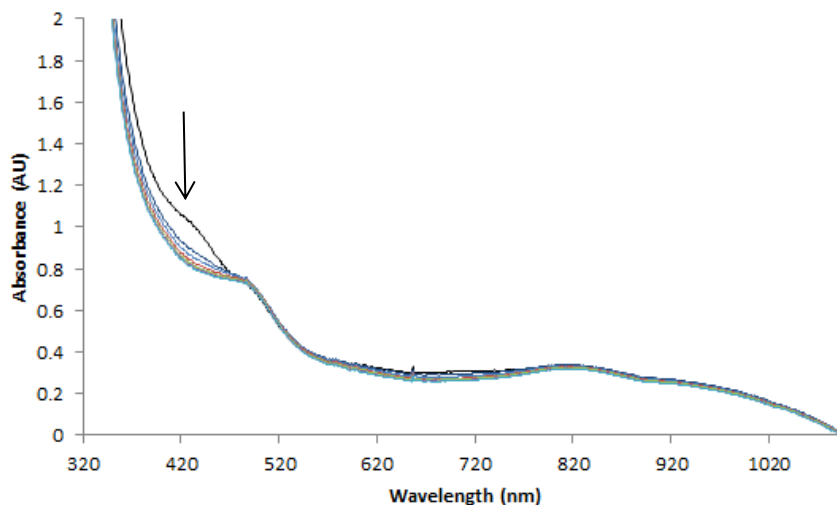
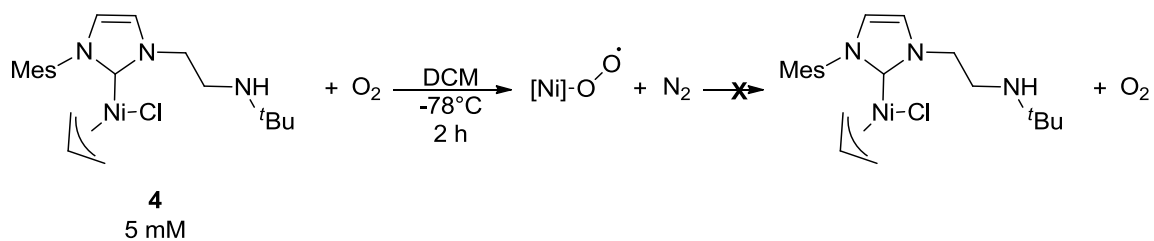


Figure 4.5: UV-Vis spectra of **Int. 2** warmed to  $-30\text{ }^{\circ}\text{C}$  for 30 minutes. The reaction time between each trace is 5 minutes.

The UV-vis spectroscopy experiments reveal that on aerobic oxidation of **4**, two intermediate species are successfully trapped at low temperature: **Int. 1** was trapped at  $-78\text{ }^{\circ}\text{C}$  and **Int. 2** was trapped at  $-65\text{ }^{\circ}\text{C}$ .

## 4.2 Reversibility of Trapped Intermediates

To investigate the reversibility of formation of **Int. 1**, the solution was sparged with dry  $\text{N}_2$  after the oxidation of **4** had successfully occurred (Scheme 4.3). The UV-Vis spectra of the  $\text{N}_2$  sparged solution did change slightly from the spectrum for **Int. 1**. However, the final spectrum did not match that of the starting Ni complex **4** at this temperature (Figure 4.6). Instead, the spectrum resembled that of **Int. 2** (Figure 4.7). **Int. 1** has not yet been left at  $-78\text{ }^{\circ}\text{C}$  for an extended time period, and it could be possible that **Int. 1** is only stable on the order of hours. There are three possible explanations for the lack of reversibility in the formation of **Int. 1**; 1) **Int. 1** is not a superoxo species as initially expected; 2) if **Int. 1** is superoxo species, the Ni-O<sub>2</sub> bond strength is greater than anticipated, or 3) **Int. 1** is a superoxo species, but reacts to form **Int. 2** before the sparging experiment could be completed.



Scheme 4.3: Formation of **Int. 1** and N<sub>2</sub> sparging to test for reversibility of O<sub>2</sub> binding, expected reactivity if **Int. 1** was a Ni<sup>III</sup>-superoxo species ([Ni]-O-O•).

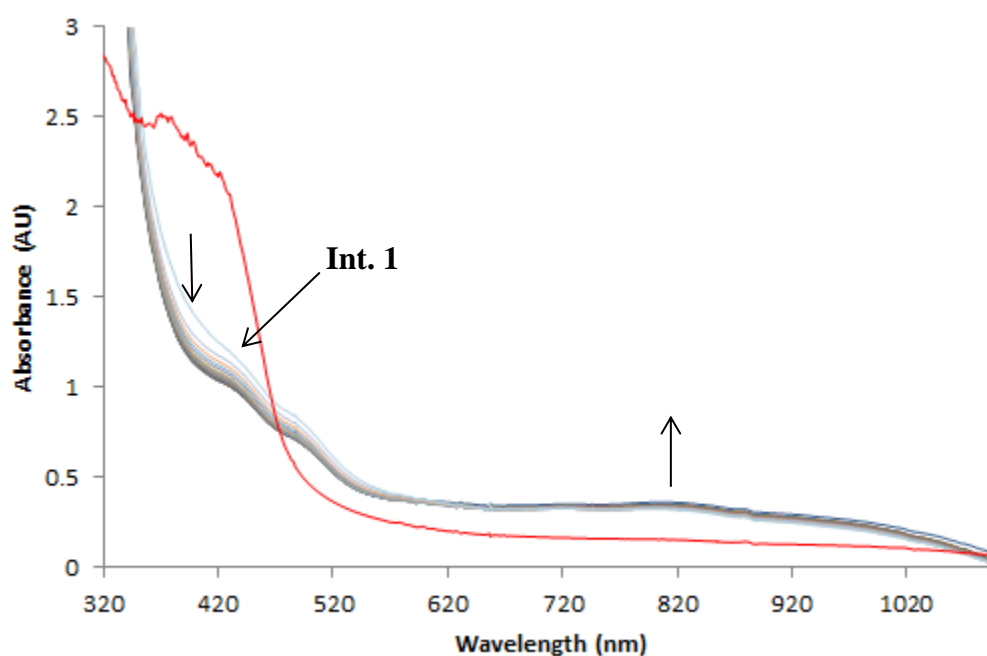


Figure 4.6: UV-Vis spectra of 5 mM **4** at  $-78^\circ\text{C}$  (red), 3 hours after O<sub>2</sub> addition at  $-78^\circ\text{C}$  (light blue), and after being sparged with N<sub>2</sub>. Traces were obtained every 5 minutes after N<sub>2</sub> addition for 100 minutes, and a final trace was obtained at 160 minutes.

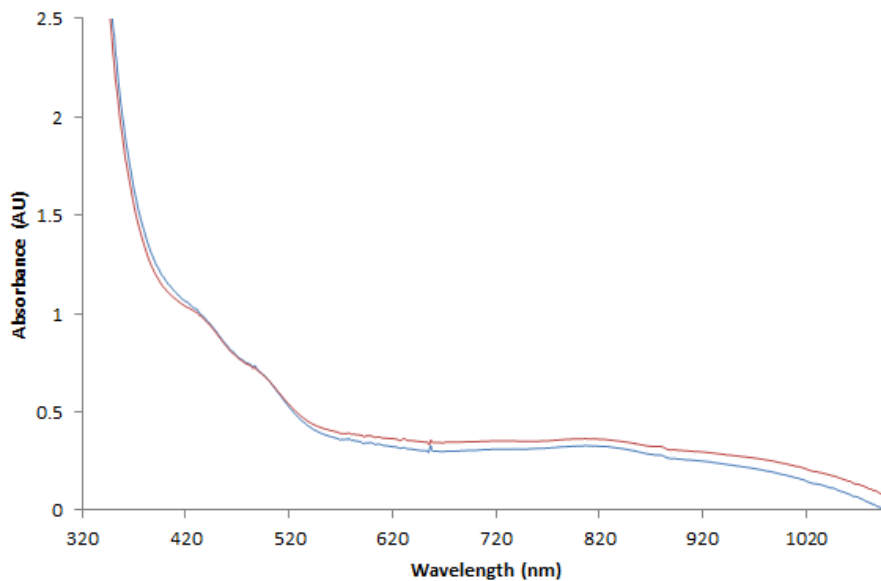
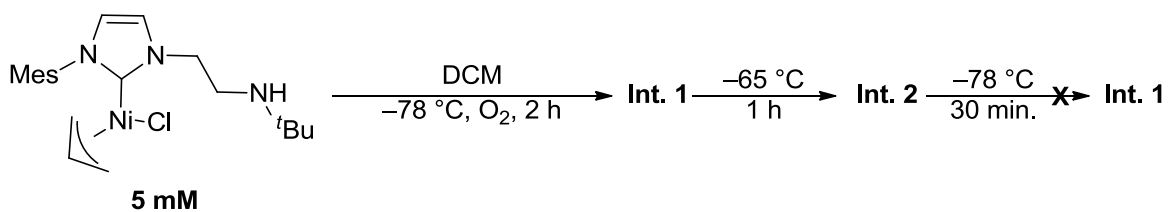


Figure 4.7: Comparison of 5 mM **4** exposed to O<sub>2</sub> at -78 °C for two hours, then: sparged with N<sub>2</sub> for 30 seconds, left for 160 minutes (blue); **Int. 2** (red).

To assess the reversibility of formation of **Int. 2** from **Int. 1**, **Int. 2** was generated at -65 °C and then cooled back to -78 °C, and the reaction was monitored by UV-vis spectroscopy (Scheme 4.4). After the sample was cooled to -78 °C, there was no change observed by UV-vis spectroscopy. The observed spectrum closely resembles that of **Int. 2** (Figure 4.8), indicating that the formation of **Int. 2** was not thermally reversible from **Int. 1**.



Scheme 4.4: Proposed reaction to assess the thermal reversibility of **Int. 2** from **Int. 1**.

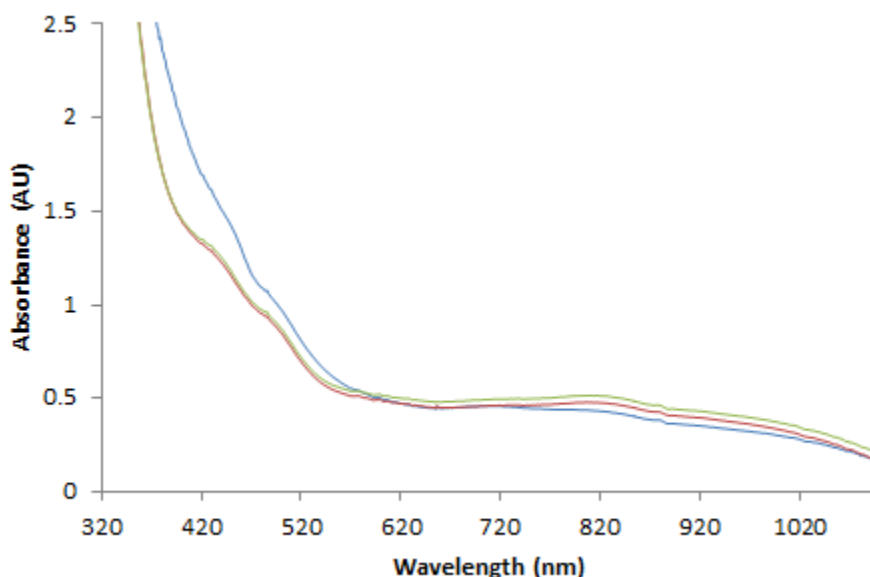
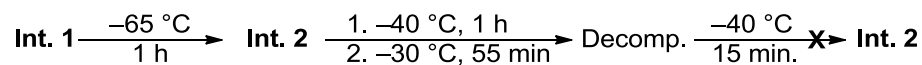


Figure 4.8: UV-Vis spectra of **4** exposed to  $O_2$  at  $-78\text{ }^\circ\text{C}$  for two hours to give **Int. 1** (blue), the sample was warmed to  $-65\text{ }^\circ\text{C}$  for one hour to give **Int. 2** (red), and cooled back to  $-78\text{ }^\circ\text{C}$  for 30 minutes (green).

To assess the reversibility of formation of decomposition species from **Int. 2**, **Int. 2** was generated at  $-65\text{ }^\circ\text{C}$  and warmed to  $-40\text{ }^\circ\text{C}$  for one hour, warmed to  $-30\text{ }^\circ\text{C}$  for 55 minutes, and cooled to  $-40\text{ }^\circ\text{C}$  for 15 minutes (Scheme 4.5). The reaction was monitored by UV-vis spectroscopy (Figure 4.9). After initially warming to  $-40\text{ }^\circ\text{C}$ , a change was observed in the UV-vis spectrum and did not overlap with **Int. 2**, but also did not overlap with the decomposition UV-vis spectrum, albeit the spectra are similar. This observation may indicate that the decomposition species are formed at either earlier timepoints or at lower temperatures. The formation of the decomposition species at  $-30\text{ }^\circ\text{C}$  was confirmed after 55 minutes, and cooled back to  $-40\text{ }^\circ\text{C}$ . However, the UV-vis spectrum did not

match **Int. 2** upon cooling, and remained the same. This observation indicates that the formation of decomposition species from **Int. 2** is not thermally reversible.



Scheme 4.5: Proposed reactivity to assess the thermal reversibility of the decomposition products to **Int. 2**.

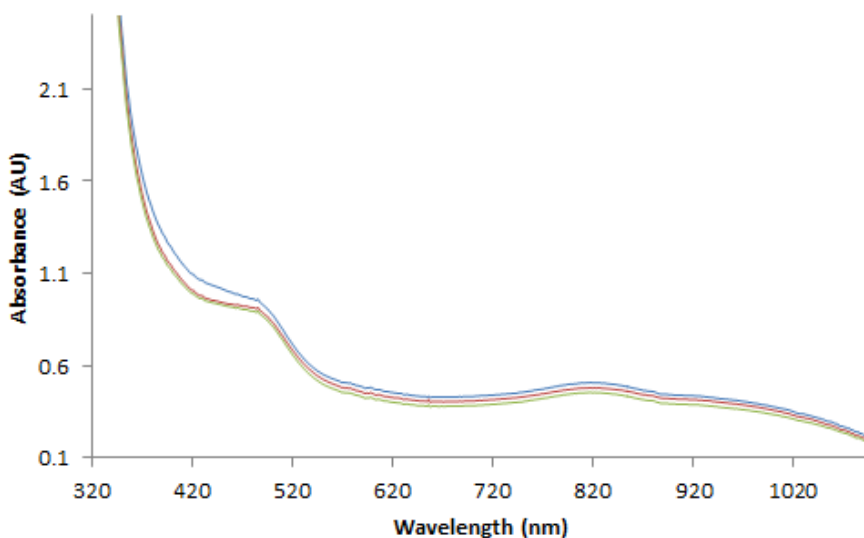
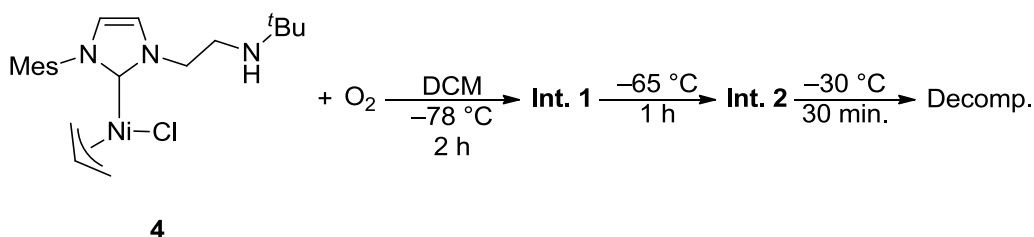


Figure 4.9: UV-Vis spectra of **Int. 2**, warmed to  $-40 \text{ }^\circ\text{C}$  and held for one hour (blue), the sample was warmed to  $-30 \text{ }^\circ\text{C}$  for 55 minutes to give the decomposition products (red), and cooled back to  $-40 \text{ }^\circ\text{C}$  for 15 minutes (green).

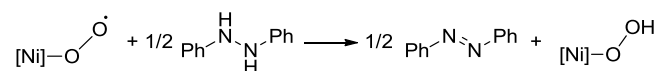
In conclusion, it has been determined that the formation of **Int. 1** from aerobic oxidation of **4** was not reversible, as determined by sparging with  $\text{N}_2$ . This also indicates that **Int. 1** may not be a  $\text{Ni}^{\text{III}}$ -superoxo, as other  $\text{Ni-O}_2$  adducts have shown reversibility upon sparging with inert gas.<sup>46, 48</sup> It has also been determined that the formation of **Int. 2** and the decomposition products are not thermally reversible, indicating that a chemical change has occurred. The reaction scheme is shown below (Scheme 4.6).



Scheme 4.6: Reaction pathway that is observed upon aerobic oxidation of **4**.

### 4.3 Reactivity of Oxidation Intermediates

To assess if **Int. 1** was a superoxo species, **Int. 1** was reacted with a hydrogen atom transfer (HAT) reagent and the reaction was monitored by UV-vis spectroscopy. If **Int. 1** contains a superoxo moiety and follows the reaction mechanism proposed by Sigman *et al.*, then it should readily abstract H<sup>•</sup> atoms from bonds that are weaker than the allyl C(sp<sup>3</sup>)-H bond (361.1 kJmol<sup>-1</sup>).<sup>12</sup> 1,2-Diphenyl hydrazine (DPH) was chosen as the HAT reagent as the compound only absorbs in the UV regions, while the expected azobenzene product has a strong absorbance band at 430 nm. DPH also has a low bond dissociation free energy at 280.7 kJmol<sup>-1</sup>, which is significantly weaker than the C(sp<sup>3</sup>)-H bond of an allyl.<sup>72</sup> The overall proposed reaction scheme is shown below (Scheme 4.7).



Scheme 4.7: Expected hydrogen atom transfer from DPH to a Ni<sup>III</sup>-superoxo ([Ni]-O-O<sup>•</sup>) species to give azobenzene and a Ni-hydroperoxo.

After confirming the formation of **Int. 1** by UV-Vis spectroscopy, DPH was titrated into the solution in 0.2 molar H<sup>•</sup> equivalents, reaching 1.2 equivalents of H<sup>•</sup> at the end of the experiment. After the addition of up to 1 equivalents of H<sup>•</sup>, no significant spectral changes were observed that would support formation of azobenzene (Figure 4.10). After 1 molar equivalent of H<sup>•</sup> was added, a slight increase at 430 nm was observed consistent with the azobenzene product. This change in the spectrum was minor and it was thus attributed to the ~5% contamination of azobenzene in the DPH reagent. This observation indicates either 1) **Int. 1** was a superoxo, but follows a different mechanism than the one proposed by Sigman that does not involve HAT with the superoxo, or 2) it was not a superoxo, and

instead is an intermediate further along the reaction pathway. Due to the observed irreversible formation of **Int. 1** and no observed HAT reactivity, the latter case is more likely. Additionally, there is literature precedence for metal-superoxo systems successfully performing H<sup>•</sup> abstractions.<sup>23,73</sup>

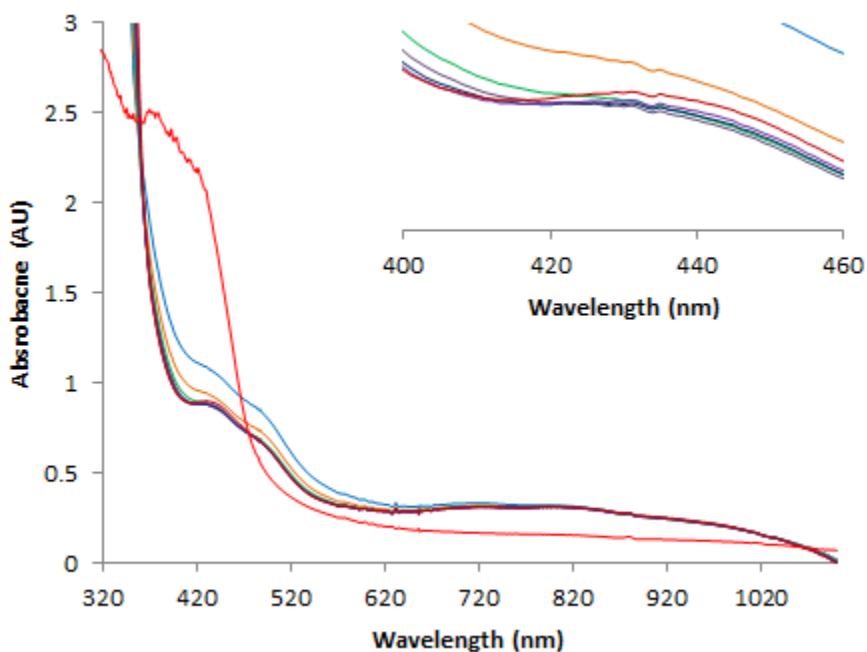
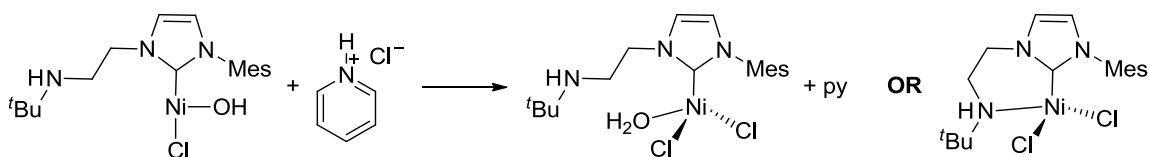


Figure 4.10: UV-Vis spectra of: 5mM **4** at  $-78\text{ }^{\circ}\text{C}$  (red), **Int. 1** (blue), and **Int. 1** after 0.2 equivalent additions of DPH (orange, green, dark blue, purple, dark red, respectively). The reaction time between each trace is 10 minutes. The inset shows an expansion of the region between 400 nm and 460 nm.

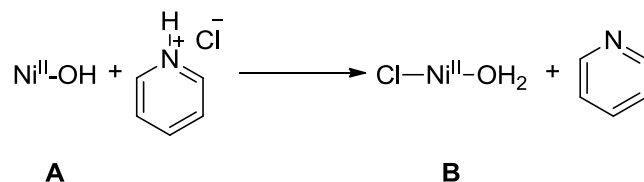
Next, **Int. 2** was reacted with an acid and the reaction was monitored by UV-vis spectroscopy. If **Int. 2** contained a hydroxo ligand, which was a proposed intermediate in the Sigman mechanism, then an acid of sufficient strength would react with the hydroxo ligand to form water. The conjugate base would then either install itself on the nickel center, or form an ion pair with the resulting complex. Pyridinium chloride ( $\text{py}\cdot\text{HCl}$ ) was chosen as the acid ( $\text{p}K_{\text{aMeCN}} = 12.3$ ), as it was miscible in DCM, and also avoids the addition of water into the reaction.<sup>63</sup> Lastly, the pyridine byproduct could form an adduct and stabilize the resulting Ni species (Scheme 4.8)





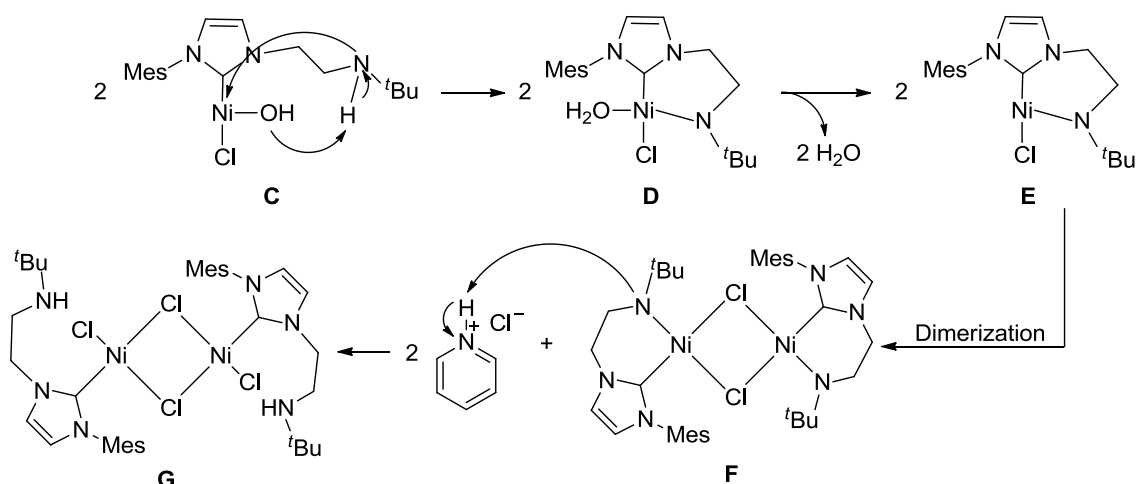
Scheme 4.8: Proposed reaction between a Ni<sup>II</sup>-OH monomer and py•HCl.

**Int. 2** was formed following an analogous procedure as above, and its formation was confirmed by UV-vis spectroscopy. Once it was confirmed, 0.2 molar equivalents of py•HCl were titrated into the solution, reaching a final amount of 1.2 molar equivalents. Upon addition of up to 0.6 molar equivalents, an isosbestic point was observed at 482 nm, with a decrease in the absorption band at 435 nm and a related growth in the band at 495 nm and 820 nm (Figure 4.11). The data suggested that **Int. 2** contains a Ni<sup>II</sup>-OH moiety, and that it was sufficiently basic to react with py•HCl (Scheme 4.9). Whether this reactivity was occurring from a monomeric or a dimeric Ni<sup>II</sup>-OH species is currently unknown. As the reaction between **A** and py•HCl was spontaneous, then **B** must have a  $pK_{aMeCN}$  that is at least 13.



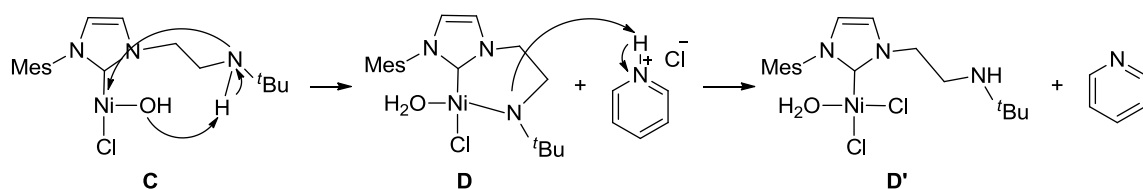
Scheme 4.9: Proposed reactivity between a Ni<sup>II</sup>-OH and py•HCl.

However, as previously proposed in Section 3.2, if the Ni-OH intermediate (**C**) is sufficiently basic it could deprotonate the secondary amine of the NHC ligand to give an aquo complex (**D**). Dissociation of water could give **E** that could dimerize through the chloro ligands to give **F**. Lastly, protonation of the amide ligand from py•HCl could lead to the formation of the dimer species **G** (Scheme 4.10).



Scheme 4.10: Potential reaction of the secondary amine on the NHC ligand with  $\text{Ni}^{\text{II}}\text{-OH}$  (**C**) and  $\text{py}\cdot\text{HCl}$  to form dimer species **G**.

Another possible reaction pathway starts from **C** and once again forms **D** on deprotonation of the amine, but the water does not dissociate to form **E** as above. Instead, **D** reacts with the  $\text{py}\cdot\text{HCl}$  to form the aquo complex **D'** (Scheme 4.11).



Scheme 4.11: Potential reaction of the secondary amine on the NHC ligand with  $\text{Ni}^{\text{II}}\text{-OH}$  (**C**) and  $\text{py}\cdot\text{HCl}$  to form the Ni-aquo complex **D'**.

It is conceivable that **Int. 2** could be the dimer **F** or the aquo complex **D**. In both cases the deprotonated amide of the NHC ligand could react with  $\text{py}\cdot\text{HCl}$  to form the dimer species **F** or the aquo complex **D'**. While the  $\text{p}K_{\text{aDCM}}$  of the secondary amine in **C** is not known, the  $\text{p}K_{\text{aMeCN}}$  of  $\text{R}_2\text{NH}$  ( $\text{R} = \text{methyl, ethyl, isobutyl, butyl}$ ) was found to be in the range of 17.88-18.75.<sup>63</sup> The  $\text{p}K_{\text{aMeCN}}$  of  $\text{py}\cdot\text{HCl}$  is lower than the  $\text{p}K_{\text{aMeCN}}$  of the amines, indicating that the protonation of **F** (to form **G**) or **D** (to form **D'**) are favorable reactions. If this reaction is dominant then the  $\text{p}K_{\text{aMeCN}}$  of the aquo ligand in **D** must be greater than 18. Future studies will target the deconvolution of these two possible protonation routes. Such a study would be beneficial as  $\text{Ni}^{\text{II}}\text{-OH}$  compounds are suggested to be basic, but to

the best of our knowledge, there have been no systematic studies to determine their  $pK_a$ . To better ascertain the  $pK_{aDCM}$  of **C**, different acids would be added with varying  $pK_a$  values. If the reaction does not proceed at a certain  $pK_a$  value, then it could indicate which reaction pathway was observed.

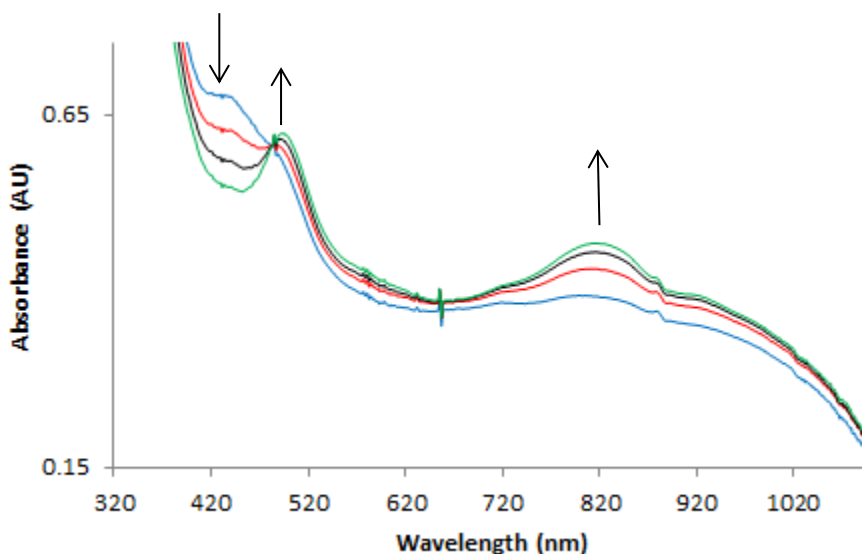


Figure 4.11: **Int. 2** (blue), with: 0.2 molar equivalence  $py\cdot HCl$  (red), 0.4 molar equivalence  $py\cdot HCl$  (black), and 0.6 molar equivalence  $py\cdot HCl$  (green). The reaction time between each trace is 10 minutes.

After 0.8 molar equivalents of acid added to **Int. 2**, the UV-vis spectra changes again, but does not display an isosbestic point, nor does it display an increase in the same bands as previously observed. This observation was not consistent with the formation of a single reaction product, and was presumed to form multiple products (Figure 4.12). Given that only 0.6 equivalents  $H^+$  were needed to protonate **Int. 2**, it was presumed that **Int. 1** to **Int. 2** does not undergo complete conversion, and this was determined by  $^1H$  NMR spectroscopy (*vide infra*). A possible reaction pathway that could occur upon the addition of excess acid is protonation of the carbene carbon of the NHC ligand, forming  $H[NHC]Cl$  and an equivalent of  $NiCl_2(py)_2$  (Scheme 4.12). This reaction pathway is supported by the observation that  $H[NHC]^+$  and  $NiCl_2(py)_4$  are decomposition products in room temperature oxidation reactions even in the absence of added acid. The addition of  $py\cdot HCl$  may increase the proportion of material going through this decomposition pathway.

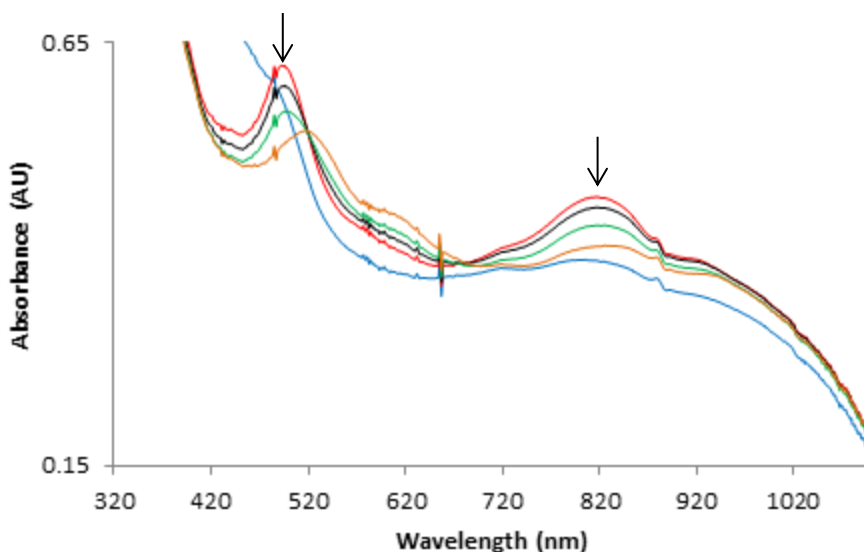
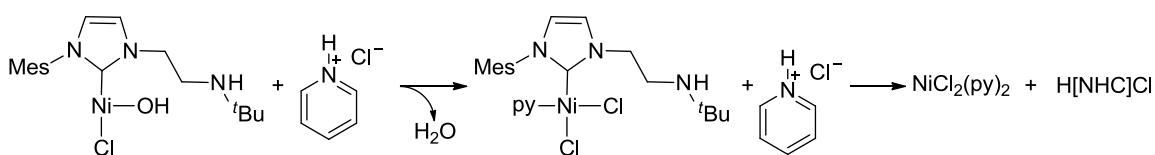


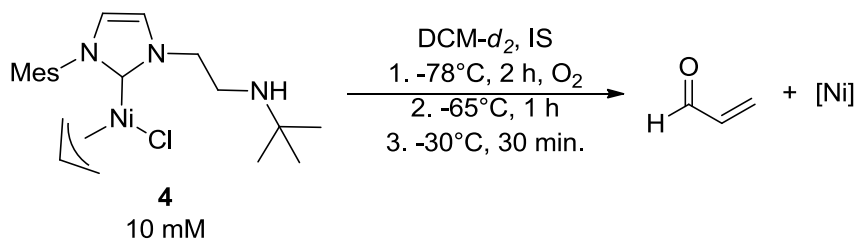
Figure 4.12: **Int. 2** (blue), with 0.6 molar equivalents  $\text{py}\cdot\text{HCl}$  (red), 0.8 molar equivalents  $\text{py}\cdot\text{HCl}$  (black), 1.0 molar equivalents  $\text{py}\cdot\text{HCl}$  (green), and 1.2 molar equivalents  $\text{py}\cdot\text{HCl}$  (orange).



Scheme 4.12: Proposed decomposition pathway upon addition of excess  $\text{py}\cdot\text{HCl}$  to **Int. 2**. Py = pyridine.

#### 4.4 Investigation of Oxidation Intermediates by Variable Temperature of $^1\text{H}$ NMR Spectroscopy

With the temperatures required for intermediate formation and trapping now known from the UV-vis experiments, low temperature  $^1\text{H}$  NMR spectroscopy was performed on a 10 mM sample of **4** with 10 mM 1,3,5-trimethoxybenzene as an internal standard (Scheme 4.13). The NMR tube was cooled to  $-85\text{ }^\circ\text{C}$ , and the headspace was flushed with  $\text{O}_2$ , following a similar methodology as the UV-vis experiments above to form **Int. 1**.



Scheme 4.13: Reaction of 10 mM **4** with  $O_2$  to determine the identities of the Ni oxidation intermediates. IS = 1,3,5-trimethoxy benzene.

After allowing **Int. 1** to form over a 2 hour period, complete consumption of the starting material was observed (Figure 4.13). The sweep width of the  $^1H$  NMR spectrum was expanded from  $-200$  to  $+200$  ppm, but no paramagnetically shifted signals were observed. There are broadened signals between the 0.5-3.0 ppm region, but they appear to match to the minor signals observed in the starting material. Based on the loss and broadening of signals from the observed  $^1H$  NMR spectrum, it was believed that **Int. 1** is a paramagnetic species. There are two possible reasons for this; either **Int. 1** is 1) a  $Ni^{III}$  species, or 2) a tetrahedral  $Ni^{II}$  species.

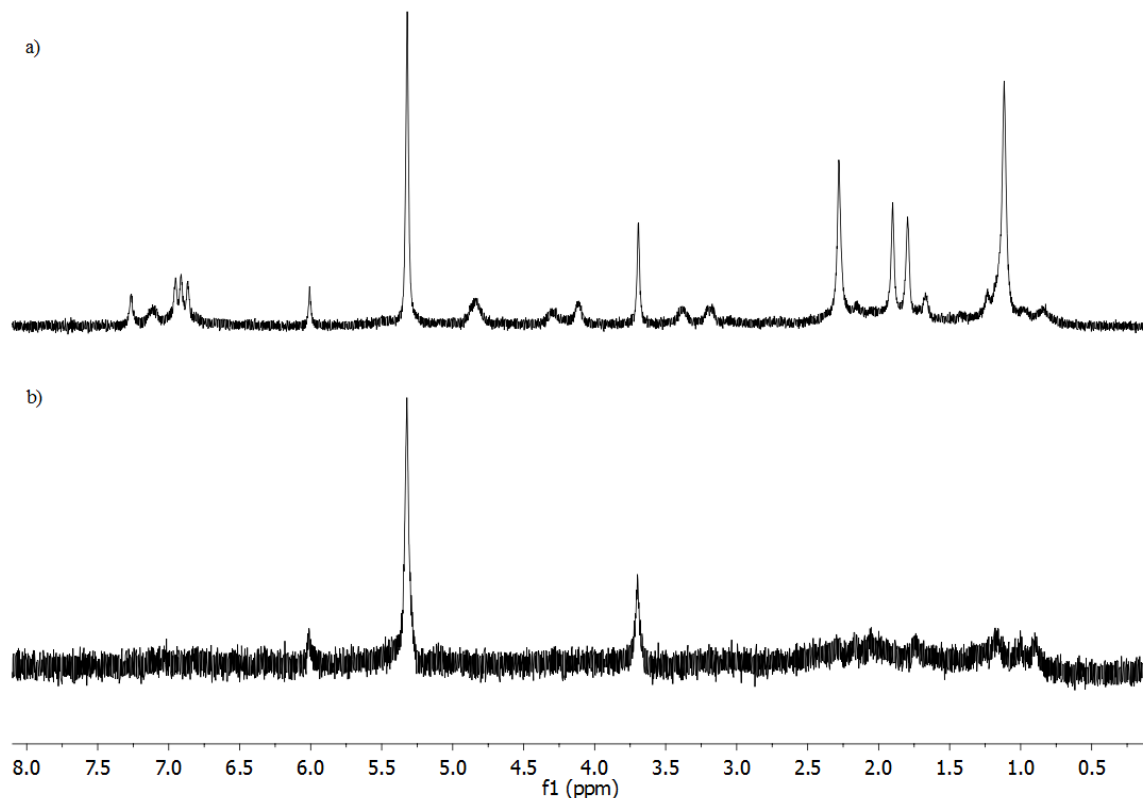


Figure 4.13: Stacked  $^1\text{H}$  NMR spectra of 10 mM **4** in  $\text{DCM-}d_2$  with trimethoxybenzene as the internal standard a) at  $-78^\circ\text{C}$ , and b) after addition of  $\text{O}_2$  and reaction for 2 h. at  $-78^\circ\text{C}$ .

While  $^1\text{H}$  NMR spectroscopy is routinely used to determine chemical structures, it is unable to determine the structure of paramagnetic species. However, the number of unpaired electrons can be determined through Evans' method analysis, which can give indirect insight into the structure. The reaction was repeated using the same conditions above, except a sealed capillary tube of 1:8  $\text{DCM}:\text{DCM-}d_2$  was also placed in the NMR tube. After the formation of **Int. 1**, there were two signals in the region for  $\text{DCM-}d_2$ , indicating successful formation of a paramagnetic species. This additional signal occurs because the  $\text{DCM-}d_2$  that was in the same solution as **Int. 1** interacts with the paramagnetic species and causes the solvent signal to be shifted, while the solvent in the capillary tube will not be affected and acts as a reference (Figure 4.14). The solvent signal has shifted downfield 0.11 ppm. From the Evans' method calculations (Appendix, Equations 1-3), the magnetic susceptibility of **Int. 1** was found to be  $2.86 \times 10^{-3} \text{ cm}^3 \text{ mol}^{-1}$ , which correlates to an effective magnetic moment ( $\mu_{\text{eff}}$ ) of  $2.02 \mu_{\text{B}}$ . The spin-only

approximation shows that for one unpaired electron,  $\mu_{\text{eff}}$  is  $1.73 \mu_{\text{B}}$ , and  $2.83 \mu_{\text{B}}$  for two unpaired electrons. The obtained  $\mu_{\text{eff}}$  value was closer in magnitude to one unpaired electron rather than two, leading to a tentative assignment of one unpaired electron on the nickel center.

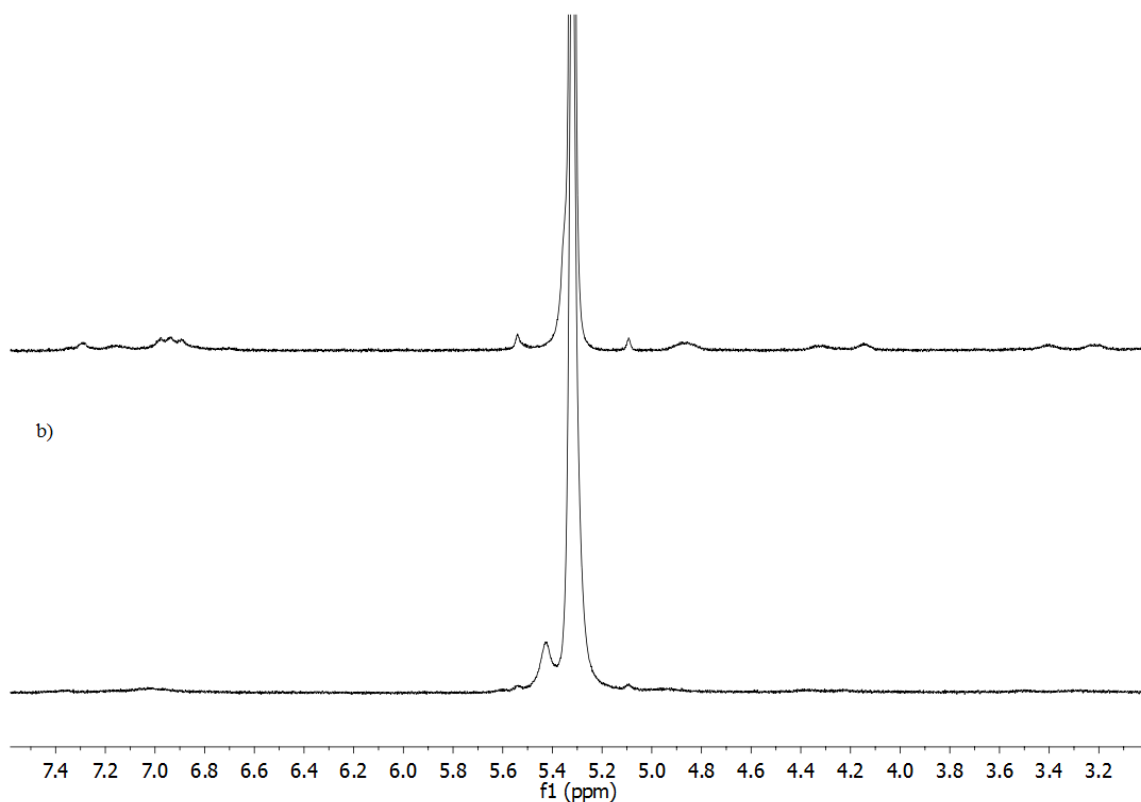


Figure 4.14: Pertinent region of the  $^1\text{H}$  NMR spectrum of 10 mM **4** with a DCM:DCM- $d_2$  sealed capillary present at  $-78\text{ }^\circ\text{C}$  a) before  $\text{O}_2$  addition, and b) 2 hours after  $\text{O}_2$  addition.

The d-orbital splitting of some of the structural candidates for **Int. 1** were then considered. A high-spin tetrahedral  $\text{Ni}^{\text{III}}$  species, a high spin square pyramidal  $\text{Ni}^{\text{III}}$ , a low spin square pyramidal  $\text{Ni}^{\text{III}}$ , and a high spin  $\text{Ni}^{\text{II}}$  were considered (Figure 4.16). **Int. 1** was unlikely to be a  $d^8$  tetrahedral high-spin  $\text{Ni}^{\text{II}}$  complex, as the idealized  $\mu_{\text{B}}$  value for high-spin tetrahedral  $\text{Ni}^{\text{II}}$  complexes is  $4.2 \mu_{\text{B}}$ .<sup>74</sup> If **Int. 1** was a superoxo species with the  $\text{O}_2$  moiety in either the side-on or end-on forms, one electron from the nickel center must couple with an electron from the oxygen molecule giving a  $\text{Ni}^{\text{III}}$  metal center. This leaves one unpaired electron on the oxygen atom that can interact with the electrons found on the metal center (Figure 4.15). This electron from the oxygen atom can interact with the

electrons on the nickel center in one of two ways: ferromagnetic coupling, where the electron spins in the same direction as the metal-based electrons, or antiferromagnetic coupling, where the electron spins in the opposite direction to the electrons found on the nickel center.<sup>75</sup>

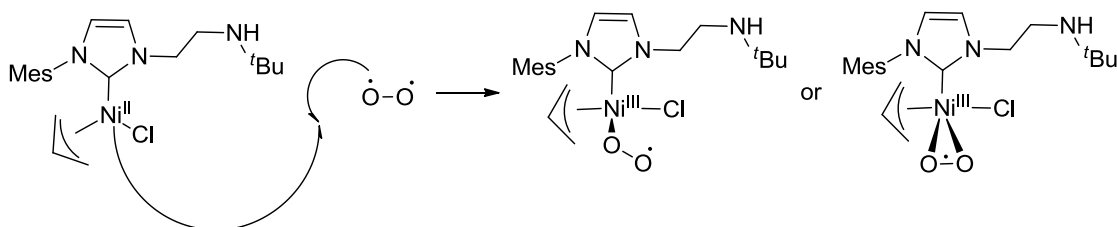


Figure 4.15: Formation of potential superoxo species from **4** and O<sub>2</sub>.

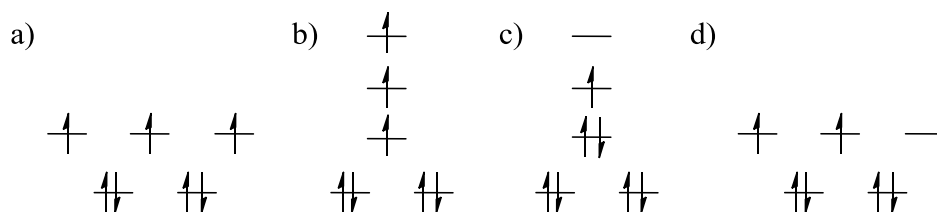


Figure 4.16: Crystal field d-orbital splitting of: a) tetrahedral Ni<sup>III</sup>, b) high-spin square pyramidal Ni<sup>III</sup>, c) low-spin square planar Ni<sup>III</sup>, and d) high-spin tetrahedral Ni<sup>II</sup>.

From the above figure, the spin states for each case were determined with an additional unpaired electron ( $S = \pm 1/2$ ) from the superoxo for ferromagnetic coupling and then anti-ferromagnetic coupling, respectively. For a), the overall spin state is either 2 or 1, for b), the overall spin state is once again 2 or 1, and c) has an overall spin state of 1 or 0. In case a) and b), there are at minimum two unpaired electrons, and either two or zero unpaired electrons in case c). However, the Evans' method analysis shows a  $1/2$  spin state from one unpaired electron, which is inconsistent Ni<sup>III</sup>-superoxo structure. From the HAT and N<sub>2</sub> sparging reactions and now the Evans method analysis, it seemed unlikely that **Int. 1** contains a superoxo. Instead, it was believed that **Int. 1** is a different intermediate that is formed further along the oxidation pathway. If this later structure did not contain a superoxo radical, then the low spin square planar Ni<sup>III</sup> center would match to the observed spin state.



Next, the sample of **Int. 1** was warmed to  $-65\text{ }^{\circ}\text{C}$ , following an analogous procedure as above for the UV-vis experiments. A singlet is observed at 9.5 ppm, which correlates to the aldehyde proton of authentic propenal, meaning that oxidation of the organic ligand has occurred at  $-65\text{ }^{\circ}\text{C}$  (Figure 4.17). The other signals for propenal are observed and integrate for their expected values. Additionally, the observed signal matched to that of the authentic propenal, meaning it is likely unbound from the metal center. As the temperature was increased, the propenal signal did not shift, giving further evidence that it was unbound. At  $-65\text{ }^{\circ}\text{C}$  propenal was formed in a 39% yield compared to the starting complex **4**. The formation of the organic product at  $-65\text{ }^{\circ}\text{C}$  means that the energy barrier to oxidation is much lower than Sigman's observations.<sup>49</sup> The formation of propenal also indicates that **Int. 2** may be a hydroxo species or another intermediate further along the reaction coordinate (Scheme 4.1).

There are also a number of broad and weak signals observed in the  $^1\text{H}$  NMR spectrum which should account for the remainder of the material. There was a broad peak observed at  $-1\text{ ppm}$  and was tentatively assigned as a monomeric  $\text{Ni}^{\text{II}}\text{-OH}$  signal, as the analogous signal in related monomeric  $\text{Ni}^{\text{II}}\text{-OH}$  are found upfield of 0 ppm, ranging from 0 to  $-4\text{ ppm}$ .<sup>51, 76</sup> Assuming this signal accounts for a single proton, it represents 39% of the Ni product as compared to the starting Ni complex **4**. In support of this assignment, the broad signal is in a 1:1 ratio with the propenal signal. The aryl region integrates low however assuming that there is one NHC ligand on the possible  $\text{Ni}^{\text{II}}\text{-OH}$  species. Given this inconsistency, the assignment of **Int. 2** as a diamagnetic  $\text{Ni}^{\text{II}}\text{-OH}$  is tentative at best.

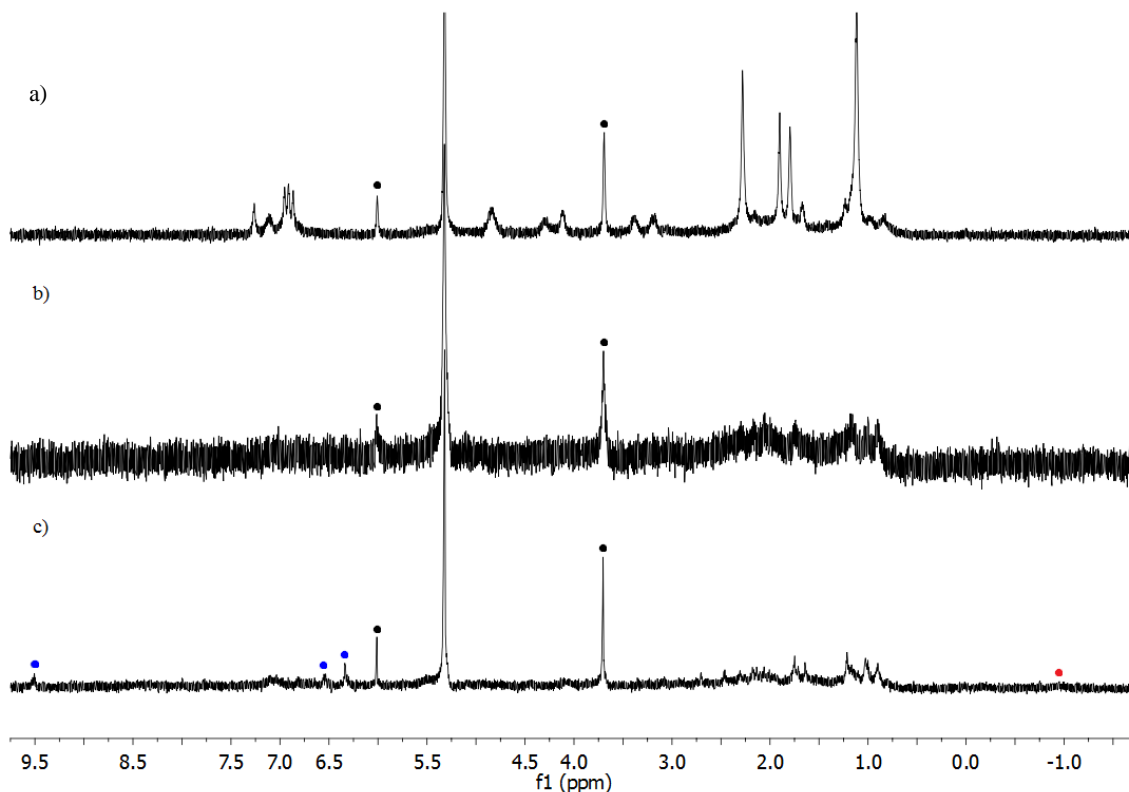


Figure 4.17: Stacked  $^1\text{H}$  NMR spectra of 10 mM **4** in  $\text{DCM-}d_2$  with trimethoxybenzene as an internal standard: a) at  $-78\text{ }^\circ\text{C}$  before  $\text{O}_2$  addition, b)  $-78\text{ }^\circ\text{C}$  2 hours after  $\text{O}_2$  addition, and c) warmed to  $-65\text{ }^\circ\text{C}$  for one hour. ● indicates propenal, ● is the broadened signal, and ● indicates the internal standard.

From the Evans method analysis of **Int. 2**, the paramagnetic solvent shift remained after **Int. 2** was formed (Appendix 8.1). The paramagnetic shift remained as the temperature was increased, and the  $\mu_{\text{eff}}$  value also increased as it was temperature dependent (Appendix 8.2). This leads to a final value of  $2.61\ \mu_{\text{B}}$ , which was closer to the expected value for two unpaired electrons. This means that the species observed at  $-65\text{ }^\circ\text{C}$  may actually be a mixture of species that contains a paramagnetic species.

Upon raising the temperature again to  $-40\text{ }^\circ\text{C}$ , the  $^1\text{H}$  NMR spectrum remains relatively unchanged with one exception. The signal at  $-1\text{ ppm}$  has shifted to  $-0.5\text{ ppm}$  and accounts for 46% of the material observed in the  $^1\text{H}$  NMR spectrum. The remainder of the material cannot be accurately determined as there are paramagnetic species present. This new signal is in a 0.94:1 ratio with the propenal signal, and is still broad. This broad signal continues to shift further downfield as the temperature increases, reaching a final peak

position of 0.5 ppm at 25 °C (Figure 4.18). This signal was still found in an approximately 1:1 ratio with propenal, and was formed in a 77% overall yield. There was also a downfield signal observed at 10.56 ppm, which accounts for 23% of the material observed, and was in an expected range for  $\text{H}[\text{NHC}]^+$  since authentic imidazolium salt is found at 10.34 ppm in  $\text{CDCl}_3$ . There is also a set of signals consistent with  $\text{NiCl}_2(\text{NHC})_2$ , and accounts for 5% of the observed material. However, as the previous observations have found a ~10% yield in  $\text{C}_6\text{D}_6$  and the literature reports that related  $\text{NiCl}_2(\text{NHC})_2$  complexes are unstable in polar solvents, this assignment was tentative.<sup>50</sup>

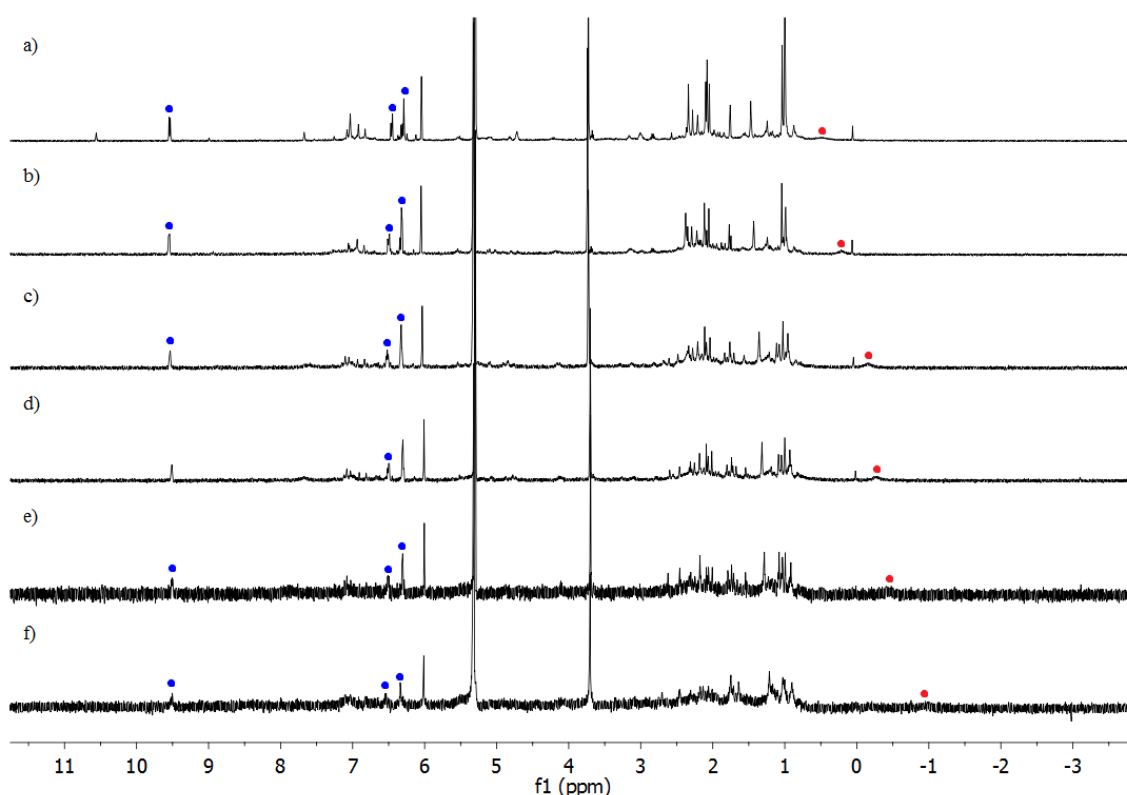


Figure 4.18:  $^1\text{H}$  NMR stack plot of 10 mM **4** with trimethoxybenzene as the internal standard, at a) 25 °C, b) 0 °C, c) -25 °C, d) -30 °C, e) -40 °C, f) -65 °C. • indicates the position of the broadened signal, • indicates propenal.

In conclusion, two distinct intermediates were detected by UV-vis spectroscopy: one at -78 °C, and another at -65 °C. These were labelled **Int. 1** and **Int. 2**, respectively. **Int. 1** was found to undergo rapid reactivity with  $\text{O}_2$ , and did not react with the  $\text{H}^\bullet$  donor DPH to form azobenzene as a byproduct. **Int. 1** was found to be paramagnetic by  $^1\text{H}$  NMR

spectroscopy. **Int. 2** was found to react with 0.6 molar equivalents of py•HCl, and was found to undergo further reactivity upon addition of more acid. The basic site on **Int. 2** for the observed reactivity with py•HCl (i.e. Ni<sup>II</sup>-OH or ligand amide) is currently unknown. All observed reactions in the sequence were found to be thermally irreversible. After the formation of **Int. 2**, free propenal was observed, indicating that the oxidation reaction occurred successfully, and that **Int. 2** was not an O<sub>2</sub> adduct. Paramagnetic species were also observed in the sample containing **Int. 2**, and were observed throughout the remainder of the reaction. From this analysis, the most likely candidate for **Int. 1** was a propenal-bound Ni<sup>II</sup>-OH intermediate, as it is expected to be non-reactive to N<sub>2</sub> sparging and HAT agents. However, the Evans method analysis suggests that **Int. 1** should be a low-spin square planar Ni<sup>III</sup>, of which there was no suitable structure from the scheme above (Scheme 4.1). A tentative assignment of **Int. 2** is the monomeric Ni<sup>II</sup>-OH with propenal released (Figure 4.19). This is supported by the observation of free propenal in the <sup>1</sup>H NMR spectra.

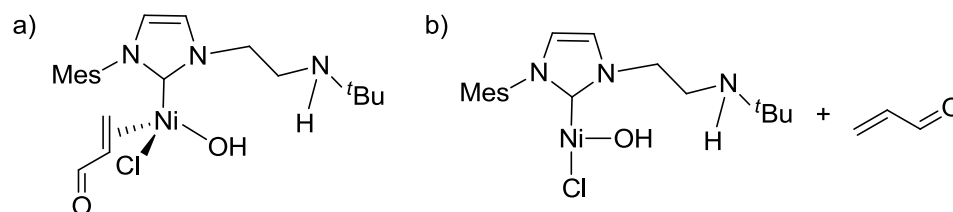


Figure 4.19: Proposed intermediate structure of: a) **Int. 1** and b) **Int. 2**.

## Chapter 5

### 5 Determination of Reaction Intermediates by Density Functional Theory and Time Dependent Density Functional Theory

#### 5.1 Determination of Reaction Intermediates by Density Functional Theory

While the experimental results from Chapter 4 are insightful, they did not precisely determine the intermediate structures formed upon aerobic oxidation of **4**. To obtain better insight into the reaction intermediates, density functional theory (DFT) and time dependent DFT (TD-DFT) were additionally employed.

The optimized structures for the relevant intermediates for the oxidation of **4** were built using known bonding parameters from known crystal structures for related compounds.<sup>53-54, 61</sup> The NHC ligand in all compounds was truncated, using a Ph group in place of the Mes, and a methyl group in place of the <sup>t</sup>Bu group. This truncation was performed to reduce the computational time and resources required. The complexes were constructed in both the square planar and tetrahedral geometries where applicable (e.g. **Int. 1**). Hydrogen bonding interactions for possible structures of **Int. 2** were modelled using bond lengths and angles crystallographically determined in a similar Ni(NHC) complex that has a hydrogen bonding interaction between a Ni-OH moiety and a ligand pendent amide group (Figure 5.1).<sup>53</sup> The complexes were geometrically optimized in the gas phase with the B3LYP<sup>77</sup> method and the 6-31G(d) basis set for C, H, N, O, Cl and the LANL2DZ basis set for nickel. The optimized geometries were then studied to ensure that the standard bond lengths were within 0.01-0.02 Å of the crystal structure. After obtaining the optimized geometries, the thermodynamic properties of the complexes were obtained at -65 °C (208.15 K) using the same level of theory.

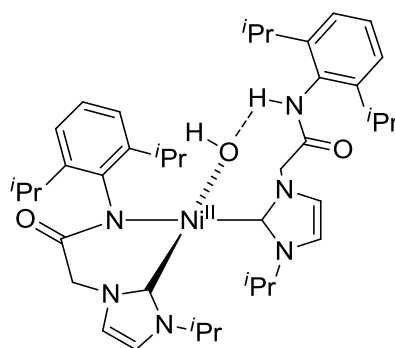


Figure 5.1: Ni-NHC complex used to model hydrogen-bonding interactions for computational methods.

First, the starting complex **4** was geometrically optimized (Figure 5.2).<sup>54</sup> The square planar geometry of the complexes was studied (**I**, Figure 5.2), as X-ray crystallography and <sup>1</sup>H NMR spectroscopy conclusively point toward a square planar diamagnetic orientation. Structure **I** contains a  $\kappa^1$ -C NHC ligand and a  $\eta^3$  allyl ligand, which was the same as the crystal structure of **4**.<sup>54</sup> The complex was also modelled as conformer **II**, a five-coordinate square pyramidal structure, with the pendent nitrogen atom of the NHC bonding in the axial site of the complex (**II**, Figure 5.2). A square planar  $\kappa^2$ -NHC  $\kappa^1$ -allyl complex was also modeled (**III**, Figure 5.2). A tetrahedral analogue of **III** was optimized as well, but an acceptable energy minimum was not found.

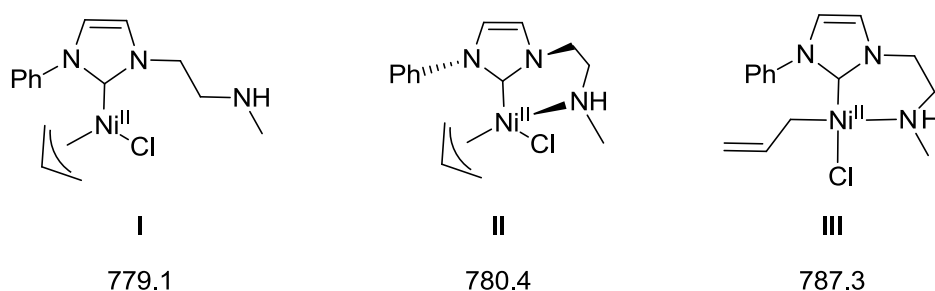


Figure 5.2: Optimized structures for compound **4** used for thermodynamic analysis at  $-65\text{ }^\circ\text{C}$ , with the corresponding calculated  $\Delta G$  values shown below in  $\text{kJmol}^{-1}$ .

From the initial analysis of the thermodynamic properties, structure **I** was the most energetically stable species at  $-65\text{ }^\circ\text{C}$ . Structure **II** was  $1.3\text{ kJmol}^{-1}$  higher in energy than **I**. This energy gap is quite small, and indicates that the  $\kappa^2$ -CN NHC binding mode is readily accessible. Structure **III** was  $8.2\text{ kJmol}^{-1}$  higher in energy than **I**. While this

energy gap is larger, it is still within reason that the complex could adopt this geometry, albeit in small amounts. This correlates well to the  $^1\text{H}$  NMR data previously obtained which shows that **4** was fluxional until temperatures of  $-70\text{ }^\circ\text{C}$ .<sup>54</sup> The low temperature  $^1\text{H}$  NMR data is also consistent with either **I** or **II**, as the allyl ligand was clearly found in a  $\eta^3$ -coordination mode. This means that all three of these structures are potential starting points for the oxidation reactivity, although **I** and **II** are the most likely observed species.

Next, the possible oxidation intermediates were modelled. To accomplish this, the thermodynamic properties of  $\text{O}_2$  were calculated, and found  $\Delta G = -26.2\text{ kJmol}^{-1}$ . The energy values calculated for **I-III** were determined including a molecule of  $\text{O}_2$ . The resulting energy for **I** plus  $\text{O}_2$  was set to  $0\text{ kJmol}^{-1}$  to be used as a reference for the upcoming intermediate structures along the reaction pathway.

Three different Ni- $\text{O}_2$  adduct structures were considered. The first, **IV**, is an end-on superoxo, a structure that was previously proposed as an oxidation intermediate by Sigman (**IV**, Figure 5.3).<sup>49</sup> Secondly, there has been literature precedence for a side-on superoxo structure, and it was deemed pertinent that the structure be considered for our system as well (**V**, Figure 5.3).<sup>34, 36</sup> Two other structures were considered as well, **VI** and **VII**. Structure **VI** was modelled as a square planar species with an end on superoxo *trans* to the  $\kappa^1$ -allyl ligand, but an acceptable optimized structure was not found. Structure **VII** was considered as Sigman found that  $\text{O}_2$  binding occurred through the apical position, but was not modelled as it is proposed to rapidly isomerize to **IV** for the subsequent reaction steps.<sup>50</sup>

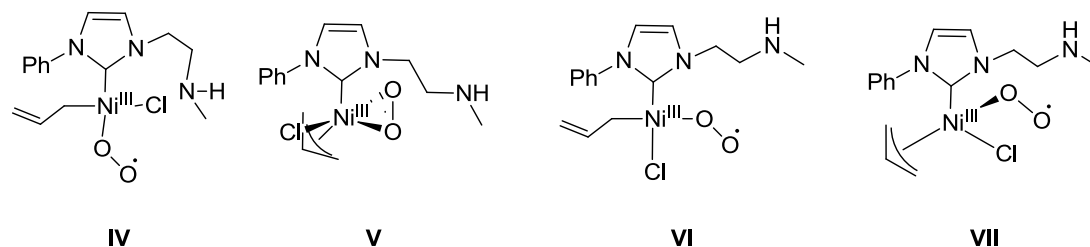


Figure 5.3: Ni- $\text{O}_2$  adducts studied to determine the reaction pathway.

A tetrahedral structure of **IV** was considered, but after the optimization procedure, a square planar structure was returned as the most stable version. Additionally, a hydrogen

bonding interaction between the pendent amine of the NHC and the superoxo ligand was modelled in variations of both **IV** and **V**, however no acceptable energy minima were found.

Structure **IV** was  $39 \text{ kJmol}^{-1}$  higher in energy than **I** (the most stable conformer of **4** plus  $\text{O}_2$ ). Structure **V** was  $43.1 \text{ kJmol}^{-1}$  higher in energy than **I**. Structure **V** was  $5.7 \text{ kJmol}^{-1}$  higher in energy than **IV**. These energy differences between the Ni- $\text{O}_2$  adducts are relatively small, and indicates that both of the proposed structures are potential intermediates (Figure 5.4).

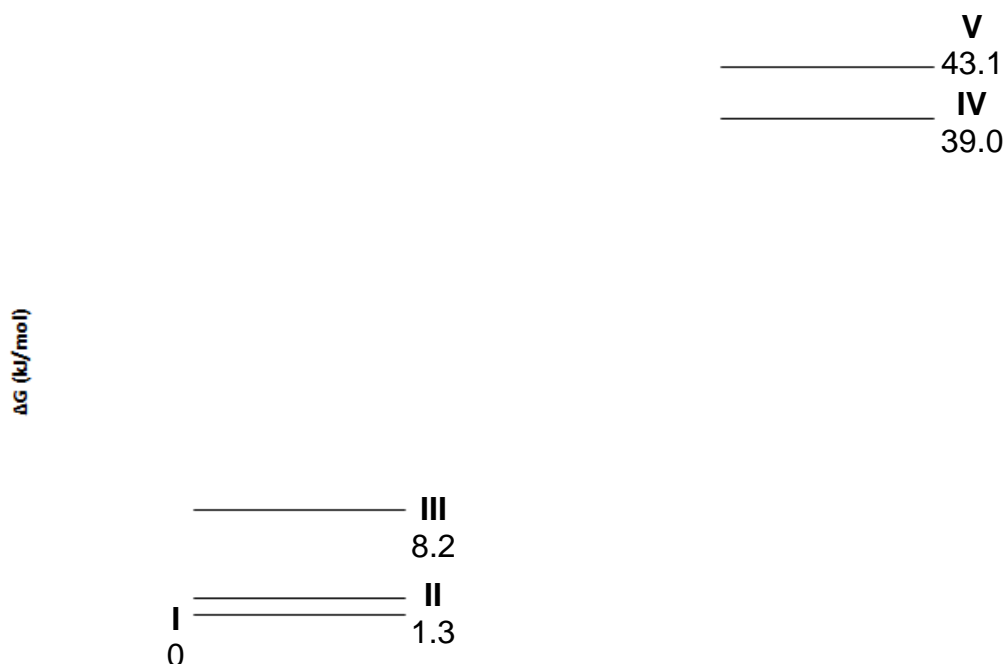


Figure 5.4: Thermodynamic plot for the conversion of structures **I-III** to the proposed Ni- $\text{O}_2$  adducts, **IV** and **V**. Numbers are energy differences from **I** in  $\text{kJmol}^{-1}$ .

During an optimization procedure, a serendipitous structure was found, where an organoperoxo metallocycle was formed (**VIII**, Figure 5.5). While this structure was not proposed by Sigman, the reported results from Sigman did not have experimental evidence for the species formed between the superoxo and the final  $\mu$ -OH dimer. As a result, the metallocycle structure was further studied to determine its relevance to the mechanism. The metallocycle structure was successfully optimized in both a tetrahedral



(**VIII**) and a square planar (**IX**) structure (Figure 5.5). Structure **VIII** is  $36.3 \text{ kJmol}^{-1}$  higher in energy than **I** (Figure 5.6). Structure **IX** is  $45.4 \text{ kJmol}^{-1}$  higher in energy than **I**. Based on the  $^1\text{H}$  NMR spectroscopy data, the first observed intermediate structure (**Int. 1**) was inferred to be paramagnetic. Since **IX** is expected to be diamagnetic, it is not a likely candidate for **Int. 1**.

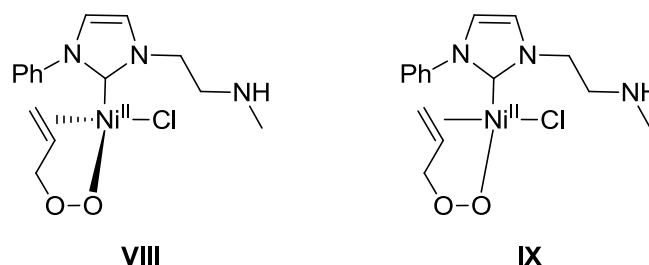


Figure 5.5: Structure of potential metallocycle intermediates **VIII** and **IX**.

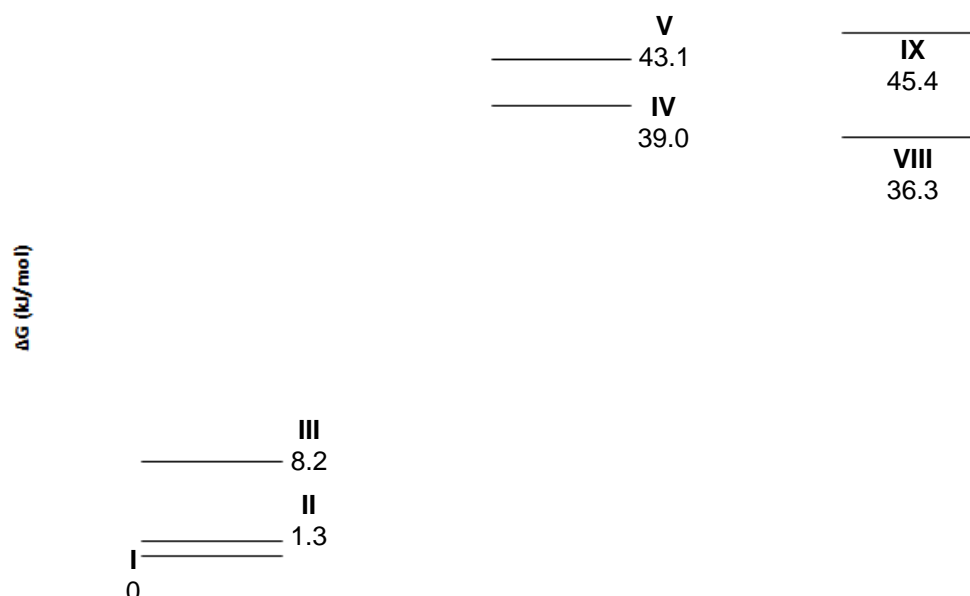


Figure 5.6: Reaction coordinate showing different conformations of **4** with  $\text{O}_2$  (**I-III**),  $\text{Ni}^{\text{III}}\text{-O}_2$  adducts **IV** and **V**, and the metallocycles **VIII** and **IX**. Numbers are energy differences from **I** in  $\text{kJmol}^{-1}$ .

From the thermodynamic analysis thus far, the majority of the species studied have very similar energy values, making an assignment for **Int. 1** challenging. When the results of the HAT reaction are considered, **VIII** would describe the observed results well, as there

is no free radical present to undergo a HAT reaction. Also, due to its tetrahedral geometry, it would be a paramagnetic species, which was inferred by  $^1\text{H}$  NMR spectroscopy. As a result, **Int. 1** is tentatively assigned as structure **VIII**.

The next structure considered along the reaction coordinate was the propenal bound  $\text{Ni}^{\text{II}}$ -OH structure **X** (Figure 5.7). **X** was chosen for analysis as it is the final proposed intermediate by Sigman before product release and subsequent dimerization of the low coordinate  $\text{Ni}^{\text{II}}$ -OH species.<sup>49</sup> Sigman had previously portrayed this complex with a  $\pi$ -bond interaction between the carbonyl and the nickel center. However, alkenes are better ligands than carbonyls, which is why the complex is modelled as shown below. Structure **X** is  $43.3 \text{ kJmol}^{-1}$  higher in energy than **I**. Intermediate **X** is also  $7 \text{ kJmol}^{-1}$  higher in energy than the tetrahedral metallocycle **IX** (Figure 5.8). A tetrahedral analogue of **X** was also modelled since **X** could be a potential structure for **Int. 1**. **Int. 1** does not show evidence of propenal by  $^1\text{H}$  NMR spectroscopy, and the structure is inferred to be paramagnetic. The tetrahedral structure of **X** would account for both of these parameters. However, after the optimization process, a square planar structure was returned as the most stable version.

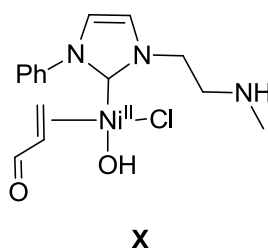


Figure 5.7: Structure of **X**.

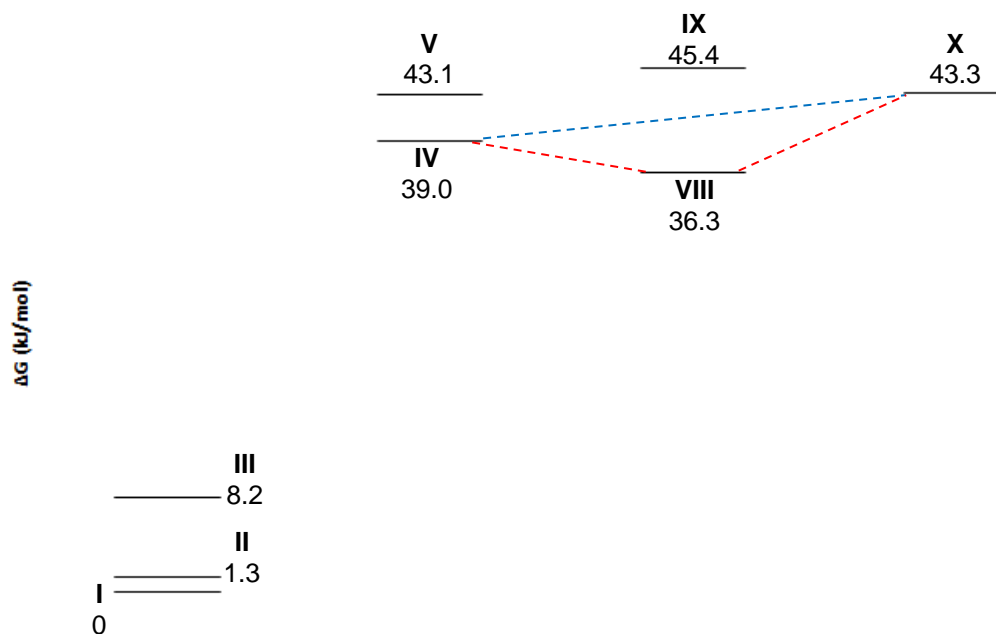


Figure 5.8: Reaction coordinate of different conformations of **4** with O<sub>2</sub> (**I-III**), Ni<sup>III</sup>-O<sub>2</sub> adducts **IV** and **V**, metallocycles **VIII** and **IX**, and the propenal bound intermediate **X**. Numbers are energy differences from **I** in kJmol<sup>-1</sup>. Sigman's proposed reaction pathway (blue dash). Our proposed reaction pathway (red dash).

At this point it is important to note that there are two proposed pathways in the reaction coordinate now. Sigman's proposed reaction (blue dashed line) does not include the metallocycle, and rather goes from the Ni<sup>III</sup>-superoxo species **IV** to the propenal bound Ni<sup>II</sup>-OH structure **X** through a series of unstable intermediate species (Scheme 4.1 of Section 4.1). From our results (red dashed line), the tetrahedral metallocycle **VIII** was an energetically feasible intermediate to be formed before **X**. As a result, an alternate reaction pathway was considered, where **VIII** was formed as a stable intermediate (Figure 5.9). In the proposed reaction scheme, the  $\pi$ -bond of the  $\kappa^1$ -allyl reacts with the superoxo rather than the allylic C-H bond (**IV**) that first forms a metallocycle with a radical in the metallocycle framework. Upon homolytic cleavage of the Ni-C bond, a new C-C  $\pi$ -bond is formed and reduces the Ni<sup>III</sup> to Ni<sup>II</sup> (**VIII**). Lastly, the peroxide bond is homolytically cleaved and C-H abstraction is performed, forming an O-H bond and a C-O  $\pi$ -bond (**X**). Whether this occurs over one or more steps is currently unknown.

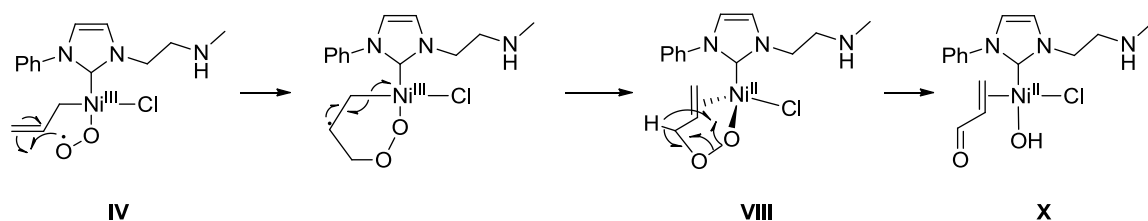


Figure 5.9: Proposed reaction pathway from a Ni<sup>III</sup>-superoxo species that forms the organoperoxo metalocycle **IX** and subsequent reactivity to **XI**.

From **X**, it was proposed that propenal dissociates and forms a monomeric Ni<sup>II</sup>-OH species, and three potential monomeric intermediates were modelled, and they are presented in no particular order (**XI-XIII**, Figure 5.10). First was the Ni<sup>II</sup>-OH structure with a  $\kappa^2$ -NHC binding mode (**XI**). This structure was considered first as it would be coordinatively saturated. Second was the Ni<sup>II</sup>-OH with no secondary interaction from the NHC ligand (**XII**). Lastly was the Ni<sup>II</sup>-OH structure with a hydrogen bond interaction between the pendent amine and the OH group (**XIII**). This structure was modelled since the original goal of including the pendent amine group was to provide a hydrogen bond donor to the hydroxide, which would hopefully offer increased stability. Structure **XIV** was chosen for study as Ni<sup>II</sup>-OH species may be sufficiently basic to deprotonate a secondary amine. Additionally, the observed water in the crystal structures provided further evidence for this type of reactivity (Section 3.2). Structure **XIV** was constructed using the same methodology, but after the geometry optimization procedure, an acceptable energy minimum was not obtained. The obtained  $\Delta G$  values for **XI-XIII** were corrected for a molecule of propenal so as to account for the stoichiometry of the reaction. Tetrahedral structures of **XI** and **XII** were modelled from known crystallographic parameters of related tetrahedral Ni-NHC complexes. However, a square planar geometry was returned as the most stable version after the geometry optimization for both structures.

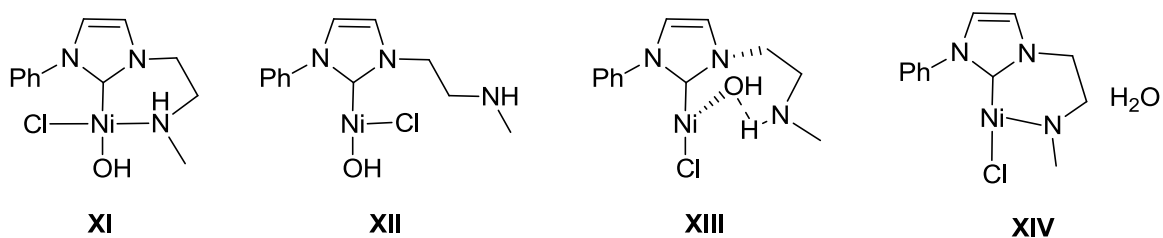


Figure 5.10: Proposed monomeric Ni<sup>II</sup>-OH structures.

Structure **XII** was 7.1 kJmol<sup>-1</sup> lower in energy than **I** (Figure 5.11). It is surprising that **XII** would be the most stable structure, as it is coordinatively unsaturated. Structure **XIII** was 0.4 kJmol<sup>-1</sup> higher in energy than **I**, and 7.5 kJmol<sup>-1</sup> higher in energy than **XII**. This energy difference between **XIII** and **XII** is quite small, and indicates that this hydrogen bond has no noticeable impact on the stability. Structure **XI** was 8.3 kJmol<sup>-1</sup> higher in energy than **I**, despite having all of its coordination sites occupied.

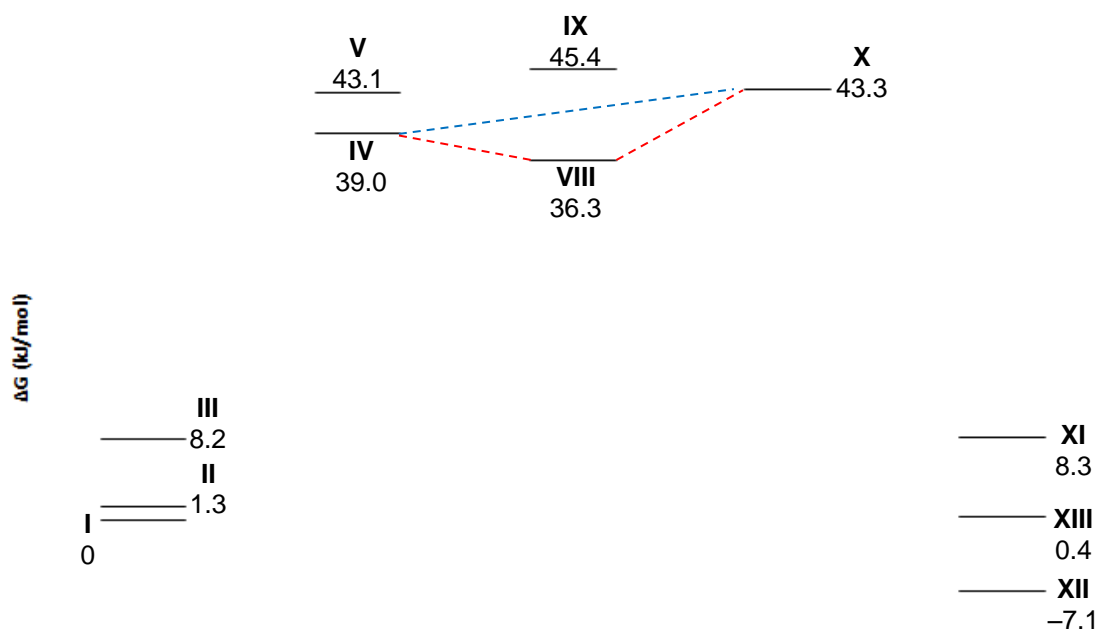


Figure 5.11: Reaction coordinate of the different conformations of **4** with O<sub>2</sub> (**I-III**), Ni<sup>III</sup>-O<sub>2</sub> adducts (**IV** and **V**), metallocycles (**VIII** and **IX**), propenal bound Ni<sup>II</sup>-OH (**X**), proposed monomeric Ni<sup>II</sup>-OH species after propenal release (**XI-XIII**). Numbers are energy differences from **I** in kJmol<sup>-1</sup>. Sigman's proposed reaction pathway (blue dash). Our proposed reaction pathway (red dash).

After these monomeric structures, possible dimeric structures were considered as subsequent intermediates along the reaction path (Figure 5.12). First was **XV**, which was a Ni- $\mu$ OH dimer, and is analogous to the dimer species reported by Sigman *et al.* (**XV**, Figure 5.12). Second was a proposed dimer species in which the nickel centers are bridged by the chloride ligands, but still retain the hydroxo groups (**XVI**, Figure 5.12). The last dimer structure that was studied was a Ni( $\kappa^2$ -NHC)( $\mu$ -Cl) dimer (**XVII**, Figure 5.12). This species was chosen as it is the dehydrated dimer of **XIV**. The  $\Delta G$  values were calculated and corrected for propenal and/or H<sub>2</sub>O where appropriate. To preserve the stoichiometry of the reaction, the final  $\Delta G$  value was divided by two to accurately compare to the monomeric energies.

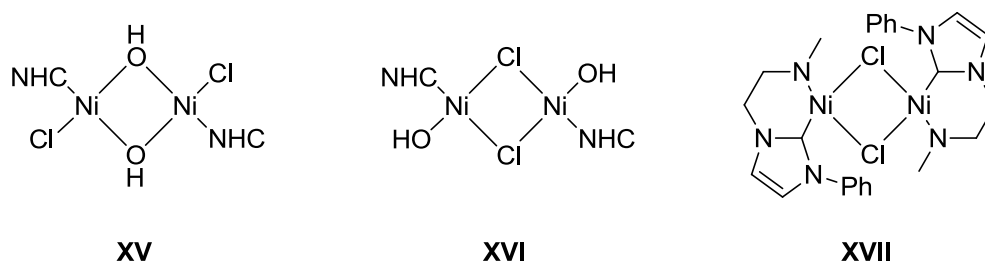


Figure 5.12: Potential dimeric structures studied.

Structure **XVII** was 24.0 kJmol<sup>-1</sup> lower in energy than **I** (Figure 5.13). This stability of the dimer species may indicate that the acidic protons of the pendent amine are promoting unwanted side reactivity. If the reaction was following the same reaction pathway as Sigman's proposed mechanism, a  $\mu$ -OH dimer should be formed as the final product, then it would be expected that **XV** should be the most favorable species to form. However, by <sup>1</sup>H NMR spectroscopy, there was only tentative evidence of a metal-bound hydroxo signal (Figure 4.17 of Section 4.4). There was an absorbance band at ~500 nm observed by UV-vis spectroscopy, which has been reported for Ni- $\mu$ OH dimers, although it was quite weak (Figure 4.5 of Section 4.1).<sup>49-50</sup> Structure **XV** is 24.9 kJmol<sup>-1</sup> higher in energy than **I**, and 49.8 kJmol<sup>-1</sup> higher in energy than **XVII**, making its formation improbable. Structure **XVI** however, could be a potential intermediate, as it is 21.1 kJmol<sup>-1</sup> lower in energy than **I**, and only 3.8 kJmol<sup>-1</sup> higher in energy than **XVII**.

From the DFT results and the experimental data, **Int. 2** cannot yet be conclusively determined. By  $^1\text{H}$  NMR spectroscopy, propenal was observed at  $-65\text{ }^\circ\text{C}$ , and the yield of propenal increases along with the temperature, potentially indicating higher conversion to the monomeric structures (**XI-XIII**). However, it has also been found that upon warming to  $-65\text{ }^\circ\text{C}$ , the sample becomes a mixture of products, and includes some amount of paramagnetic material. Additionally,  $\text{py}\cdot\text{HCl}$  reacts with **Int. 2**, but whether the reaction was occurring between the hydroxo ligand or an amido has yet to be determined. The DFT results do not aid in this analysis much, as the monomeric hydroxo intermediates are all relatively close in energy.

From the dimeric species, **XVII** was the most favorable structure formed, although **XVI** is a possibility as well. It was unlikely that **XV** is being formed as it is  $\sim 50\text{ kJmol}^{-1}$  higher in energy than **XVIII**, and  $\sim 25\text{ kJmol}^{-1}$  higher in energy than **I**.

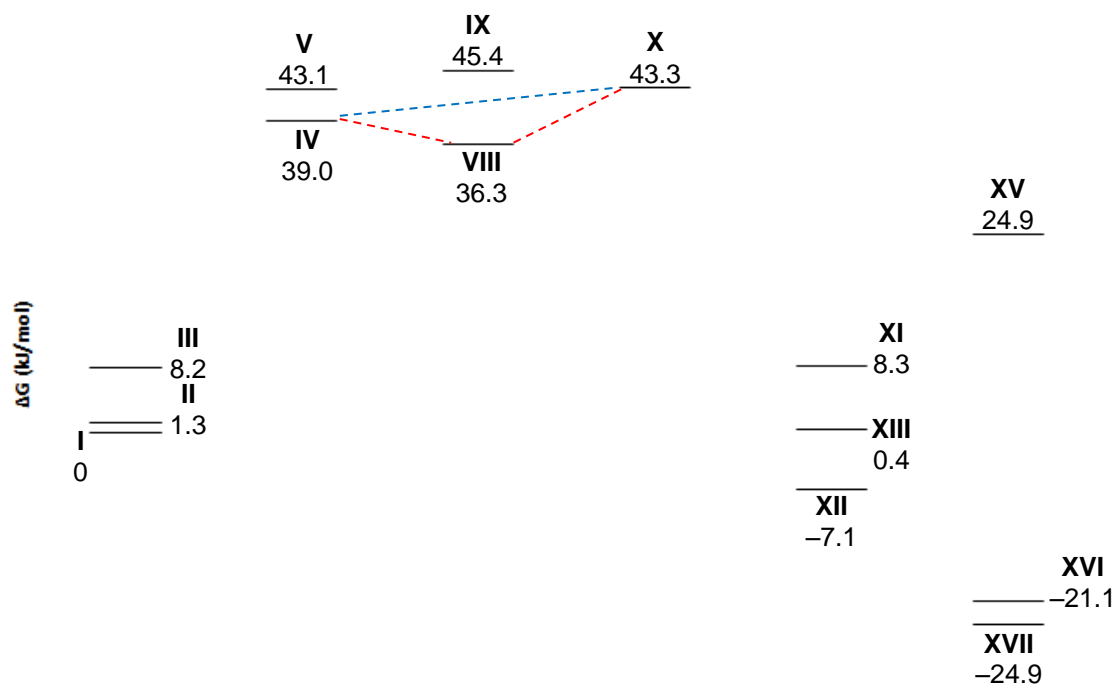


Figure 5.13: Reaction coordinate depicting energy values for the different conformations of **4** with  $\text{O}_2$  (**I-III**),  $\text{Ni}^{\text{III}}\text{-O}_2$  adducts (**IV-V**), metallocycles (**VIII-IX**), propenal-bound  $\text{Ni}^{\text{II}}\text{-OH}$  (**X**), monomeric  $\text{Ni}^{\text{II}}\text{-OH}$  structures (**XI-XIII**), and possible dimeric species (**XV-XVII**). Numbers are energy differences from **I** in  $\text{kJmol}^{-1}$ . Sigman's proposed reaction pathway (blue dash). Our proposed reaction pathway (red dash).

The last structure to be analyzed was the  $\text{NiCl}_2(\text{NHC})_2$  species (**XVIII**), as it was known to form readily from previous decomposition studies (Figure 5.14). While it was not a dimeric species, two molecules of **4** are required to account for all of the atoms. As a result, the calculated  $\Delta G$  value was divided by two to allow for proper comparisons (Figure 5.15). This structure was the most thermodynamically stable species yet, with a corrected energy of  $-125.1 \text{ kJmol}^{-1}$  lower than **I**, and over  $100 \text{ kJmol}^{-1}$  more stable than **XVII**. This shows that this structure was highly favorable to form thermodynamically, although it was still a low yielding product in the experimental analysis of the decomposition products.

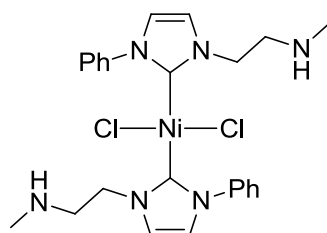


Figure 5.14: Structure of XVIII

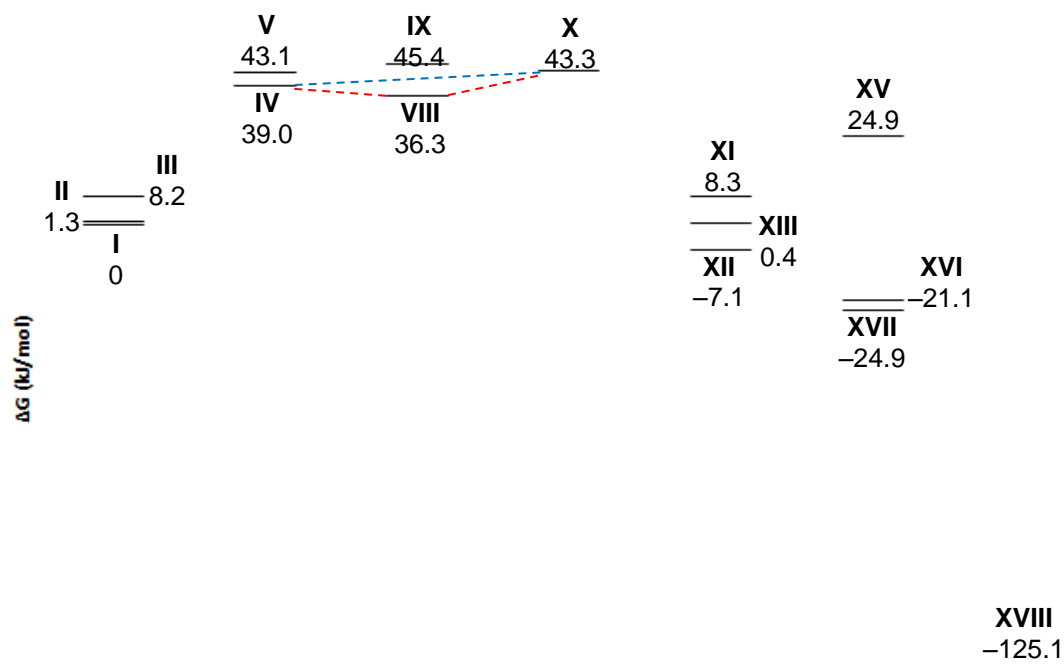


Figure 5.15: Reaction coordinate of the different conformations of **4** with  $\text{O}_2$  (**I-III**),  $\text{Ni}^{\text{III}}\text{-O}_2$  adducts (**IV** and **V**), metallocycles (**VIII** and **IX**), propenal-bound  $\text{Ni}^{\text{II}}\text{-OH}$  (**X**), monomeric  $\text{Ni}^{\text{II}}\text{-OH}$  species (**XI-XIII**),



dimer species (**XV-XVII**) and  $\text{NiCl}_2(\text{NHC})_2$  (**XVIII**). Numbers are energy differences from **I** in  $\text{kJmol}^{-1}$ . Sigman's proposed reaction pathway (blue dash). Our proposed reaction pathway (red dash).

From the above study, there are several key intermediates that have been modelled, but the main problem was that many of the proposed intermediates have very similar energy values. This makes intermediate determination through DFT methods more challenging. From the experimental results and the DFT results obtained here, a proposed reaction is shown below (Figure 5.16). First,  $\text{O}_2$  coordinates to **I** and undergoes oxidation to form a  $\text{Ni}^{\text{III}}$  end-on superoxo (**IV**). Next, **IV** undergoes a series of radical reactions to form **VIII**, which performs a C-H abstraction to give **X**. Next, dissociation of the propenal gives **XII** which dimerizes to form **XVI**. Next, the hydroxo ligands would react with the secondary amines of the NHC ligands to give **XVII**. Experimental evidence shows various decomposition pathways occurred subsequently and these were not considered. From the DFT analysis and experimental evidence, **Int. 1** was proposed to be **VIII**, while **Int. 2** could be **XII**, **XVI**, or **XVII**.

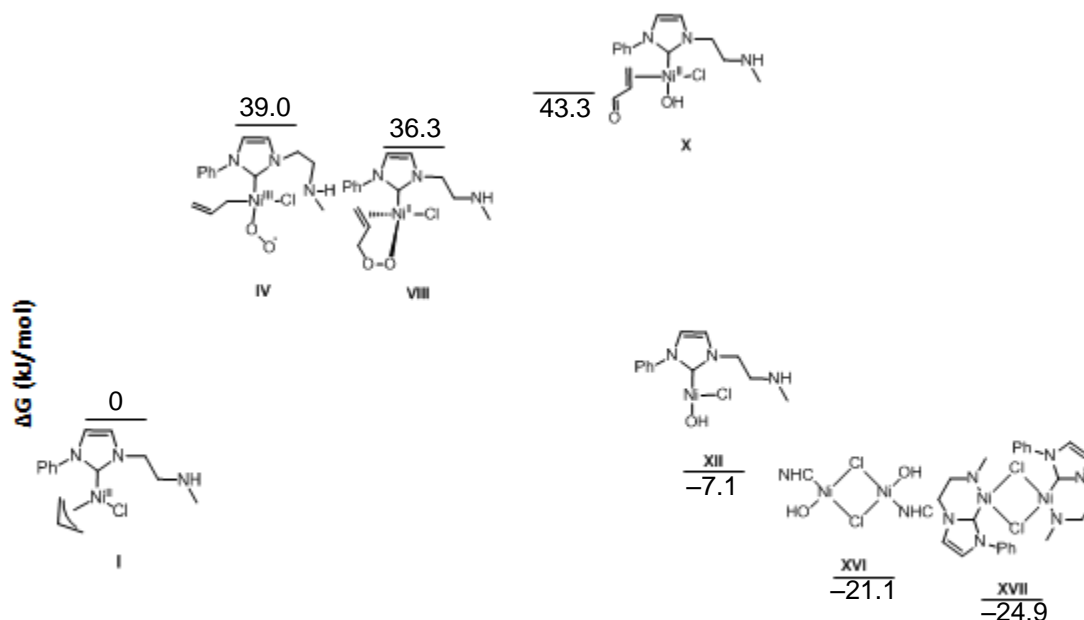


Figure 5.16: Proposed reaction pathway for the oxidation of **4** based on DFT calculated  $\Delta G$  values.

## 5.2 Time-Dependent DFT of Possible Oxidation Intermediates

Time dependent DFT (TD-DFT) analysis was used to aid in the assignment of reaction intermediates by calculating the theoretical UV-vis spectra of the possible species. Due to the number of structures analyzed, only the most pertinent structures will be discussed, and the complete data set can be found in the Appendix (Appendix 8.3-8.5).

The optimized structures obtained from Section 5.1 were used for the TD-DFT calculations, and the pertinent intermediates studied are shown below (Figure 5.17). The first 40 excited states were calculated, and the resulting simulated UV-vis spectrum was normalized. The normalization factor was determined by comparing the experimental and calculated UV-vis spectrum for complex **4** and multiplying or dividing by a factor to set the most intense band to 1. All of the subsequent spectra were normalized by the same factors. Based on the wavelength and oscillator strengths of the simulated spectrum compared to the experimental spectrum, the structure was concluded to be either a possible structure or not.

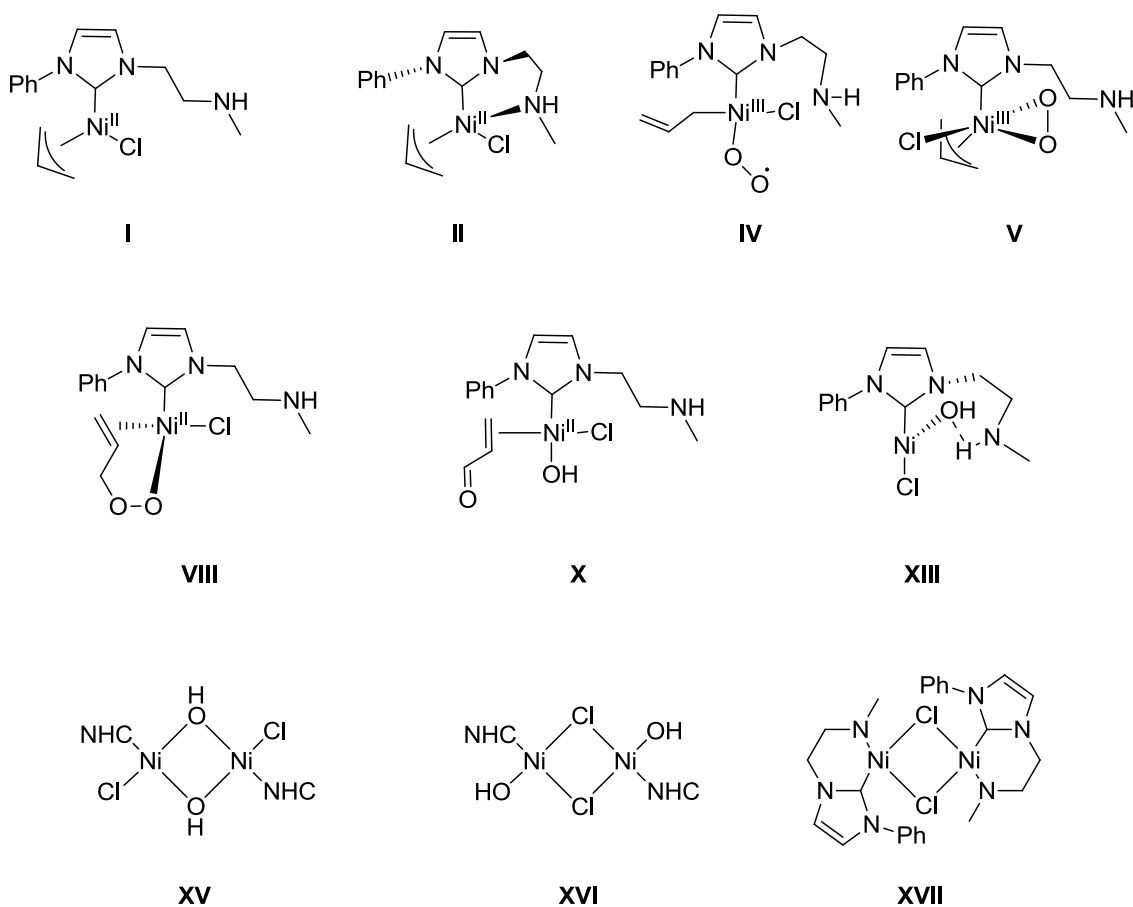


Figure 5.17: Structures chosen from Section 5.1 to be studied by TD-DFT methods.

From the experimental UV-vis analysis of Ni(allyl) complex **4**, there were two unique spectra obtained; one at 20 °C, and another at -65 °C. This change in the UV-vis spectrum was thought to occur from the fluxional nature of the complex, as observed in the room temperature <sup>1</sup>H NMR spectrum.<sup>54</sup> In previous studies, the static regime of **4** was not reached until -70 °C with an iodo-substituted complex.<sup>54</sup> This static complex was found to contain an η<sup>3</sup> allyl ligand, and from the crystal structure of **4**, the NHC was found to be in a κ<sup>1</sup>-C binding mode.<sup>54</sup> As a result, the TD-DFT spectra of conformers **I** and **II** were compared to the UV-vis spectrum of **4** obtained at -65 °C as it was more likely to resemble a single species. Structure **I** was considered as its structure is known, and it was the lowest energy conformer of **4** that was modelled in Section 5.1. Structure **II** was considered as well, as it was energetically accessible at this temperature regime

(Section 5.1), and also because the amine coordination mode has yet to be determined at this low temperature.

At  $-65\text{ }^{\circ}\text{C}$  the observed  $\lambda_{\text{max}}$  of **4** is 380 nm. From the simulated data of **I** and **II**, the simulated spectra are relatively similar, with a simulated excitation at  $\sim 420$  nm (Figure 5.18). This observation indicates that the TD-DFT simulation accurately gave a transition in the visible region. When these simulated traces are compared to the experimental spectrum of **4** at  $-65\text{ }^{\circ}\text{C}$ , there is not a great fit between the simulated and experimental spectra. This is likely due to a systematic error that is common in TD-DFT simulations.

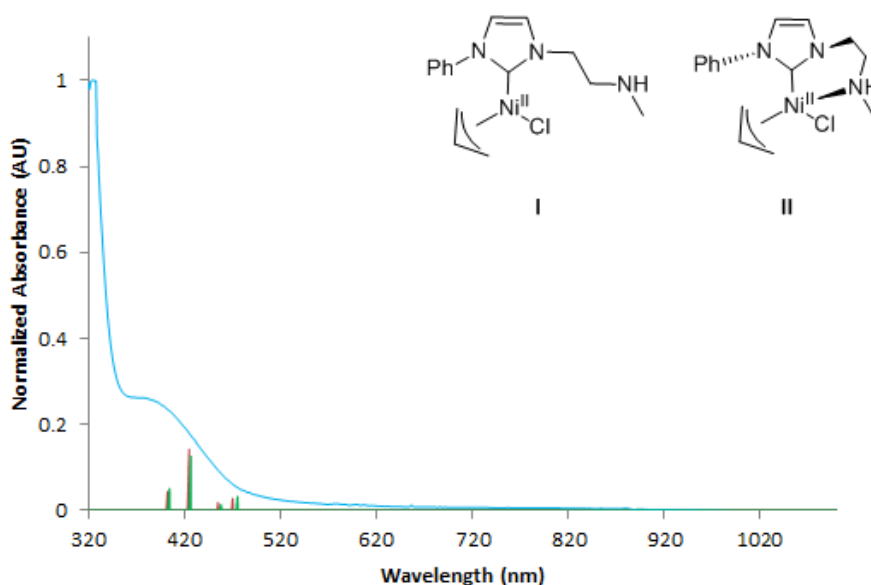


Figure 5.18: UV-Vis traces of **4** at  $-65\text{ }^{\circ}\text{C}$  (blue), TD-DFT simulated trace of **I** (red), and TD-DFT simulated trace of **II** (green).

From the proposed structures for **Int. 1**, there are three structures of interest; **IV**, **V**, and **VIII**. The end-on superoxo structure **IV** was considered here as it has been previously suggested by Sigman, and was energetically feasible according to the DFT calculations.<sup>49-50</sup> The side-on peroxo structure **V** was considered as there is literature precedence for side-on peroxo interactions with  $\text{Ni}^{\text{III}}$ .<sup>34, 47</sup> Lastly, the metallocycle structure **VIII** was considered as it would match the reactivity results of **Int. 1** (HAT,  $\text{N}_2$  sparging) from Section 3.3. The tetrahedral conformer of propenal-bound species **X** could

be a possible structure for **Int. 1**, although an optimized geometry was not obtained, and prevented the subsequent TD-DFT analysis.

The obtained UV-vis spectrum of **Int. 1** at  $-78\text{ }^{\circ}\text{C}$  has a shoulder at  $\sim 360\text{ nm}$ , and weak absorbance bands throughout the rest of the visible region. From the simulated spectrum of **IV**, there are simulated excitations within the 320-520 nm region that show a decrease in the oscillator strength as the wavelength increases (Figure 5.19). The simulated spectrum also displays a strong absorbance at  $\sim 710\text{ nm}$ . The simulated spectrum of **IV** matches well to the obtained spectrum of **Int. 1** at  $-78\text{ }^{\circ}\text{C}$  between the 320-520 nm range, as the absorbance becomes weaker as the wavelength increases in both spectra. However, the simulated UV-vis spectrum shows a strong absorbance at  $\sim 710\text{ nm}$  that was not observed in the UV-vis spectrum of **Int. 1**. Overall, the end-on superoxo structure **IV** is not a good fit for **Int. 1**, and is unlikely to be the observed structure.

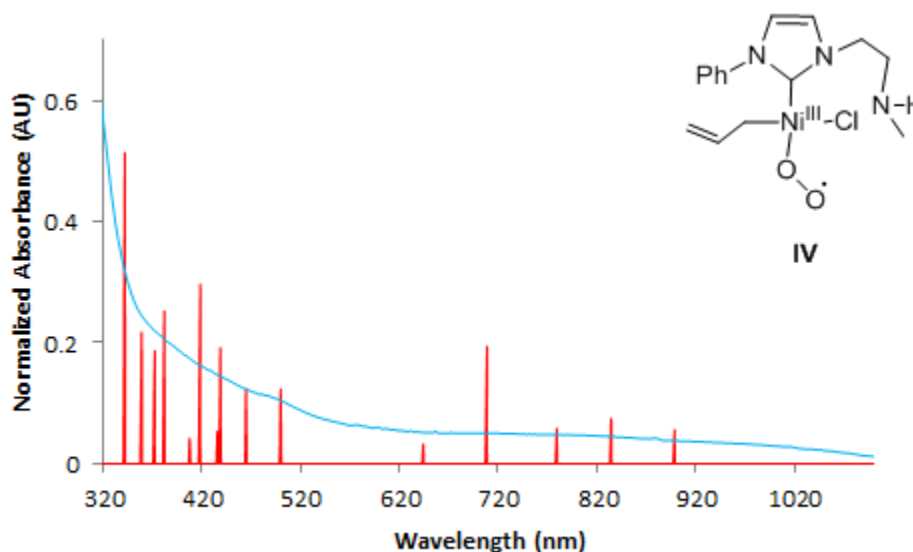


Figure 5.19: UV-vis spectrum of **Int. 1**  $-78\text{ }^{\circ}\text{C}$  (blue) and TD-DFT simulation of end-on superoxo structure **IV** (red).

Next, **V** was studied, and the simulated TD-DFT spectrum shows a pattern of absorbance bands between 320 nm and 520 nm that decrease in absorbance strength as the wavelength increases. When **V** was compared to the experimental UV-vis spectrum of **Int. 1**, the 320-520 nm region could correlate, as both spectra exhibit a decrease in

absorbance with an increase in wavelength between 320 nm and 520 nm (Figure 5.20). However, the simulated spectrum does not contain a calculated absorbance band at ~720 nm which was observed as a minor band in the experimental spectrum.

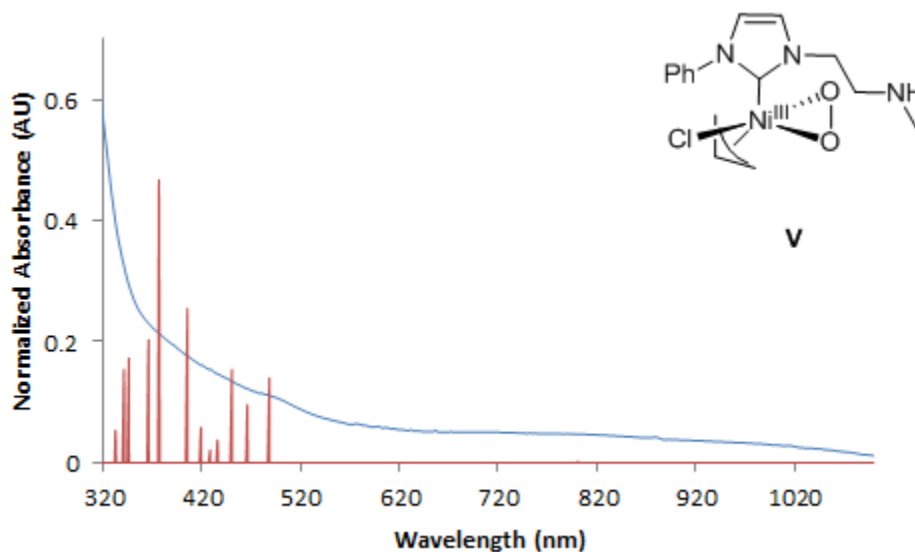


Figure 5.20: UV-vis spectrum of **Int. 1**  $-78^{\circ}\text{C}$  (blue) and TD-DFT simulation of side-on superoxo **V** (red).

Lastly, the metallocycle **VIII** was considered as it was energetically the most stable intermediate structure proposed by DFT, and would be unreactive to  $\text{N}_2$  sparging and HAT agents, which was consistent with the experimental results from Section 4.3. The simulated TD-DFT spectrum shows no absorbance bands around 720 nm, and little correlation to the experimental spectrum between 320 and 520 nm (Figure 5.21).

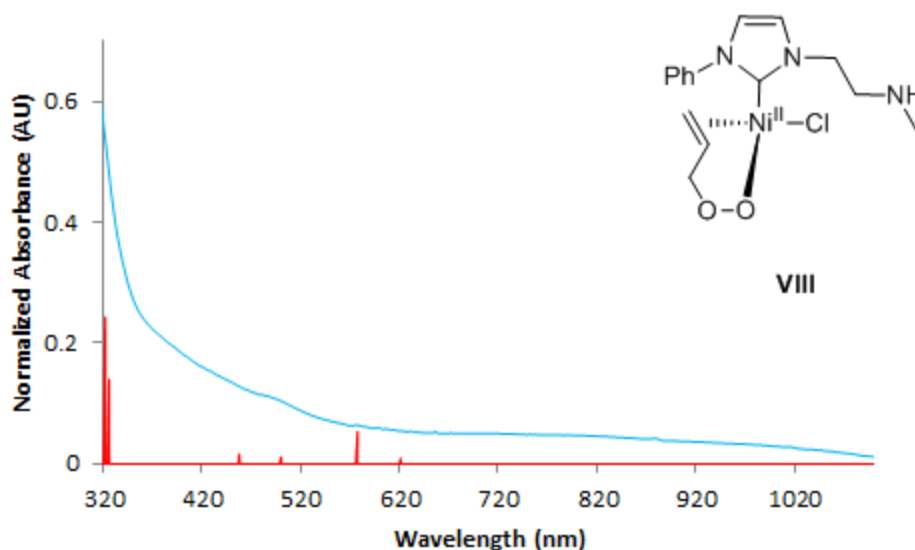


Figure 5.21: UV-vis spectrum of **Int. 1** at  $-78$  °C (blue) and TD-DFT simulation of metallocycle **VIII** (red).

From the TD-DFT analysis of the proposed structures for **Int. 1**, there was no conclusive structure that was determined between **V** and **VIII**. From the simulated traces, **IV** was a poor match, as it shows a strong absorbance band at 710 nm that is only a minor band in the experimental spectrum. Based on this result and the reactivity studies from Section 4.3, the end-on superoxo **IV** was not considered as an option for **Int. 1**.

Next, **Int. 2** was probed by TD-DFT analysis. From the low temperature  $^1\text{H}$  NMR analysis, it was known that propenal has formed, indicating that the reaction has proceeded through the superoxo structures. In the experimental spectrum of **Int. 2** at  $-65$  °C, there are absorbance bands observed between 390 and 500 nm, with a weak absorbance band observed at  $\sim 790$  nm. Structures **XI** and **XII** were simulated by TD-DFT analysis, but had very poor fitting between the simulated and experimental spectrum (Appendix 8.4 and 8.5, respectively).

Structure **X** was first considered, as it was the first intermediate structure that could be formed after the superoxo structures if Sigman's reaction pathway is followed (Scheme 4.1).<sup>49</sup> The simulated UV-vis spectrum of **X** contains absorbance bands between 390 nm and 500 nm, and a very weak band at  $\sim 680$  nm. When the simulated spectrum of **X** was

stacked with the obtained  $-65\text{ }^{\circ}\text{C}$  spectrum, there was a good fit in the 390-500 nm range (Figure 5.22). However, there are no minor absorbance bands simulated in the 790 nm range.

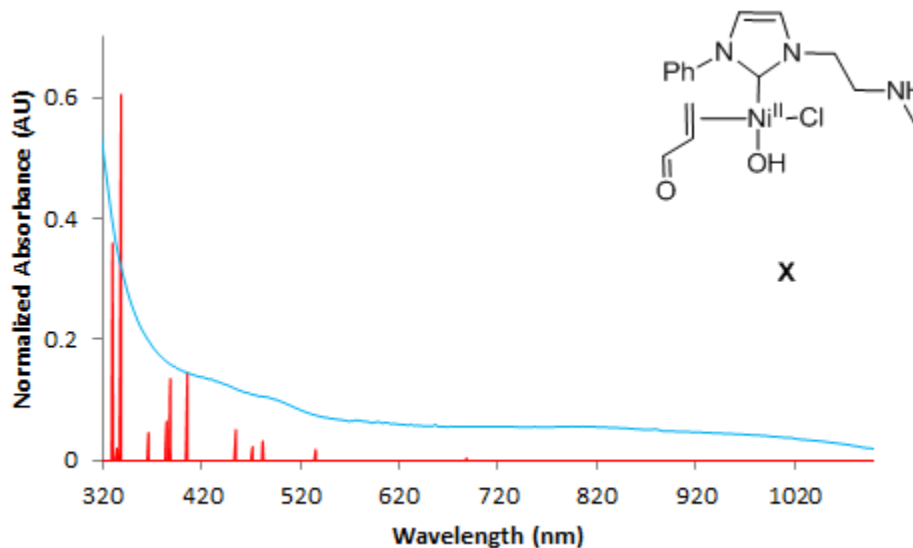


Figure 5.22: UV-Vis trace of **Int. 2** at  $-65\text{ }^{\circ}\text{C}$  (blue) and TD-DFT simulation of structure **X** (red).

One of the other proposed intermediate structures for **Int. 2** was structure **XIII** that has a hydrogen bond to the hydroxo ligand, as it was an energetically accessible intermediate structure by DFT analysis. From the TD-DFT simulated UV-vis spectrum of **XIII**, there was an absorbance band at  $\sim 770\text{ nm}$ , and no absorbance bands simulated between 420 nm and 520 nm. This simulated band at 770 nm could correlate to the absorbance band observed at  $\sim 810\text{ nm}$  for **Int. 2** (Figure 5.23). However, there are no absorbance bands observed in the 420-520 nm region in the TD-DFT simulated spectrum of **XIII**, whereas the spectrum for **Int. 2** still shows absorbance bands within that region.



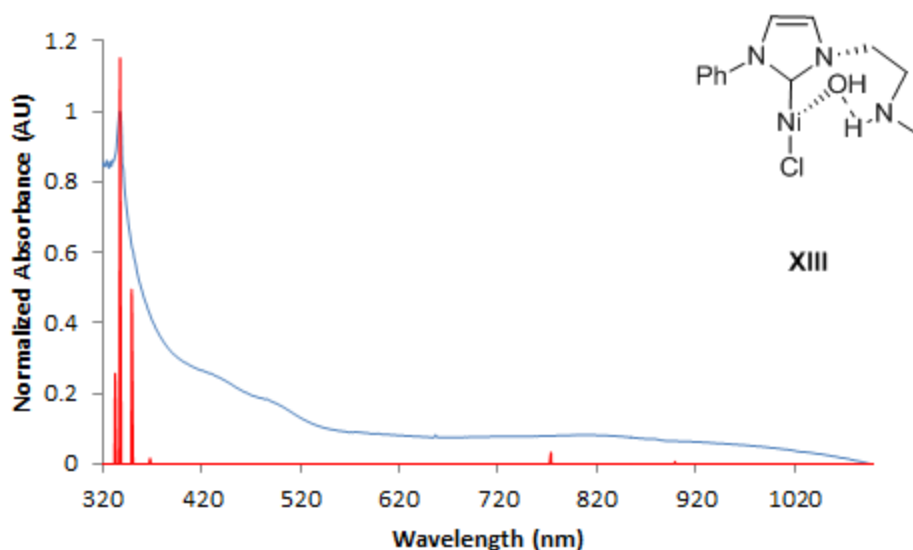


Figure 5.23: UV-vis spectrum of **Int. 2** at  $-65\text{ }^{\circ}\text{C}$  (blue) and TD-DFT simulation of **XIII** (red).

Interestingly, when the two simulated TD-DFT spectra for **X** and **XIII** are overlaid, the two simulated data sets match well to the experimentally observed spectrum. Structure **X** has simulated absorbance bands between 320 and 520 nm, while **XIII** has a simulated absorbance at  $\sim 770$  nm, which could correlate to the observed absorbance band at  $\sim 810$  nm. From this observation, it could be possible that the two species are formed alongside each other (Figure 5.24). From Chapter 4, it was found that **Int. 2** was not formed quantitatively, and may contain decomposition/side-products.

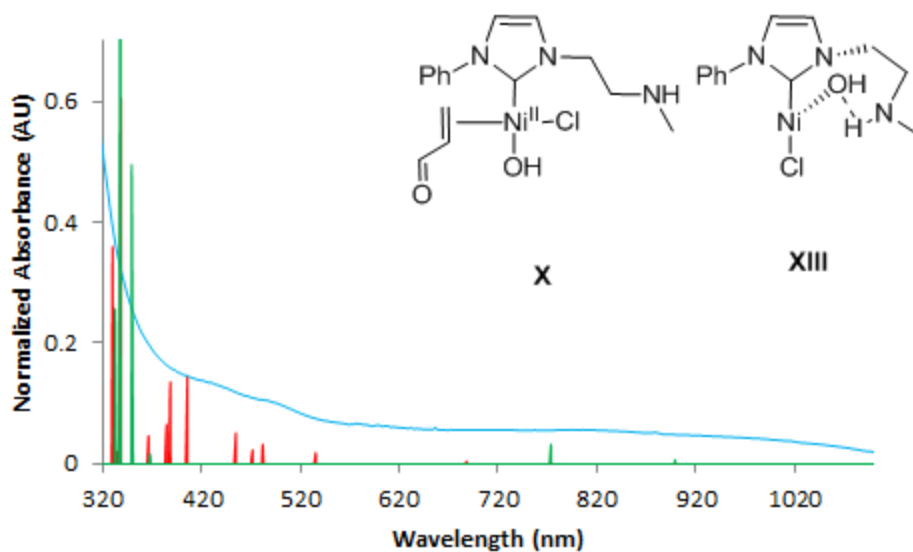


Figure 5.24: UV-vis spectrum of **Int. 2** at  $-65\text{ }^{\circ}\text{C}$  (blue), TD-DFT simulation of **X** (red), and TD-DFT simulation of **XIII** (green).

From the DFT analysis, the most favorable dimer species to form was **XVII**, which shows strong absorbance bands between 380 nm and 400 nm, and a medium absorbance band at 760 nm. When the UV-vis spectrum of **Int. 2** was compared to the TD-DFT spectrum of **XVII**, there was little correlation between the two spectra as the peak positions and intensities do not match between the two (Figure 5.25).

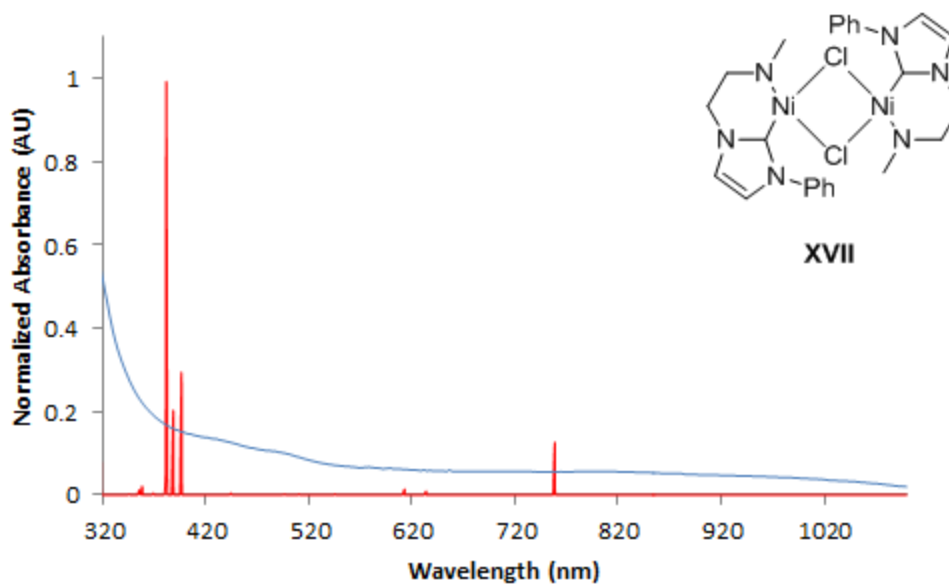


Figure 5.25: UV-vis spectrum of **Int. 2** at  $-65\text{ }^{\circ}\text{C}$  (blue) and TD-DFT spectrum of **XVII** (red).

The next most energetically favorable dimer species was **XVI** (Figure 5.12). The TD-DFT simulated spectrum of **XVI** shows an absorbance band at  $\sim 500\text{ nm}$ . When the simulated spectrum of **XVI** was compared to the experimental spectrum obtained at  $-65\text{ }^{\circ}\text{C}$ , the bands observed at  $\sim 500\text{ nm}$  are in agreement with one another (Figure 5.26). However, there are bands observed at  $\sim 420\text{ nm}$  and  $\sim 770\text{ nm}$  in the experimental UV-vis spectrum that were not simulated in the TD-DFT spectrum **XVI**.

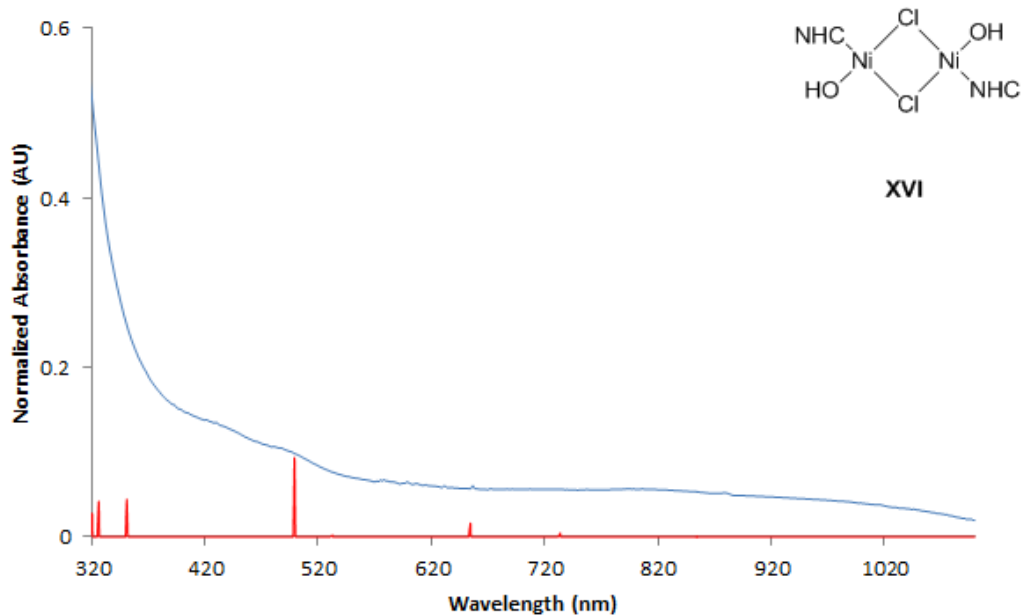


Figure 5.26: UV-vis spectrum of **Int. 2** at  $-65\text{ }^{\circ}\text{C}$  (blue) and TD-DFT spectrum of dimer species **XVI** (red).

The last dimer structure that was simulated by TD-DFT was **XV**, which was analogous to the Ni- $\mu\text{OH}$  structure proposed by Sigman (Figure 5.11).<sup>49</sup> From the simulated TD-DFT spectrum of **XV**, there was an absorbance band at  $\sim 500\text{ nm}$ , which matches the literature reports of other Ni- $\mu\text{OH}$  dimers.<sup>49-50</sup> When the simulated UV-vis spectrum of **XV** was compared to the UV-vis spectrum obtained at  $-65\text{ }^{\circ}\text{C}$ , the bands at  $500\text{ nm}$  match well between the two spectra (Figure 5.27). However, once again there are no absorbance bands simulated at  $\sim 770\text{ nm}$  or  $\sim 420\text{ nm}$  which were observed experimentally.

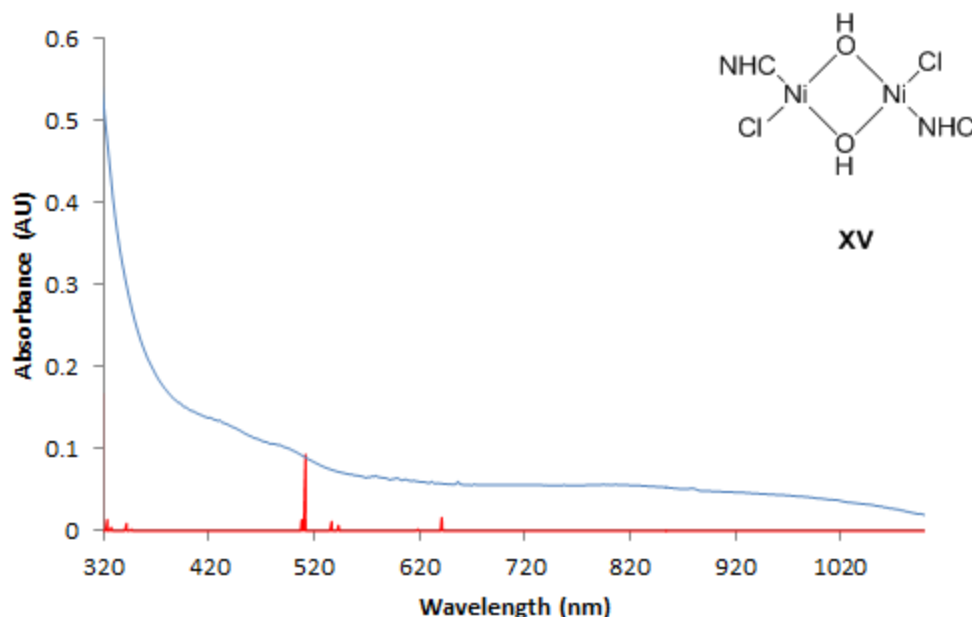


Figure 5.27: Obtained UV-vis spectrum of **Int. 2** at  $-65\text{ }^{\circ}\text{C}$  (blue) and the TD-DFT simulated spectrum of **XV** (red).

From the three dimer structures studied, **XV** and **XVI** match the experimental absorbance band at  $\sim 500\text{ nm}$ . However, the three dimer structures do not show the related absorbance bands at  $\sim 770\text{ nm}$  or  $\sim 420\text{ nm}$ . Additionally, **XVII** does not correlate to the experimentally observed spectrum. This observation indicates that the dimer species may be present at  $-65\text{ }^{\circ}\text{C}$ , but are not the major species observed. From the  $^1\text{H}$  NMR spectrum and the UV-vis spectra, it is unknown if there was one or several nickel species observed at  $-30\text{ }^{\circ}\text{C}$ . As a result, the TD-DFT analysis was not applied to the  $-30\text{ }^{\circ}\text{C}$  data.

From the TD-DFT analysis of **Int. 1**, there was no conclusive evidence to determine the structure of **Int. 1** between **IV**, **V**, and **VIII**. From the TD-DFT analysis and the experimental results, it was unlikely that **IV** was the observed structure at **Int. 1**. From the TD-DFT analysis of **Int. 2**, neither the TD-DFT simulated spectrum of **X** nor **XIII** correlate exactly to the experimental spectrum obtained at  $-65\text{ }^{\circ}\text{C}$ . However, when the two simulated spectra are overlaid, it shows stronger agreement to the experimentally observed spectrum. This means that **Int. 2** may be a mixture of **X** and **XIII**. Lastly, the dimeric structures **XV**, **XVI**, and **XVII** were studied as possible structures for **Int. 2** at  $-65\text{ }^{\circ}\text{C}$ . Structure **XVII** was energetically favorable by DFT and was found to have a poor

fit to the experimental UV-vis spectrum. Structures **XV** and **XVI** did display some slight correlation at ~500 nm, but did not have simulated absorbance bands at ~770 nm or ~420 nm. It is unlikely that the dimeric species **XVII** was formed at -65 °C, although **XV** and **XVI** may be formed, also. The final decomposition spectrum was not compared to anything, as it is believed to be a mixture of several species, making identification of a single species challenging.

## 6 Conclusions and Future Work

### 6.1 General Conclusions

In this thesis, three main areas of interest were probed. The first two were the optimal oxidation conditions of **5a** and **5b** (Chapter 2) and the optimal catalytic oxidation conditions for **4** (Chapter 2). Upon exposure to O<sub>2</sub>, 5 mM samples of **5a** formed **CA** and **PVK** in ~1:1 ratios in moderate to good yields as determined by GC-FID; and are consistent with samples at a higher concentration. From these studies, MeCN gave the highest conversion (~90%), while pyridine showed increased selectivity for **CA**, presumably through coordination to the intermediate structures. The attempted catalysis of allylbenzene with **4** as the catalyst was attempted at high and low temperatures and with additional base in both MeCN and pyridine, with no turnover observed by GC-FID. This reaction was also conducted neat and in DCM at -50 °C, with no turnover observed by GC-FID. The substrate was changed to cinnamyl pinacolborane with **4** as the catalyst, as the byproduct B-O bond is stronger than the byproduct O-H bond, and provide a better thermodynamic driving force. However, there was no turnover observed by <sup>1</sup>H NMR spectroscopy. From these experiments, it was found that **4** was non-catalytic under the reported conditions. The most likely reason that **4** is non-catalytic is due to decomposition of the reactive intermediates. Whether this was through dimerization or deprotonation of the NHC ligand is currently unknown.

The third area was the investigation of the decomposition (Chapter 3) and intermediate structures (Chapters 4 and 5) formed upon oxidation of **4**. First, the room temperature decomposition products of **4** were studied, and three products were observed; H[NHC]<sup>+</sup> (17% yield), NiCl<sub>2</sub>(NHC)<sub>2</sub> (~10% yield), and NiCl<sub>2</sub>(py)<sub>4</sub>. From these studies, the decomposition species observed do not account for all of the material present, meaning that some of the decomposition species have yet to be identified. Previous work from a related non-bifunctional system has shown that the major decomposition species formed is a Ni<sup>II</sup>-μOH dimer.<sup>49</sup> From the experiments reported above, the decomposition products observed are dramatically different, indicating that the choice of the NHC ligand plays a crucial role in the observed reactivity.

The synthesis of an analogue of  $\text{Ni}^{\text{III}}\text{-O}_2$  was attempted by reacting **5a** with  $\text{NaN}_3$  in  $\text{C}_6\text{H}_6$ , although the reaction did not proceed due to the low solubility of  $\text{NaN}_3$  in  $\text{C}_6\text{H}_6$ . The solvent was changed to MeCN, but the reaction did not proceed cleanly and gave poor evidence for the formation of a Ni- $\text{N}_3$  species by  $^1\text{H}$  NMR spectroscopy and MALDI-MS. As a result of poor experimental data and more fruitful research avenues, this section of the project was not investigated further.

The oxidation intermediates and mechanism for **4** were probed through both experimental (Chapter 4) and computational methods (Chapter 5). Two key intermediates were observed and trapped: **Int. 1** at  $-78\text{ }^\circ\text{C}$ , and **Int. 2** at  $-65\text{ }^\circ\text{C}$ . Neither of the intermediates showed thermal reversibility. **Int. 1** was not reversible when sparged with  $\text{N}_2$ , and was unreactive to the HAT agent DPH. **Int. 1** was found to be a paramagnetic species, although the obtained  $\mu_{\text{B}}$  value did not correlate to the predicted structures. From the thermodynamic analysis, there were three intermediates of interest for **Int. 1**; end-on superoxo **IV**, side-on superoxo **V**, and tetrahedral metallocycle **VIII**. These three intermediates had similar energy values, making identification by thermodynamic stability difficult. From the TD-DFT analysis of these three structures, **IV** was unlikely to be observed as its simulated spectrum fits poorly. The TD-DFT analysis of structures **V** and **VIII** do not match the experimental spectrum well, but are still possibilities that could be observed. From the experimental and computational data presented, **Int. 1** was proposed to be the tetrahedral metallocycle **VIII**, as it would be non-reactive to HAT agents and  $\text{N}_2$  sparging, and was the most stable structure of the three by the thermodynamic analysis. **VIII** was also tetrahedral, which would lead to a paramagnetic spectrum, which was inferred from the  $^1\text{H}$  NMR analysis. The possible presence of this intermediate could indicate that a new mechanism is occurring that has been previously unidentified.

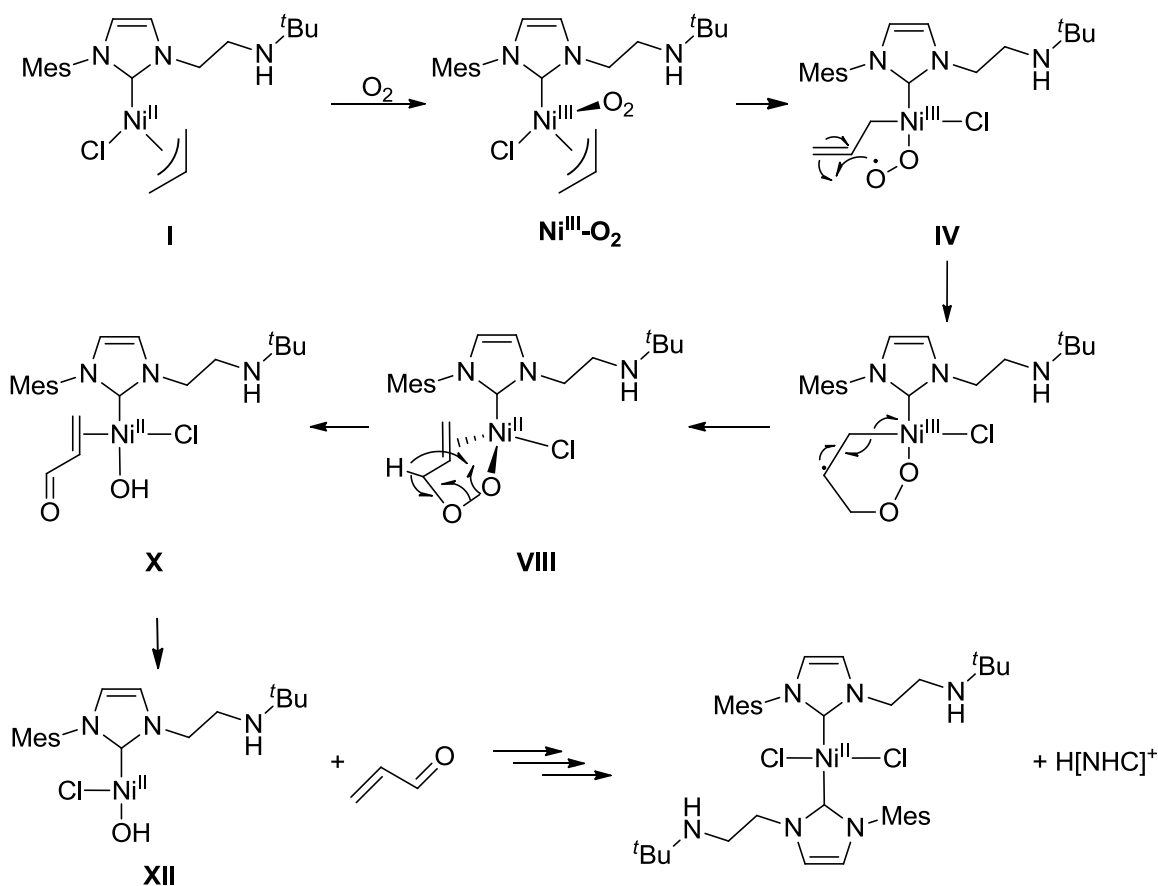
**Int. 2** was reactive to  $\text{py}\cdot\text{HCl}$ , although whether the reactivity is due to a  $\text{Ni}^{\text{II}}\text{-OH}$  species or a possible amido is currently unknown. **Int. 2** also contained free propenal, indicating that **Int. 2** was not a Ni- $\text{O}_2$  adduct. It was found that **Int. 2** was not generated



quantitatively and other impurities or side-products are present, as the Evans method shift was observed throughout the reaction.  $\text{H}[\text{NHC}]^+$  was observed as a decomposition product in the final room temperature  $^1\text{H}$  NMR spectrum, and potentially  $\text{NiCl}_2(\text{NHC})_2$ . A characteristic shift for a  $\text{Ni}^{\text{II}}-\mu\text{OH}$  dimer was not observed during the reaction. As **Int. 2** is formed alongside other decomposition species, its identity was difficult to determine by computational methods. From the thermodynamic analysis, **X**, **XI**, **XII**, and **XIII** are energetically accessible  $\text{Ni}^{\text{II}}-\text{OH}$  monomers. From the dimeric structures **XV**, **XVI**, and **XVII**, structure **XVII** was the most energetically stable species. Structure **XV** (the analogous  $\text{Ni}^{\text{II}}-\mu\text{OH}$  dimer to Sigman *et al.*) was  $\sim 50 \text{ kJmol}^{-1}$  higher in energy than the most stable conformer of **I**, making it an unlikely intermediate to be formed. From the TD-DFT analysis, structures **XI** and **XII** showed poor agreement to the experimentally observed spectrum. Individually, **X** and **XIII** did not agree well to the experimental spectrum, but when the two are overlaid, there was much better agreement to the experimental spectrum for **Int. 2**. All three dimers matched poorly to the experimentally observed UV-vis spectrum. From the results, **Int. 2** cannot be conclusively determined as it was likely a mixture of species, although the TD-DFT analysis and experimental results point to either **XVI** or **XVII** being possible candidates.

To explain the observed results, an alternate reaction mechanism was proposed (Scheme 6.1). First, **I** binds to  $\text{O}_2$  and presumably forms a square pyramidal  $\text{Ni}^{\text{III}}-\text{O}_2$  intermediate.<sup>50</sup> Next, the allyl alkene homolytically cleaves and forms a bond with the oxygen radical (**IV**). This leaves a radical carbon atom in the framework of the metallocycle. The Ni-C bond homolytically cleaves and forms a new C-C double bond with the framework radical and reduces the  $\text{Ni}^{\text{III}}$  to  $\text{Ni}^{\text{II}}$ . This leads to the tetrahedral structure **VIII**. Next, **VIII** performs a radical C-H abstraction, leading to the formation of **XII** and the organic propenal product. Whether this transformation occurs over one or two steps is currently unknown. The propenal then dissociates, forming a monomeric  $\text{Ni}^{\text{II}}-\text{OH}$  structure. After this, the reactivity is unknown, but decomposes to  $\text{NiCl}_2(\text{NHC})_2$  and  $\text{H}[\text{NHC}]^+$ . This mechanism differs dramatically from previous systems, as the final observed nickel product was a  $\text{Ni}-\mu\text{OH}$  dimer, whereas there was no substantial evidence of a  $\text{Ni}-\mu\text{OH}$  dimer observed in our system, and C-H activation step is different as well.<sup>49</sup>

From the observations above, the inclusion of a pendent hydrogen bond donor group within the NHC ligand dramatically changes the decomposition products and proposed reaction pathways. As of right now, the identity and reactivity of the observed intermediates are still being probed. Additionally, there appears to be little evidence of a hydrogen bonding interaction even being present during the oxidation reaction. From the experimental results, the pendent hydrogen bonding group does not appear to be necessary, and may even be promoting unwanted side reactivity through protonation of the hydroxo ligand. This side reactivity may be preventing the  $\text{Ni}^{\text{II}}\text{-OH}$  from performing the desired chemistry.



Scheme 6.1: Proposed alternate oxidation pathway of 4.

## 6.2 Future Work

Future work on this project will focus on two areas; 1) complete characterization of the intermediate structures and 2) synthesis of bi- or tridentate NHC ligands to better stabilize the proposed  $\text{Ni}^{\text{II}}\text{-OH}$  intermediate.

To accomplish the first goal a number of experiments will assist in the identification of **Int. 1**. **Int. 1** will be initially reacted with PPh<sub>3</sub> and if there is a bound superoxo, then an oxygen atom transfer reaction should occur and form the corresponding O=PPh<sub>3</sub> (Figure 6.2).<sup>46-47</sup> **Int. 1** will also be titrated with py•HCl to determine if a basic Ni-OH or amido group (M-NRR') is present. Next, **Int. 1** will be studied by EPR spectroscopy so as to more accurately determine the number of unpaired electrons. From the crystal field d-orbital splitting interactions with superoxo, all of the samples had integer spin states. While EPR spectroscopy does not work well for integer spin states, the confirmation of an integer spin state can at least shed some insight as to the structure of **Int. 1**.<sup>78</sup> Another method that can be used to probe the paramagnetic properties of **Int. 1** is SQUID. The SQUID measurements will more accurately determine the effective magnetic moment of **Int. 1**, and can once again provide insight into the structure based on the magnetic properties. The geometry and oxidation of the nickel center in **Int. 1** can also be determined by extended X-ray absorption fine structure (EXAFS) methods.<sup>79-80</sup> Of interest will be the positions of the oxygen and nitrogen atoms through the different intermediate structures to better determine the intermediate structures. Lastly, further computational analysis can be performed using different functionals while retaining the same basis sets to ensure computation accuracy. This can provide further insight into the proposed reaction pathway and, based on the calculated energies, potentially eliminate certain intermediates as possible structures.

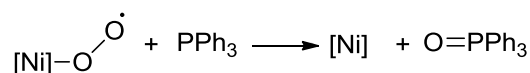


Figure 6.1: Proposed reaction of a Ni<sup>III</sup>-O<sub>2</sub> with PPh<sub>3</sub> to form OPPh<sub>3</sub>.

To aid in identifying **Int. 2**, the titration with py•HCl will be repeated, but with 0.1 molar equivalent additions, and ending the reaction after 0.6 molar equivalents have been added. The resulting sample will be tested for its thermal stability, and if it is stable, NMR spectroscopy will be conducted. To determine if the reactivity observed upon addition of py•HCl to **Int. 2** was from a Ni<sup>II</sup>-OH moiety or an amido moiety, the acid titration experiment will be repeated using different acids of varying strengths. Potential acids to use are acetic acid (pK<sub>aMeCN</sub> = 22.3), cyanoacetic acid (pK<sub>aMeCN</sub> = 18.0), malonic

acid ( $pK_{a}^{\text{MeCN}} = 15.3$ ), and dichloroacetic acid ( $pK_{a}^{\text{MeCN}} = 13.2$ ).<sup>63</sup> This range of  $pK_a$  values will aid in determining whether the observed reactivity is for protonation of a  $\text{Ni}^{\text{II}}\text{-OH}$  or an amido group. While it is unlikely that **Int. 2** contains a superoxo, the titration with DPH will be performed to confirm this.

To address this challenge, NHC ligands that lack a pendent hydrogen bonding group but contain a hemilabile group will be used instead. The hemilabile group will have the same function as the pendent amine of the complexes described above, which is to stabilize the proposed low coordinate intermediate structures formed. This essentially forms a bi- or tridentate ligand, depending on the number of atoms that could coordinate to the metal center. Bi- or tridentate ligands have been previously shown to stabilize  $\text{Ni}^{\text{II}}\text{-OH}$  monomers.<sup>51</sup> By using a bi- or tridentate ligand with a hemilabile ligand, it could be possible to form the proposed  $\text{Ni}^{\text{II}}\text{-OH}$  as a stable species to allow for full characterization. Two target ligands have been determined (Figure 6.3). These ligands have been previously reported, and their syntheses are known.<sup>81-82</sup> The pyridyl arm of the ligands is proposed to be a hemilabile ligand, and would allow for coordination and stabilization if the complex adopted a low coordinate state. Once the resulting metal complexes have been characterized and determined to be  $\text{O}_2$  reactive, the intermediate structures of these new complexes will be further studied using methods similar to those discussed in the report. If the proposed  $\text{Ni}^{\text{II}}\text{-OH}$  is formed, it is proposed that these ligands will stabilize the hydroxo and allow for full characterization. After the characterization, the catalytic activity of the  $\text{Ni}^{\text{II}}\text{-OH}$  will be studied using similar reactions as those mentioned in Chapter 2. The  $pK_{a}^{\text{DCM}}$  of the  $\text{Ni}^{\text{II}}\text{-OH}$  moiety will also be determined by subjecting the sample to a variety of acids and monitoring the reaction through UV-vis spectroscopy.

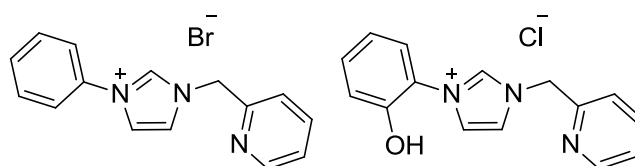


Figure 6.2: Proposed bi- and tridentate ligands to be used for the stabilization of **Int. 2**.

## 7 Experimental

Unless otherwise stated, all procedures were carried out under an inert nitrogen atmosphere using standard glovebox or Schlenk techniques. Glassware was placed in a 150 °C oven for three hours prior to use and cooled either under vacuum or by flowing inert gas into the glassware. Dried solvents, with the exception of MeCN, were obtained from an Innovative Technologies 400-5 Solvent Purification System and were stored over 4 Å molecular sieves. Dry MeCN was obtained from an Innovative Technologies 400-5 Solvent Purification System and stored without further modifications. CDCl<sub>3</sub> and C<sub>6</sub>D<sub>6</sub> were purchased from Cambridge Isotope Laboratories and were purged with nitrogen and stored over 4Å sieves before use. Ampoules of MeCN-*d*<sub>3</sub> were obtained from Cambridge Isotope Laboratories and, as indicated, either used as received or stored over 3 Å sieves for 24 hours prior to use. DCM-*d*<sub>2</sub>, and pyridine-*d*<sub>5</sub> were obtained from Cambridge Isotope Laboratories and, as indicated, either used as received or stored over 4Å molecular sieves for 24 hours prior to use. 2-(*tert*-Butylamino)ethanol (99%), thionyl chloride (99%), sodium hydroxide (99%), potassium bis(trimethylsilyl)amide (95%), allyl chloride (98%), cinnamyl chloride (95%), formaldehyde (37% w/w in H<sub>2</sub>O), glyoxal (40% w/w in H<sub>2</sub>O), glacial acetic acid (99%), ammonium acetate (98%), nickel<sup>II</sup>(acetylacetonate) (95%), 1,5 cyclooctadiene (99%), 2,4,6-trimethyl aniline (98%), diisobutyl aluminium hydride (1.0 M in THF), *N,N*-diisopropyl ethyl amine (99%), cinnamyl acetate (99%), bis(pinacolato)diboron (98%), and pyridinium chloride (98%) were purchased from either Alfa Aesar or Sigma Aldrich and used without further purification. 1,2 diphenyl hydrazine was purchased from Oakwood Chemicals and washed with petroleum ether until the washes were pale yellow. Ni(cod)<sub>2</sub>,<sup>83</sup> *N*-mesitylimidazole,<sup>84</sup> 2-(*tert*-butylamino) ethyl chloride hydrochloride,<sup>84</sup> [HC{(Mes)N(CHCH)N(CH<sub>2</sub>CH<sub>2</sub>NH(<sup>*t*</sup>Bu))}]Cl•HCl,<sup>54</sup> [HC{(Mes)N(CHCH)N(CH<sub>2</sub>CH<sub>2</sub>NH(<sup>*t*</sup>Bu))}]Cl,<sup>54</sup> [C{(Mes)NH(CHCH)N(CH<sub>2</sub>CH<sub>2</sub>NH(<sup>*t*</sup>Bu))}],<sup>54</sup> cinnamyl pinacolborane,<sup>60</sup> **4**<sup>54</sup> and **5a**<sup>54</sup> were synthesized according to previous methods. **5b** was synthesized by a previous member of the Blacquiere group.<sup>54</sup> Dioxygen (99%) was purchased from Praxair and passed through a drying tube containing calcium sulphate and a cold ice trap to remove water prior to use. NMR spectra were acquired at the listed temperatures on a Varian

INOVA 600 MHz or Varian INOVA 400 MHz spectrometer.  $^1\text{H}$  NMR spectra were referenced using residual solvent signals to tetramethylsilane at 0 ppm. Oxidation reactions were analyzed using an Agilent 7890A GC-FID with an HP-5 column using tetradecane as an internal standard. Calibration curves and response factors for phenyl vinyl ketone (**PVK**) and cinnamaldehyde (**CA**) were used to quantify and they were determined by a previous member of the Blacquiere group.<sup>54</sup> MALDI-TOF mass spectra were collected using an AB Sciex 5800 TOF/TOF mass spectrometer using either pyrene or anthracene as the matrix in a 20:1 matrix:substrate molar ratio. Infrared spectra were collected on solid samples using a PerkinElmer UATR TWO FT-IR spectrometer. UV-Visible spectra were collected using an Agilent Technologies Cary 8454 UV-Visible spectrometer, fitted with a Unisoko CoolspeK UV USP-203-A cryostat for low temperature analyses. The crystal sample of **9** and **10** was mounted on a Mitegen polyimide micromount with a small amount of Paratone N oil. All X-ray measurements were made on a Bruker Kappa Axis Apex2 diffractometer at a temperature of 110 K. The unit cell dimensions were determined from a symmetry-constrained fit and compared to crystal structures in the Cambridge Crystallographic Database Center (CCDC).

### General Procedure for the Stoichiometric Oxidation of **5a**

In a vial, a stock solution of **5a** (120 mg, 0.241 mmol, 100 mM) was prepared in THF (2.415 mL). In a separate vial, a stock solution of the internal standard tetradecane (40 mg, 0.202 mmol, 100.81 mM) was prepared in THF (2.00 mL). To 12 GC vials (A-L), 50  $\mu\text{L}$  of the **5a** solution and 49.6  $\mu\text{L}$  of the tetradecane solution were dispensed. Vials A and B were set aside, while vials C-L had the solvent removed *in vacuo*. To vial A, 900.4  $\mu\text{L}$  of THF was added, and then the vial was capped. To vial G, 891.4  $\mu\text{L}$  of THF was added, and then the vial was capped. To the remainder of the vials (B-F, H-L), 1 mL of the necessary solvent (in order: DCM, acetone, MeCN, DMF, MeTHF, Toluene, DME, pyridine, dioxane, dioxane) was added to the residue, and then the vials were capped and removed from the glovebox. 9  $\mu\text{L}$  of degassed  $\text{H}_2\text{O}$  was added to vial G via a microliter syringe. Dry  $\text{O}_2$  was bubbled into the GC vials A-K for ~20 seconds through a stainless steel needle equipped with a bleed needle. The vials were left sealed under the  $\text{O}_2$

environment, and after 15 minutes, the vials were analyzed by GC-FID. Vial L was analyzed by GC-FID without the addition of O<sub>2</sub>.

### **Stoichiometric Oxidation of 5a in THF with LiHMDS**

In a vial, a stock solution of **5a** (42 mg, 0.084 mmol, 50 mM) was prepared in THF (1.7 mL). In a separate vial, a stock solution of the internal standard tetradecane (20 mg, 0.10 mmol, 100 mM) was prepared in THF (1 mL). In a third vial, a stock solution of LiHMDS (39 mg, 0.23 mmol, 110 mM) was prepared in THF (2.12 mL). To six GC vials (A-F), 200 µL of the **5a** solution and 100 µL of the tetradecane solution were dispensed. Two of the GC vials (A and B) were diluted to 1 mL of THF. 100 µL of the LiHMDS stock solution was added to the remaining four (C-F) GC vials. The GC vials were capped with a screw cap fitted with a PTFE septum and removed from the glovebox along with the LiHMDS stock solution. Dry O<sub>2</sub> was bubbled through a stainless steel needle for ~20 seconds into vials A-D, each equipped with a bleed needle. The vials were left sealed under the O<sub>2</sub> environment for 15 minutes, and analyzed by GC-FID. After vials A and B were initially analyzed, 100 µL of the LiHMDS was added to each and they were left to react for 15 minutes, after which they were once again analyzed by GC-FID.

### **General Procedure for the Stoichiometric Oxidation of 5a with PPh<sub>3</sub>**

In a vial, a stock solution of **5a** (11 mg, 0.022 mmol, 100 mM) was prepared in THF (221 µL). In a separate vial, a stock solution of the internal standard tetradecane (25 mg, 0.13 mmol, 100 mM) was prepared in THF (1.26 mL). A third stock solution of PPh<sub>3</sub> (116 mg, 0.442 mmol, 500 mM) was prepared in THF (884 µL). To two GC vials (A and B), 50 µL of the **5a** solution and the internal standard solution were dispensed. Vials A and B were then diluted with 900 µL THF, capped, and set aside. To two other GC vials (C and D), 50 µL of the **5a** solution and the internal standard solution were dispensed, and the solvent was removed *in vacuo* to afford a light brown residue. Vials C and D were then dissolved in 1 mL MeCN and capped, and all four vials (A-D) were removed from the glovebox. Dry O<sub>2</sub> was bubbled through a stainless steel needle into the vials for ~20 seconds with a bleed needle present. The vials were left sealed under the O<sub>2</sub> environment



for 15 minutes, and were then analyzed by GC-FID. After analysis by GC-FID, the vials were brought back into the glovebox and 100  $\mu\text{L}$  of the  $\text{PPh}_3$  solution was added via syringe. The vials were capped and swirled, and brought out of the glovebox. After 15 minutes, the solutions were analyzed again by GC-FID.

### **Representative Procedure for Attempted Catalytic Oxidation of Allylbenzene**

A stock solution of allylbenzene (54 mg, 0.46 mmol, 127 mM) was prepared in MeCN (3.7 mL), and 1.6 mL of the resulting solution was added to a 5 mL round bottom flask that was charged with 3 $\text{\AA}$  molecular sieves and a stir bar. A second stock solution containing **4** (5 mg, 0.01 mmol, 5 mM) in MeCN (2.5 mL) was prepared and 421  $\mu\text{L}$  of this solution was added to the round bottom flask. A third stock solution of the internal standard tetradecane (8 mg, 0.04 mmol, 11 mM) in MeCN (3.7 mL) was prepared and a 1.6 mL portion was added to the round bottom flask. The final concentrations are 100 mM allylbenzene, 10 mM tetradecane, 1 mol% **4**. The flask was sealed with a septum and secured with electrical tape before being removed from the glovebox. Dry  $\text{O}_2$  was bubbled through a stainless steel needle into the flask, which was equipped with a bleed needle, for ~45 seconds and the reaction was stirred at room temperature. Reaction aliquots (0.1 mL) were removed and diluted to a total volume of 1 mL with MeCN at 0.25, 1, 4, and 6 hours and analyzed by GC-FID. The yields of phenyl vinyl ketone and cinnamaldehyde were less than 1%, indicating that catalytic turnover did not occur. The reaction was repeated under similar conditions with pyridine as the solvent.

### **Attempted Catalysis of Allylbenzene with **4** at High and Low Temperatures**

The procedure follows the representative procedure as above, except that the reaction flask was immersed in a preheated oil bath set to 70  $^\circ\text{C}$  after  $\text{O}_2$  addition when MeCN was the solvent, and a 100  $^\circ\text{C}$  oil bath for pyridine. For low temperatures, the procedure follows the representative procedure as above for both MeCN and pyridine, except the internal standard was not added to the reaction flask due to poor solubility at low temperatures. Additionally, the reaction flask was immersed in a dry ice/acetone bath held at  $-30$   $^\circ\text{C}$  after  $\text{O}_2$  addition. The yields of phenyl vinyl ketone and cinnamaldehyde were less than 1%, indicating that catalytic turnover did not occur.



### Attempted Catalysis of Allylbenzene with **4** with a Base Additive

The procedure follows the representative procedure above with one exception. A fourth stock solution of *N,N*-diisopropyl ethyl amine (76 mg, 0.58 mmol, 171 mM) was prepared in MeCN (3.4 mL). From the stock solution, 1.6 mL of the base was added to the reaction flask. The yields of phenyl vinyl ketone and cinnamaldehyde were less than 1%, indicating that catalytic turnover did not occur. The reaction was repeated with pyridine as the solvent, with no catalytic turnover observed.

### Attempted Catalysis of Allylbenzene Under Neat Conditions

The procedure follows the representative procedure above except for the following. The stock solutions of **4** and tetradecane internal standard were prepared in DCM rather than MeCN. After the portions were added to the reaction flask, the solvent was removed *in vacuo*, and subsequently charged with 4Å molecular sieves. Allylbenzene (3.579 mL) was added to the round bottom flask, dissolving the residue. No catalytic turnover was observed.

### Attempted Catalysis of Allylbenzene with **4** in DCM at –50 °C

The procedure follows the representative procedure above except for the following. The stock solutions of **4**, tetradecane, and allylbenzene were prepared in DCM rather than MeCN. The flask was immersed in a dry ice/acetone bath held at –50 °C for 5 minutes before O<sub>2</sub> addition, and the temperature was maintained for the entirety of the reaction. No catalytic turnover was observed.

### Attempted Catalysis of Cinnamyl Pinacolborane in CDCl<sub>3</sub>, C<sub>6</sub>D<sub>6</sub>, or MeCN-*d*<sub>3</sub>

A stock solution of cinnamyl pinacolborane (78 mg, 0.32 mmol, 200 mM) was prepared in CDCl<sub>3</sub> (1.597 mL) in a 20 mL vial. In a separate vial, a stock solution of **4** (13 mg, 0.031 mmol, 20 mM) was prepared in CDCl<sub>3</sub> (1.545 mL). From the stock solution of cinnamyl pinacolborane, 225 μL was added to 6 NMR tubes (A-F), and 23 μL of the stock solution of **4** was added afterwards. All of the NMR tubes were diluted to a final volume of 0.6 mL and sealed with a septa cap. NMR tubes A and B were diluted with

CDCl<sub>3</sub>, C and D were diluted with C<sub>6</sub>D<sub>6</sub>, and E and F were diluted with MeCN-*d*<sub>3</sub>. The final concentrations were 75 mM cinnamyl pinacolborane and 0.75 mM **4** (1 mol%). A final NMR tube, G, was made by adding 225 μL of the stock solution of cinnamyl pinacolborane and diluted to 0.6 mL with CDCl<sub>3</sub> as a control. An initial <sup>1</sup>H NMR spectrum was collected of NMR tube G before O<sub>2</sub> addition. Dry O<sub>2</sub> was bubbled through NMR tubes AC, E, and G for ~20 seconds with a bleed needle present and were left to react at room temperature. To NMR tubes B, D, and F, dry O<sub>2</sub> was bubbled through the NMR tubes for ~20 seconds with a bleed needle present and placed into a preheated 50 °C oil bath (B) or a 70 °C oil bath (D and F). All of the NMR tubes were analyzed by <sup>1</sup>H NMR spectroscopy at one hour and 24 hours after O<sub>2</sub> addition.

### Control Reactions with Cinnamyl Pinacolborane in MeCN-*d*<sub>3</sub>

A stock solution of cinnamyl pinacolborane (48 mg, 0.20 mmol, 200 mM) was prepared in MeCN-*d*<sub>3</sub> (0.983 mL) in a 20 mL vial. In a separate vial, a stock solution of **4** (12 mg, 0.03 mmol, 20 mM) was prepared with MeCN-*d*<sub>3</sub> (1.426 mL). Lastly, a stock solution of dimethyl terephthalate (21 mg, 0.11 mmol, 100 mM) was prepared in MeCN-*d*<sub>3</sub> (1.081 mL) for use as an internal standard. To four NMR tubes (A-D), 225 μL of stock cinnamyl pinacolborane and 75 μL of dimethyl terephthalate were dispensed. To NMR tubes C and D, 22 μL of stock **4** was added. All four NMR tubes were diluted to a final volume of 0.6 mL, with the final concentrations being 75 mM cinnamyl pinacolborane, 0.75 mM **4** (if present), and 12.5 mM dimethyl terephthalate. The four NMR tubes were sealed with a septa cap and removed from the glovebox. NMR tubes A and C were immediately placed into a 70 °C oil bath. NMR tubes B and D had dry O<sub>2</sub> bubbled through a stainless steel needle with a bleed needle present for ~20 seconds, after which they were placed into a 70 °C oil bath. The reaction was monitored by <sup>1</sup>H NMR spectroscopy after 1, 4, 24, and 48 hours.

### General Procedure for the Quantification of Nickel-Based Products by <sup>1</sup>H NMR spectroscopy Following Oxidation of **4**

A vial was charged with **4** (5 mg, 0.01 mmol) and another vial was charged with dimethyl terephthalate (2 mg, 0.01 mmol). To the vial of **4**, 1 mL of the NMR solvent of choice

(C<sub>6</sub>D<sub>6</sub>, DCM-*d*<sub>2</sub>, MeCN-*d*<sub>3</sub>, dry MeCN-*d*<sub>3</sub>, pyridine-*d*<sub>5</sub>, or dry pyridine-*d*<sub>5</sub>) was added. The resulting solution was transferred to the vial containing the dimethyl terephthalate and the solids were dissolved. The resulting mixture was transferred to a NMR tube and fitted with a septum cap, and an initial <sup>1</sup>H NMR spectrum was collected. Dry O<sub>2</sub> was bubbled through a stainless steel needle into the NMR tube fitted with a bleed needle for ~20 seconds. An immediate color change was observed from dark orange to pale pink for C<sub>6</sub>D<sub>6</sub>, while the pyridine-*d*<sub>5</sub> samples changed color from pale orange to amber. The samples dissolved in DCM-*d*<sub>2</sub> and MeCN-*d*<sub>3</sub> showed a color change from yellow-orange to pale pink, with a large number of solids forming immediately for the DCM-*d*<sub>2</sub> sample. The tubes were left sealed under the O<sub>2</sub> atmosphere for the duration of the experiment, with <sup>1</sup>H NMR spectra collected at 5 minutes, 1, 4, 24, and 30 hours. Due to solid formation in the samples for DCM-*d*<sub>2</sub>, C<sub>6</sub>D<sub>6</sub>, and MeCN-*d*<sub>3</sub>, data collection was stopped at 4 hours for the sample prepared in DCM-*d*<sub>2</sub>, and 24 hours for the samples prepared in C<sub>6</sub>D<sub>6</sub> and MeCN-*d*<sub>3</sub>. No solids were observed in the samples prepared in pyridine-*d*<sub>5</sub>. The results of this analysis are tabulated and discussed in Section 2.2.

### Decomposition of **4** in MeCN

In a 20 mL vial, a sample of **4** (55 mg, 0.13 mmol) was dissolved in 5 mL MeCN. The resulting orange-brown solution was transferred to a 100 mL Schlenk flask charged with a stir bar; which was sealed with a septum cap and secured with electrical tape. The flask was removed from the glovebox. Dry O<sub>2</sub> was bubbled through a stainless steel needle for ~30 seconds with a bleed need present and the flask was stirred under a static O<sub>2</sub> atmosphere for 15 minutes. A color change from orange-brown to brown was observed over 15 minutes. The solvent and the allyl oxidation product propenal were removed *in vacuo* to give a brown residue. The Schlenk flask was brought back into the glovebox. The solid was extracted with C<sub>6</sub>D<sub>6</sub> to yield a red solution (A), which was transferred to a NMR tube. After 15 minutes, purple solids (B) were observed collecting on the bottom of the NMR tube. The solution inside the NMR tube remained red. The solids in the Schlenk flask were washed with additional C<sub>6</sub>H<sub>6</sub> (5 x 1 mL) until the washings were colorless, and were collected in a 20 mL vial. The initially collected NMR sample was mixed with the benzene washes and filtered through a glass microfiber pipette, with purple solids

collecting on top of the microfiber plug. The filtrate remained a red solution. The solids on the glass microfiber pipette were rinsed with pyridine into a clean 20 mL vial. This dissolved the purple solids giving a pale yellow solution. The solvents were removed *in vacuo* for both samples (A and B) to give solids of the matching colors for A, while B remained a pale yellow color. The solids, A and B, were analyzed by  $^1\text{H}$  NMR spectroscopy, yet no conclusive data could be drawn because the spectra were complex. From the isolated solids, crystals suitable for X-ray crystallography were obtained by slow vapor diffusion of hexanes into toluene for A, and hexanes into pyridine for B. Red crystals were observed from the crystallization of A and B, and were found to be  $\text{NiCl}_2(\text{NHC})_2 \cdot \text{H}_2\text{O}$ .<sup>61</sup> Blue crystals were observed from B, and were found to be *trans*- $\text{Cl}_2(\text{pyridine})_4 \cdot \text{H}_2\text{O}$ .<sup>62</sup>

### Decomposition of 4 in THF

The decomposition of **4** in THF follows a similar procedure as outlined above, with the following exceptions. A 20 mL vial was charged with **4** (125 mg, 0.297 mmol) and dissolved with 5 mL THF. The orange-brown solution and a stir bar were transferred to a Schlenk flask, which was then sealed with a septum cap and secured with electrical tape.  $\text{O}_2$  was then bubbled into the solution through a stainless steel needle for ~30 seconds with a bleed needle present. The solution was left to react under the static  $\text{O}_2$  atmosphere for 15 minutes, during which a color change from orange-brown to dark red was observed after 15 minutes of  $\text{O}_2$  addition. Dark red solids were observed in the Schlenk flask after removal of the solvent and propenal. An initial extraction was performed with  $\text{C}_6\text{D}_6$ , affording a red solution. A  $^1\text{H}$  NMR spectrum was obtained, but no conclusive evidence was found. An extraction with THF was performed and used to grow suitable crystals for X-ray crystallography by slow vapor diffusion with hexanes, revealing  $\text{NiCl}_2(\text{NHC})_2$ . Purple solids were observed forming at the bottom of the crystallization vial, but no suitable crystals were found. Brown solids remained in the flask after extraction.  $^1\text{H}$  NMR spectroscopy matched the literature values report by Ong *et al.* for  $\text{NiCl}_2(\text{NHC})_2$ .

### Attempted Synthesis of 11

In a vial, **5a** (49 mg, 0.099 mmol) was dissolved in 2 mL benzene. The solution was added to a 20 mL vial charged with a stir bar and solid  $\text{NaN}_3$  (7 mg, 0.1 mmol) and left to stir for 18 hours. The resulting dark orange-brown solution was left to sit undisturbed for two hours, at which time white solids were observed at the bottom of the vial. The solution was filtered through a glass microfiber pipette filter, with pale orange solids collected. The glass microfiber pipette filter was washed with benzene (3 x 1 mL). The resulting filtrate was dark orange-brown, and the solvent was removed under vacuum. The resulting orange-brown solid was washed with cold pentane ( $-35\text{ }^\circ\text{C}$ , 3 x 1 mL) and dried under vacuum.  $^1\text{H}$  NMR spectrum matches the starting species **5a**.

### Preliminary Synthesis of 11

A 20 mL vial was charged with a stir bar and **5a** (10 mg, 0.002 mmol). In another 20 mL vial,  $\text{NaN}_3$  (4 mg, 0.06 mmol) was added and dissolved in 10 mL MeCN. The  $\text{NaN}_3$  solution was added dropwise to the vial containing **5a** and left to stir for 4 days, upon which a slight color change was from orange to orange-yellow was observed. The solution was filtered through a glass microfiber pipette and washed with  $\text{C}_6\text{H}_6$  (3 x 1 mL), and the solvent removed *in vacuo* to afford a yellow-orange powder. Approximate yield (by relative  $^1\text{H}$  NMR integration): 5.5%  $^1\text{H}$  NMR (600 MHz,  $\text{C}_6\text{D}_6$ ): 7.28 ppm (br), 6.35 ppm (s), 6.29 ppm (s), 5.01 ppm (d, br), 3.88 ppm (d), 2.75 ppm (s), 2.50 ppm (t), 1.83 ppm (s), 1.81 ppm (s), 0.88 ppm (s), 0.80 ppm (s). ATR-IR ( $\text{cm}^{-1}$ ): 2039 (Ni- $\text{N}_3$ )

### General Procedure for Preparing 4 for UV-Vis Spectroscopy Experiments

In a vial, a stock solution of **4** (14 mg, 0.033 mmol, 100 mM) was dissolved in DCM (332  $\mu\text{L}$ ). The cuvette was charged with 4 mL DCM, capped, and removed from the glovebox. The DCM blank was obtained at room temperature on the UV-visible spectrometer. The cuvette was then cleaned and brought back into the glovebox. The cuvette was then charged with 200  $\mu\text{L}$  of the stock solution of **4** and diluted with DCM (800  $\mu\text{L}$ ) to give a final volume of 4 mL and a final concentration of 5 mM **4**. The cuvette was capped, removed from the glovebox, and placed in the spectrometer to obtain a room temperature spectrum. The spectrometer was then cooled to  $-78\text{ }^\circ\text{C}$  and the solution was allowed to equilibrate for 5 minutes. A low temperature spectrum was obtained. After

this time, the N<sub>2</sub> atmosphere in the cuvette was replaced by flowing dry O<sub>2</sub> into the headspace with a bleed needle present for ~15 seconds.

### **Low Temperature Stoichiometric Oxidation Monitored by UV-Vis Spectroscopy**

The start of this experiment follows the general procedure as above, with the following exceptions. Once the temperature equilibrium was reached, the kinetics experiment was started, collecting a UV-Visible spectrum every 5 minutes for 2 hours. After 5 minutes, the headspace was replaced with O<sub>2</sub> by flowing dry O<sub>2</sub> into the cuvette with a bleed needle present. The solution was not bubbled as it would have accelerated the reaction too quickly and made intermediate determination difficult. The reaction between **4** and O<sub>2</sub> was complete after two hours as there were no changes observed in the UV-vis spectra. A spectrum was collected after this time and labelled intermediate 1 (**Int. 1**). The sample was warmed to -65 °C, and a spectrum was collected every 5 minutes for 1 h, after which no changes were observed in the UV-vis spectra. A spectrum was collected after this time and labelled intermediate 2 (**Int. 2**). Lastly, the reaction was warmed to -30 °C and left to react for 30 minutes, collecting a UV-visible spectrum once every 5 minutes. The final spectrum matched the room temperature decomposition spectrum.

### **Determination of Non-Reversible O<sub>2</sub> Binding by UV-Visible Spectroscopy**

The preparation for this experiment follows the same general procedure as above. The sample was left to react with O<sub>2</sub> for 2 hours, and the conversion was confirmed by collecting a UV-vis spectrum after this time. Dry N<sub>2</sub> was then bubbled into the cuvette through a stainless steel needle for ~30 seconds with a bleed needle present. A UV-visible spectrum was collected every 5 minutes for 75 minutes, with no change in the UV-Vis spectra observed.

### **Determination of Non-Reversible Intermediate Formation by UV-Visible Spectroscopy**

The preparation for this experiment follows the general procedure as above. After O<sub>2</sub> addition, the reaction was left at -78 °C for two hours. After the formation of **Int. 1** was confirmed by collecting a UV-Visible spectrum, the temperature was raised to -65 °C

and held for one hour, scanning every 5 minutes until no changes in the collected spectra were observed. After this, the sample was cooled to  $-78\text{ }^{\circ}\text{C}$  and held for 35 minutes, scanning every 5 minutes. No changes were observed in the UV-vis spectra upon cooling from  $-65\text{ }^{\circ}\text{C}$  to  $-78\text{ }^{\circ}\text{C}$ . The sample was then warmed to  $-65\text{ }^{\circ}\text{C}$  and allowed to equilibrate for 5 minutes. After this time, the sample was warmed to  $-40\text{ }^{\circ}\text{C}$  and held at that temperature for one hour, scanning every 5 minutes. After this time, the temperature was raised to  $-30\text{ }^{\circ}\text{C}$  and held for 55 minutes, scanning every 5 minutes. After this time, the sample was cooled to  $-40\text{ }^{\circ}\text{C}$  and held for 15 minutes, scanning every 5 minutes. The reaction was stopped once it was apparent that there was no temperature mediated reversibility.

### **Attempted Hydrogen Atom Transfer Reaction with Int. 1 and 1,2 Diphenyl Hydrazine**

The initial steps for this experiment follow the same general procedure as above, with the following exceptions. A stir bar was placed inside the cuvette before obtaining the blank spectrum. In a 5 mL round bottom flask, a stock solution of 1,2 diphenyl hydrazine (88 mg, 0.48 mmol, 100 mM) was dissolved in DCM (4.78 mL). The flask was sealed with a septum and removed from the glovebox. After confirming the formation of **Int. 1** by UV-Visible spectroscopy, the magnetic stirrer was turned on. A 20  $\mu\text{L}$  (0.2 equiv. of  $\text{H}^{\bullet}$ ) aliquot of the 1,2 diphenyl hydrazine solution was injected into the cuvette via a microliter syringe. A UV-Visible spectrum was collected every minute for ten minutes. Additional 20  $\mu\text{L}$  (0.2 equiv.) injections of the 1,2 diphenyl hydrazine solution were made up to for a total of 1.2 equivalents  $\text{H}^{\bullet}$  to **Int. 1**.

### **Titration of Acid into Int. 2**

The initial steps of this experiment follow the general procedure above, with the following exceptions. The cuvette was charged with a stir bar before the blank spectrum was obtained. In a 5 mL round bottom flask, a stock solution of pyridinium chloride (91 mg, 0.79 mmol, 100 mM) was dissolved in DCM (3.94 mL). The flask was sealed with a septum and removed from the glovebox. The sample was cooled to  $-78\text{ }^{\circ}\text{C}$  and left to equilibrate for 5 minutes. After this time, the headspace was replaced with  $\text{O}_2$  by flushing



O<sub>2</sub> through a stainless steel needle through the septum with a bleed needle present. The sample was left at temperature for 2 h, and the formation of **Int. 1** was confirmed by UV-vis spectroscopy. The sample was then warmed to  $-65\text{ }^{\circ}\text{C}$  and left to equilibrate for 5 minutes. After this time, the sample was left at temperature for 1 h. After confirming the formation of **Int. 2** by UV-vis spectroscopy, the magnetic stirrer was turned on. A 20  $\mu\text{L}$  (0.2 equiv.) aliquot of the pyridinium chloride solution was injected into the cuvette via a microliter syringe. A UV-visible spectrum was collected every minute for ten minutes. A total of six additions of the pyridinium chloride solution were made, for a total of 1.2 equivalents of pyridinium chloride to **Int. 2**.

#### **VT-NMR Spectroscopy of a Solution of 4 that was Treated with O<sub>2</sub> at $-78\text{ }^{\circ}\text{C}$**

In a vial, a stock solution of **4** (57 mg, 14 mmol, 100 mM) was dissolved in dry DCM-*d*<sub>2</sub> (1.355 mL). In a separate vial, a stock solution of the internal standard 1,3,5-trimethoxybenzene (13 mg, 0.077 mmol, 100 mM) was dissolved in DCM-*d*<sub>2</sub> (773  $\mu\text{L}$ ). To two NMR tubes (A and B), 60  $\mu\text{L}$  of the **4** stock solution and 6.7  $\mu\text{L}$  of the internal standard stock solution were added. Both NMR tubes were then diluted to a final volume of 600  $\mu\text{L}$ , making the final concentrations 10 mM **4** and 1.1 mM internal standard. Both NMR tubes were capped with septa caps, removed from the glovebox, and sealed with parafilm. Sample A was inserted into the NMR spectrometer and a room temperature spectrum was obtained before cooling to  $-78\text{ }^{\circ}\text{C}$ . After equilibrating for 5 minutes, a low temperature spectrum was obtained, and was found to match previous studies.((REF)) Sample B was placed in a liquid nitrogen/acetone bath, cooled to  $-85\text{ }^{\circ}\text{C}$ , and allowed to equilibrate for 5 minutes. After equilibrating, the headspace was flushed with dry O<sub>2</sub> through a needle with a bleed needle present. NMR tube B was then quickly exchanged with NMR tube A and left to equilibrate inside the NMR spectrometer for 5 minutes. After this time, a <sup>1</sup>H NMR spectrum was collected at each 5 minute time point for 2 hours. The temperature was then raised to  $-65\text{ }^{\circ}\text{C}$ , and allowed to equilibrate for 5 minutes. After this time, a <sup>1</sup>H NMR spectrum was collected at each 5 minute time point for 2 hours, followed by collection of a <sup>1</sup>H-<sup>1</sup>H COSY spectrum. The temperature was then raised to  $-30\text{ }^{\circ}\text{C}$ , with a <sup>1</sup>H NMR spectrum collected at each 5 minute time point for 0.5 hours. A <sup>1</sup>H NMR spectrum was then collected at  $-25\text{ }^{\circ}\text{C}$ ,  $0\text{ }^{\circ}\text{C}$ , and  $25\text{ }^{\circ}\text{C}$ . This



reaction was repeated with higher concentrations of **4** (50 mM in NMR tubes). However, the reactivity did not match what was previously observed.

### Evans' Method Analysis of Int. 1 and Int. 2

Sample preparation and cooling procedures are the same as above, except a sealed capillary tube of 1:8 DCM:DCM- $d_2$  was placed inside the NMR tubes as well. Once the temperature had equilibrated, a  $^1\text{H}$  NMR spectrum was collected at each 5 minute time point for 2 hours. The temperature was then raised to  $-65\text{ }^\circ\text{C}$  and the sample was left to equilibrate for 5 minutes. After the temperature was equilibrated, a  $^1\text{H}$  NMR spectrum was collected at each 5 minute time point for 1 hour. The temperature was raised to  $-40\text{ }^\circ\text{C}$ , and the sample was left to equilibrate for 5 minutes. After this, a  $^1\text{H}$  NMR spectrum was collected. The remainder of the experiment follows the same procedure as ## above.

### Computational Methods

All calculations were performed using Gaussian 09.<sup>85</sup> Geometry optimization, vibrational frequency calculations, and time-dependent calculations were performed using the B3LYP<sup>77, 86</sup> functional in the solvent free gas phase. The LANL2DZ effective core potential basis set was used for nickel, and the 6-31G(d) was used for other atoms. Dioxygen was modelled in its triplet state. The computed metal complexes were derived from related crystal structures where.<sup>49, 53-54, 61</sup> The desired complexes were visualized and constructed using the Arguslab software. The NHC ligand was truncated in the following ways:  $t\text{Bu}$  was converted to Me, Mes was converted to Ph. The geometries of the structures were first optimized to ensure accurate data was obtained from further analysis. The Gaussian input file was generated in Arguslab and edited to ensure that the appropriate keywords were included. The input file was then transferred to the SHARCNet Orca cluster to be run on the Gaussian 09 program. Once the job had completed, the formcheck file was generated and visualized in Arguslab. From the optimized geometries, the thermodynamic data was obtained at  $-65\text{ }^\circ\text{C}$  (208.15 K) for all species. For the metal complexes, the first 40 excited states were calculated by TD-DFT from the optimized geometry.

## References

1. Punniyamurthy, T.; Velusamy, S.; Iqbal, J., *Chem. Rev.* **2005**, *105*, 2329-2364.
2. Nakamura, A.; Nakada, M., *Synthesis* **2013**, *45*, 1421-1451.
3. Shi, Z.; Zhang, C.; Tang, C.; Jiao, N., *Chem. Soc. Rev.* **2012**, *41*, 3381-3430.
4. Ely, R. J.; Morken, J. P., *J. Am. Chem. Soc.* **2010**, *132*, 2534-2535.
5. Limnios, D.; Kokotos, C. G., *J. Org. Chem.* **2014**, *79*, 4270-4276.
6. Yu, H.; Shen, J., *Org. Lett.* **2014**, *16*, 3204-3207.
7. Dach, R.; Song, J. J.; Roschangar, F.; Samstag, W.; Senanayake, C. H., *Org. Process Res. Dev.* **2012**, *16* (11), 1697-1706.
8. Armitage, J. B.; Strauss, H. W., *Ind. Eng. Chem.* **1964**, *56*, 28-32.
9. tert-Butyl Hydroperoxide MSDS. tert-Butyl Hydroperoxide ; MSDS No. B2633 [Online]; Sigma-Aldrich: St. Louis, MO, March 7, 2015.  
<http://www.sigmaaldrich.com/MSDS/MSDS/DisplayMSDSPage.do?country=CA&language=en&productNumber=B2633&brand=SIAL&PageToGoToURL=http%3A%2F%2Fwww.sigmaaldrich.com%2Fcatalog%2Fproduct%2Fisial%2Fb2633%3Flang%3Den>  
(accessed August 23, 2017).
10. Chromium(VI) oxide MSDS. Chromium(VI) oxide ; MSDS No. 27081 [Online]; Sigma-Aldrich: St. Louis, MO, December 29, 2017.  
[www.sigmaaldrich.com/MSDS/MSDS/DisplayMSDSPage.do?country=CA&language=en&productNumber=27081&brand=SIGALD&PageToGoToURL=http%3A%2F%2Fwww.sigmaaldrich.com%2Fcatalog%2Fproduct%2Fsigald%2F27081%3Flang%3Den](http://www.sigmaaldrich.com/MSDS/MSDS/DisplayMSDSPage.do?country=CA&language=en&productNumber=27081&brand=SIGALD&PageToGoToURL=http%3A%2F%2Fwww.sigmaaldrich.com%2Fcatalog%2Fproduct%2Fsigald%2F27081%3Flang%3Den)  
(accessed August 23, 2017).
11. Blanksby, S. J.; Ellison, G. B., *Acc. Chem. Res.* **2003**, *36*, 255-263.
12. Roudesly, F.; Oble, J.; Poli, G., *J. Mol. Catal. A: Chem.* **2017**, *426*, 275-296.
13. Shing, T. K. M.; Jiang, Q., *J. Org. Chem.* **2000**, *65*, 7059-7069.
14. Lee, H.-Y.; Sha, C.-K., *J. Org. Chem.* **2012**, *77*, 598-605.
15. Jeker, O. F.; Carreira, E. M., *Angew. Chem. Int. Ed.* **2012**, *51*, 3474-3477.
16. Ho, T.-L.; Su, C.-Y., *J. Org. Chem.* **2000**, *65*, 3566-3568.
17. Yu, J.-Q.; Corey, E. J., *J. Am. Chem. Soc.* **2003**, *125*, 3232-3233.

18. Chen, H.; Jiang, H.; Cai, C.; Dong, J.; Fu, W., *Org. Lett.* **2011**, *13*, 992-994.
19. Osterberg, P. M.; Niemeier, J. K.; Welch, C. J.; Hawkins, J. M.; Martinelli, J. R.; Johnson, T. E.; Root, T. W.; Stahl, S. S., *Org. Process Res. Dev.* **2015**, *19* (11), 1537-1543.
20. Constable, D. J. C.; Dunn, P. J.; Hayler, J. D.; Humphrey, G. R.; Leazer, J. J. L.; Linderman, R. J.; Lorenz, K.; Manley, J.; Pearlman, B. A.; Wells, A.; Zaks, A.; Zhang, T. Y., *Green Chem.* **2007**, *9*, 411-420.
21. Newman, S. G.; Jensen, K. F., *Green Chem.* **2013**, *15*, 1456-1472.
22. Ye, X.; Johnson, M. D.; Diao, T.; Yates, M. H.; Stahl, S. S., *Green Chem.* **2010**, *12*, 1180-1186.
23. Drago, R. S., *Coord. Chem. Rev.* **1992**, *117*, 185-213.
24. Fusi, A.; Ugo, R.; Zanderighi, G. M., *J. Catal.* **1974**, *34*, 175-190.
25. Wang, R.-M.; Hao, C.-J.; Wang, Y.-P.; Li, S.-B., *J. Mol. Catal. A: Chem.* **1999**, *147*, 173-178.
26. Lajunen, M. K.; Maunula, T.; Koskinen, A. M. P., *Tetrahedron* **2000**, *56*, 8167-8171.
27. Sankaralingam, M.; Lee, Y.-M.; Nam, W.; Fukuzumi, S., *Inorg. Chem.* **2017**, *56*, 5096-5104.
28. Li, Z.; Liu, C.; Tang, R.; Liu, G., *RSC Adv.* **2013**, *3*, 9745-9751.
29. Salavati-Niasari, M., *J. Mol. Catal. A: Chem.* **2007**, *272*, 207-212.
30. Denisov, I. G.; Makris, T. M.; Sligar, S. G.; Schlichting, I., *Chem. Rev.* **2005**, *105*, 2253-2278.
31. Yoshikawa, S.; Shimada, A., *Chem. Rev.* **2015**, *115*, 1936-1989.
32. Luo, F.; Shinzawa-Itoh, K.; Hagimoto, K.; Shimada, A.; Shimada, S.; Yamashita, E.; Yoshikawa, S.; Tsukihara, T., *Acta Crystallogr. Sect. F* **2017**, *73*, 416-422.
33. Rich, P. R., *Biochem. Soc. Tran.* **2017**, *45*, 813-829.
34. Jeoung, J.-H.; Nianios, D.; Fetzner, S.; Dobbek, H., *Angew. Chem. Int. Ed.* **2016**, *55*, 3281-3284.
35. Holland, P. L., *Dalton Trans.* **2010**, *39*, 5415-5425.
36. Yao, S.; Bill, E.; Milsmann, C.; Wieghardt, K.; Driess, M., *Angew. Chem. Int. Ed.* **2008**, *47*, 7110-7113.

37. Ananikov, V. P., *ACS Catal.* **2015**, *5*, 1964-1971.
38. Jones, G. D.; Martin, J. L.; McFarland, C.; Allen, O. R.; Hall, R. E.; Haley, A. D.; Brandon, R. J.; Konovalova, T.; Desrochers, P. J.; Pulay, P.; Vivic, D. A., *J. Am. Chem. Soc.* **2006**, *128*, 13175-13183.
39. Biswas, S.; Weix, D. J., *J. Am. Chem. Soc.* **2013**, *135*, 16192-16197.
40. Kieber-Emmons, M. T.; Riordan, C. G., *Acc. Chem. Res.* **2007**, *40*, 618-625.
41. Dible, B. R.; Sigman, M. S.; Arif, A. M., *Inorg. Chem.* **2005**, *44*, 3774-3776.
42. Deb, T.; Rohde, G. T.; Young, V. G.; Jensen, M. P., *Inorg. Chem.* **2012**, *51*, 7257-7270.
43. Watson, M. B.; Rath, N. P.; Mirica, L. M., *J. Am. Chem. Soc.* **2017**, *139*, 35-38.
44. Chianese, A. R.; Li, X.; Janzen, M. C.; Faller, J. W.; Crabtree, R. H., *Organometallics* **2003**, *22*, 1663-1667.
45. Dorta, R.; Stevens, E. D.; Scott, N. M.; Costabile, C.; Cavallo, L.; Hoff, C. D.; Nolan, S. P., *J. Amer. Chem. Soc.* **2005**, *127*, 2485-2495.
46. Goldcamp, M. J.; Robison, S. E.; Krause Bauer, J. A.; Baldwin, M. J., *Inorg. Chem.* **2002**, *41*, 2307-2309.
47. Cho, J.; Kang, H. Y.; Liu, L. V.; Sarangi, R.; Solomon, E. I.; Nam, W., *Chem. Sci.* **2013**, *4*, 1502-1508.
48. Kimura, E.; Machida, R.; Kodama, M., *J. Am. Chem. Soc.* **1984**, *106*, 5497-5505.
49. Dible, B. R.; Sigman, M. S., *J. Am. Chem. Soc.* **2003**, *125*, 872-873.
50. Dible, B. R.; Sigman, M. S., *Inorg. Chem.* **2006**, *45*, 8430-8441.
51. Huang, D.; Holm, R. H., *J. Am. Chem. Soc.* **2010**, *132*, 4693-4701.
52. Powell-Jia, D.; Ziller, J. W.; DiPasquale, A. G.; Rheingold, A. L.; Borovik, A. S., *Dalton Trans.* **2009**, 2986-2992.
53. Samantaray, M. K.; Shaikh, M. M.; Ghosh, P., *Organometallics* **2009**, *28*, 2267-2275.
54. Hazlehurst, R. J.; Hendriks, S. W. E.; Boyle, P. D.; Blacquiere, J. M., *ChemistrySelect* **2017**, *2*, 6732-6737.
55. Omer, H. M.; Liu, P., *J. Am. Chem. Soc.* **2017**, *139*, 9909-9920.

56. Darwent, B. d., *National Standard Reference Data Series*. 31 ed.; National Bureau of Standards: Washington, 1970.
57. Hazlehurst, R. J. *Aerobic Oxidations Mediated by Allylnickel(N-Heterocyclic Carbene)Chloride Complexes: Investigating the Role of a Pendent Amine Group*. Western University, London, ON, 2016.
58. Feng, M.; Tang, B.; Xu, H.-X.; Jiang, X., *Org. Lett.* **2016**.
59. Fujii, T.; Nishida, H.; Abiru, Y.; Yamamoto, M.; Kise, M., *Chem. Pharm. Bull.* **1995**, *43*, 1872-1877.
60. Zhang, P.; Roundtree, I. A.; Morken, J. P., *Org. Lett.* **2012**, *14*, 1416-1419.
61. Huang, Y.-P.; Tsai, C.-C.; Shih, W.-C.; Chang, Y.-C.; Lin, S.-T.; Yap, G. P. A.; Chao, I.; Ong, T.-G., *Organometallics* **2009**, *28*, 4316-4323.
62. Cisterna, J.; Artigas, V.; Fuentealba, M.; Hamon, P.; Manzur, C.; Dorcet, V.; Hamon, J.-R.; Carrillo, D., *Inorg. Chim. Acta* **2017**, *462*, 266-280.
63. Izutsu, K., *Acid-Base Dissociation Constants in Dipolar Aprotic Solvents*. Blackwell Scientific: Oxford, UK, 1990.
64. Barondeau, D. P.; Kassmann, C. J.; Bruns, C. K.; Tainer, J. A.; Getzoff, E. D., *Biochem.* **2004**, *43*, 8038-8047.
65. Schmidt, M.; Scherk, C.; Iakovleva, O.; Nolting, H. F.; Meier, B.; Parak, F., *Inorg. Chim. Acta* **1998**, *275*, 65-72.
66. Bertini, I.; Luchinat, C.; Scozzafava, A., *J. Am. Chem. Soc.* **1980**, *102*, 7349-7353.
67. Reedijk, J., *Chem. Soc. Rev.* **2013**, *42*, 1776-1783.
68. Ishikawa, R.; Fuyuhiko, A.; Hayami, S.; Inoue, K.; Kawata, S., *J. Mol. Struct.* **2008**, *892*, 220-224.
69. Duggan, D. M.; Hendrickson, D. N., *Inorg. Chem.* **1973**, *12*, 2422-2431.
70. van Albada, G. A.; Smeets, W. J. J.; Spek, A. L.; Reedijk, J., *J. Chem. Crystallogr.* **1998**, *28*, 427-432.
71. Sodium Azide FT-IR Spectrum.  
<http://www.sigmaaldrich.com/spectra/ftir/FTIR002576.PDF> (accessed August 16, 2016).
72. Warren, J. J.; Tronic, T. A.; Mayer, J. M., *Chem. Rev.* **2010**, *110*, 6961-7001.
73. Ansari, A.; Jayapal, P.; Rajaraman, G., *Angew. Chem. Int. Ed.* **2015**, *54*, 564-568.

74. Cho, J.; Yap, G. P. A.; Riordan, C. G., *Inorg. Chem.* **2007**, *46*, 11308-11315.
75. Drago, R. S.; Corden, B. B., *Acc. Chem. Res.* **1980**, *13*, 353-360.
76. Campora, J.; Matas, I.; Palma, P.; Graiff, C.; Tiripicchio, A., *Organometallics* **2005**, *24*, 2827-2830.
77. Lee, C.; Yang, W.; Parr, R. G., *Phys. Rev. B* **1988**, *37*, 785-789.
78. Buvaylo, E. A.; Melnyk, A. K.; Trachevsky, V. V.; Vassilyeva, O. Y.; Skelton, B. W., *Polyhedron* **2016**, *105*, 238-245.
79. Truong, P. T.; Gale, E. M.; Dzul, S. P.; Stemmler, T. L.; Harrop, T. C., *Inorg. Chem.* **2017**, *56* (14), 7761-7780.
80. Schneck, F.; Finger, M.; Tromp, M.; Schneider, S., *Chem. – Eur. J.* **2017**, *23*, 33-37.
81. Fernandez, F. E.; Puerta, M. C.; Valerga, P., *Organometallics* **2011**, *30*, 5793-5802.
82. Yang, D.; Tang, Y.; Song, H.; Wang, B., *Organometallics* **2016**, *35*, 1392-1398.
83. Krysan, D. J.; Mackenzie, P. B., *J. Org. Chem.* **1990**, *55*, 4229-4230.
84. He, Y.; Lv, M.-f.; Cai, C., *Dalton Trans.* **2012**, *41*, 12428-12433.
85. Frisch, M. J.; Trucks, G. W.; Schlegel, H. B.; Scuseria, G. E.; Robb, M. A.; Cheeseman, J. R.; Scalmani, G.; Barone, V.; Petersson, G. A.; Nakatsuji, H.; Li, X.; Caricato, M.; Marenich, A.; Bloino, J.; Janesko, B. G.; Gomperts, R.; Mennucci, B.; Hratchian, H. P.; Ortiz, J. V.; Izmaylov, A. F.; Sonnenberg, J. L.; Williams-Young, D.; Ding, F.; Lipparini, F.; Egidi, F.; Goings, J.; Peng, B.; Petrone, A.; Henderson, T.; Ranasinghe, D.; Zakrzewski, V. G.; Gao, J.; Rega, N.; Zheng, G.; Liang, W.; Hada, M.; Ehara, M.; Toyota, K.; Fukuda, R.; Hasegawa, J.; Ishida, M.; Nakajima, T.; Honda, Y.; Kitao, O.; Nakai, H.; Vreven, T.; Throssell, K.; Montgomery, J., J. A. ; Peralta, J. E.; Ogliaro, F.; Bearpark, M.; Heyd, J. J.; Brothers, E.; Kudin, K. N.; Staroverov, V. N.; Keith, T.; Kobayashi, R.; Normand, J.; Raghavachari, K.; Rendell, A.; Burant, J. C.; Iyengar, S. S.; Tomasi, J.; Cossi, M.; Millam, J. M.; Klene, M.; Adamo, C.; Cammi, R.; Ochterski, J. W.; Martin, R. L.; Morokuma, K.; Farkas, O.; Foresman, J. B.; Fox, D. J. *Gaussian 09*, E.01; Wallingford, CT, 2010.
86. Becke, A. D., *Phys. Rev. A* **1988**, *38*, 3098-3100.

## Appendices

$$X_M = \frac{477\Delta_{ppm}}{2V_1c} \quad (1)$$

Equation 1: Magnetic susceptibility ( $X_M$ ,  $\text{cm}^3\text{mol}^{-1}$ ) equation from Evans method.  $\Delta_{ppm}$  is the difference between the solvent signals in the  $^1\text{H}$  NMR (Hz),  $V_1$  is the magnetic frequency (Hz), and  $c$  is the concentration ( $\text{molL}^{-1}$ ).

$$\mu_{eff} = \sqrt{8X_M T} \quad (2)$$

Equation 2: Effective magnetic moment  $\mu_{eff}$  ( $\mu_B$ ) equation.  $X_M$  is the magnetic susceptibility ( $\text{cm}^3\text{mol}^{-1}$ ),  $T$  is the temperature in degrees Kelvin (K).

$$\mu_{eff} = \sqrt{n(n+2)} \quad (3)$$

Equation 3: Spin-only approximation equation.  $\mu_{eff}$  is the effective magnetic moment ( $\mu_B$ ). Number of unpaired electrons ( $n$ ).

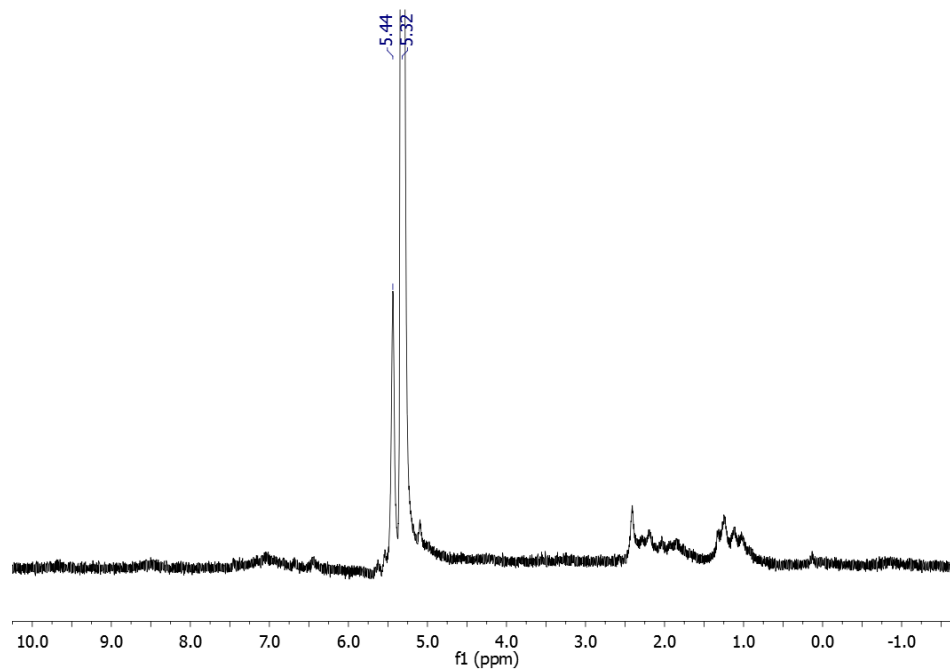


Figure 0.1:  $^1\text{H}$  NMR spectrum of **Int. 2** at  $-65\text{ }^\circ\text{C}$  in  $\text{DCM-}d_2$  with a capillary tube of 1:8  $\text{DCM}:\text{DCM-}d_2$  present. The signal at 5.32 ppm is DCM, while the signal at 5.44 ppm is the paramagnetically shifted DCM.

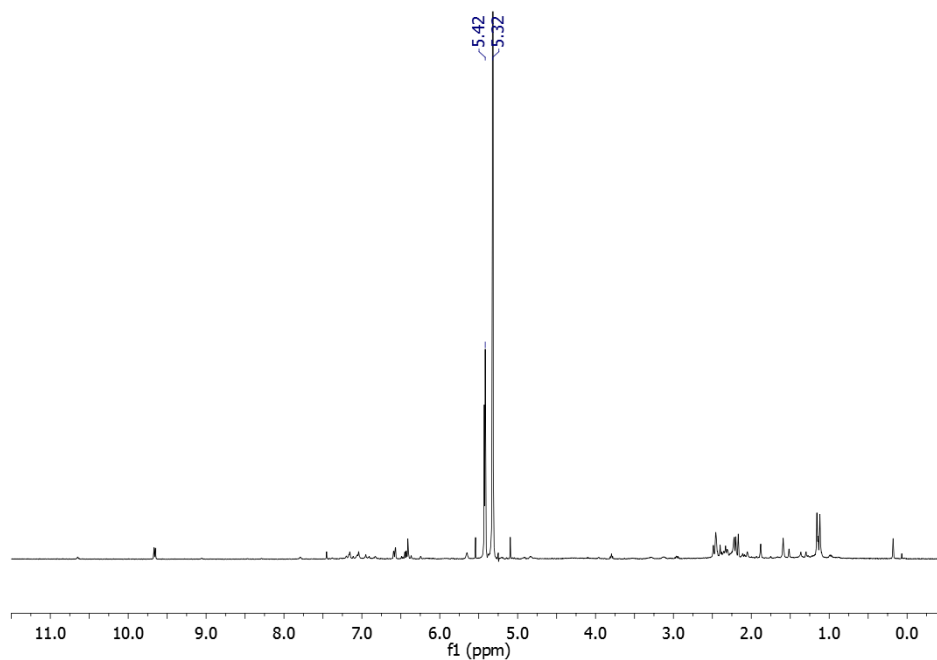


Figure 0.2:  $^1\text{H}$  NMR spectrum of decomposed **4** at  $25\text{ }^\circ\text{C}$  3.5 h after  $\text{O}_2$  addition at  $-78\text{ }^\circ\text{C}$  in  $\text{DCM-}d_2$  with a capillary tube of 1:8  $\text{DCM}:\text{DCM-}d_2$  present. The signal at 5.32 ppm is DCM, while the signal at 5.42 ppm is paramagnetically shifted DCM.



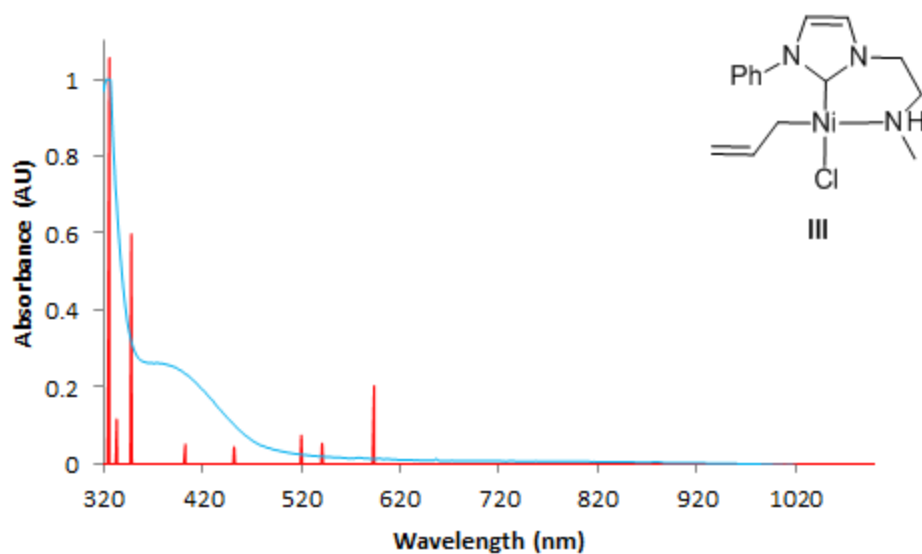


Figure 0.3: Obtained UV-vis spectrum of **4** at  $-65$  °C (blue) and TD-DFT simulated spectrum of **III** (red).

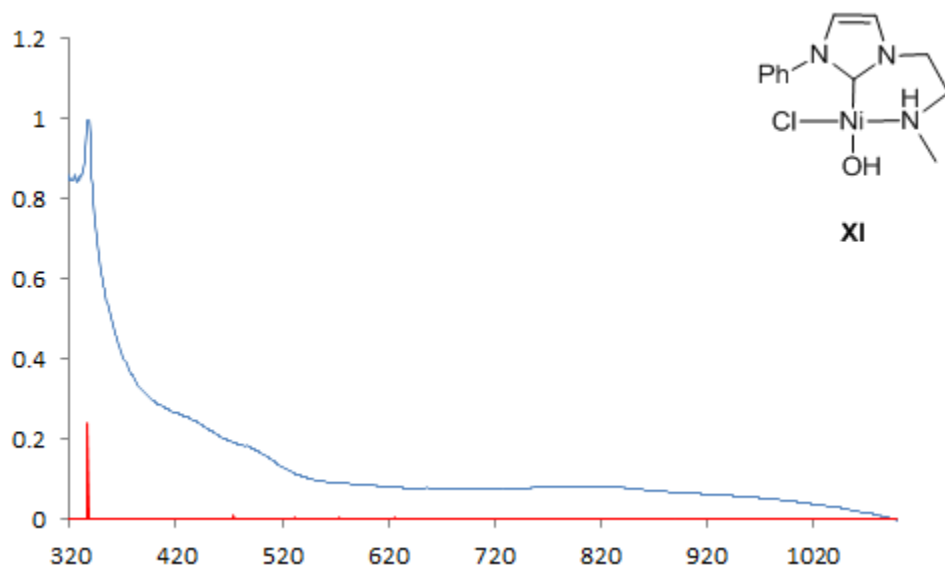


Figure 0.4: Obtained UV-vis spectrum of **Int. 2** at  $-65$  °C (blue) and TD-DFT simulated spectrum of **XI** (red).

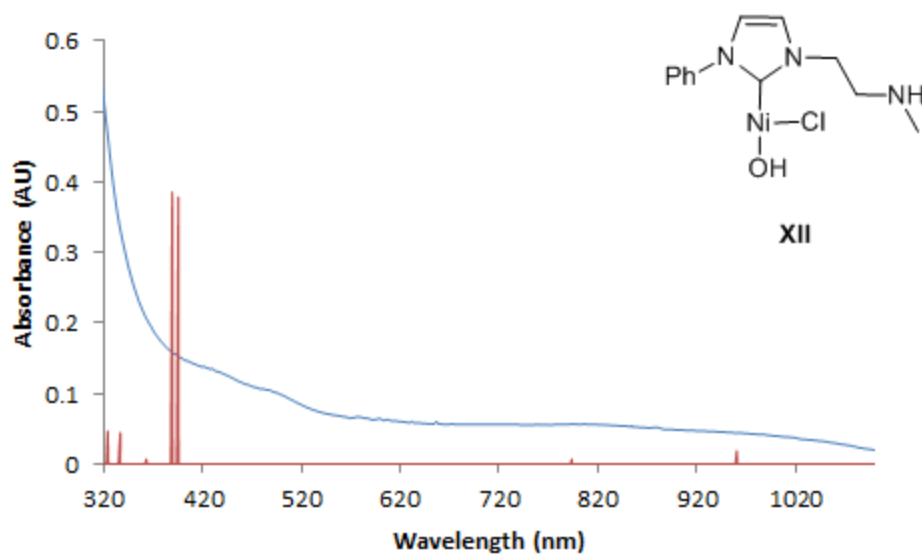


Figure 0.5: Obtained UV-vis spectrum of **Int. 2** at  $-65\text{ }^{\circ}\text{C}$  (blue) and TD-DFT simulated spectrum of **XII** (red).

## Curriculum Vitae

### Summary of Strengths

- Strong Analytical and Problem Solving Skills: Researched and implemented alternate methods to solve a chemical modelling problem and determined intermediate structures
- Safety-Oriented: Responded appropriately to a chemical spill within the workplace which resulted in a successful remediation without injury. Have trained others in chlorine chemical handling procedures with regards to indoor swimming pools
- Demonstrated leadership ability: Have been promoted to assistant supervisor positions within two community pools (YMCA and Dorchester Community Pool)
- Effective communicator and Instructor: Prepared and facilitated both public swimming lessons as well as lifeguard staff training.
- Effective team leader: Have been responsible for over-seeing 4-6 swim instructors during lessons to ensure effective program delivery
- Technical skills: Proficient with Microsoft Excel, Word, and Powerpoint, as well as chemical modelling software

### Education

**M.Sc. Inorganic Chemistry (Pending)** September 2015-Present

The University of Western Ontario, London, ON

- Thesis title: Determining the Reactivity and Oxidation Intermediates of an Allylnickel (*N*-Heterocyclic Carbene) Chloride Complex

**B.Sc. Honours Specialization in Chemistry** September 2011-April 2015

The University of Western Ontario, London, ON

- Relevant courses include Instrumental Analytical Chemistry, Inorganic Chemistry of Main Group Elements, and Transition Metal Chemistry

### Relevant Skills and Experience

M.Sc. Research – Blacquiere Group 2015-Present

The University of Western Ontario, London, ON

- Trained in proper handling of air and moisture sensitive materials (Schlenk and glovebox techniques)
- Communicate important aspects of research with Dr. Johanna Blacquiere
- Independently perform ligand and organometallic synthesis reactions
- Characterized reaction products and monitored reactions *in situ* (NMR, IR, MALDI-MS, UV-vis)
- Prepare and analyze catalytic reactions (GC-FID, NMR)
- Participate in weekly group meetings
- Maintain standard operation of a MBraun glovebox

Chemistry 4491E: Chemical Research Discovery and Scientific Communication 2014-15

The University of Western Ontario, London, ON

- Assigned an independent study project within the Stillman Bioinorganic Group
- Participated in weekly group meetings
- Communicated feedback to Dr. Stillman, who oversaw my research
- Created a computer model that resulted in ground-breaking results that may be published for the advancement of the scientific community
- Trained myself on components of Gaussian computer software

Lifeguard Team Leader

2010-15

Bob Hayward YMCA, London, ON

- Supervised the pool during a variety of activities including swimming lessons, open swim, and fitness classes
- Instructed students from 6 months to the elderly in swimming safety and technique
- Resolved disputes between parents and instructors
- Recommended several schedule changes that were implemented
- Mentored new staff members in how to effectively guard and instruct
- Reviewed instructor performance through internal audits and offered feedback

Assistant Supervisor

2011-2014 (Seasonal)

Dorchester Community Pool, Dorchester, ON

- Performed opening and closing duties, including set up of safety equipment and safely depositing cash
- Handled transactions between the public and the municipal office
- Scheduled shifts for staff members, including lessons and private lessons

- Assisted in the recruitment and selection process for junior staff members
- Responsible for answering phone calls and handling disagreements from the public

### **Publications and Presentations**

- Hazlehurst, R. J.; Hendriks, S. W. E.; Boyle, P. D.; Blacquiere, J. M., Ligand Dynamics and Aerobic Allylic Oxidation with Bifunction Ni(NHC) Complexes, *ChemistrySelect* **2017**, 2, 6732
- Poster Presentation at the 49<sup>th</sup> IDW Conference. Poster Title: Oxygen Reactivity of a NiCl( $\pi$ -allyl)(NHC) Species
- Poster Presentation at the 100<sup>th</sup> CSC Conference. Poster Title: Oxygen Reactivity of a NiCl( $\pi$ -allyl)(NHC) Species

**\*\*References Made Available Upon Request\*\***